DTU Nanotech
Department of Micro- and Nanotechnology

Master Thesis, s032091

Acoustofluidics in microsystems: investigation of resonances

Rune Barnkob

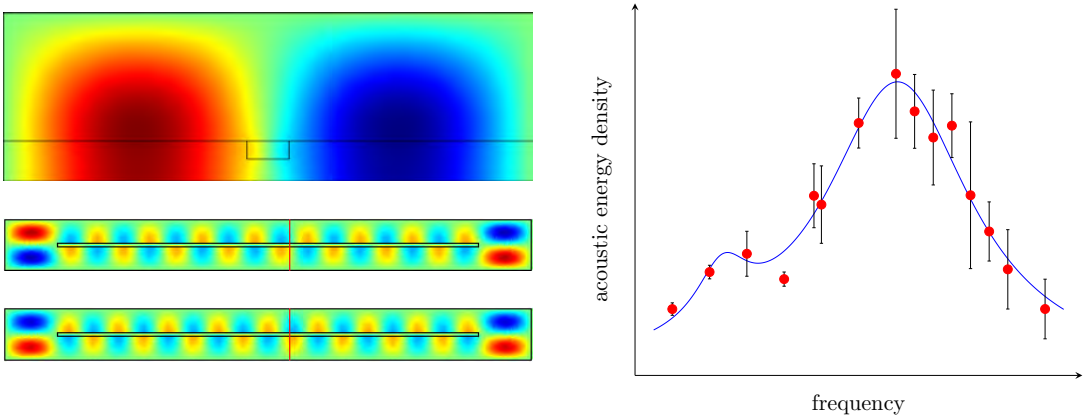

Supervisor: Professor Henrik Bruus

Department of Micro– and Nanotechnology
Technical University of Denmark

June 30, 2009

Frontpage illustration
The illustration at the frontpage shows (left) color plots by 2D and 3D models of acoustic resonances in a microchip, and (right) a Lorentzian shape line fit to experimentally measured acoustic energy density in a straight water-filled microchannel.

Abstract

The use of ultrasound standing waves for particle manipulation and separation has gained renewed interest and widespread use in the past decade since its application in the emerging field microfluidics.

In many silicon-based separation devices the so-called acoustic pressure force is utilized to separate particles in aqueous solutions by establishing transverse half-wavelength pressure modes in microchannels. In the present we work apply theoretical analyses and numerical simulations to investigate the acoustic resonances in such microchannels. A special emphasis is put on taking the surrounding chip material into account, thus going beyond the traditional transverse half-wavelength picture. We show that the localization of acoustic energy in the active channels can be optimized by choosing the width of the channel in the right proportion relative to the width of the surrounding silicon chip. This analysis provides a simple but important design tool, which is applied in numerical simulations of two application schemes; (*i*) a high throughput many-channel separation chip, and (*ii*) a three-channel chip for *in situ* calibration of the acoustic pressure force.

Moreover, we present modeling of a point-actuation device. We study how the position of a piezo transducer on the chip surface influences the acoustic resonances in the microchannels. For a fixed position of the point transducer, we analyze the total acoustic energy in the system as a function of the driving frequency, the radiative energy loss to the surroundings, and the viscous energy dissipation in the liquid. This work has led to the fabrication of a point-actuation device by our collaborators in the group of Laurell at Lund University. Additionally, we theoretically investigate the basic conditions for creating straight water-filled channels acting as acoustic waveguides in microchips.

In addition to the theoretical work, we present results from experiments carried out through visits in the laboratory in the group of Laurell. Here we obtained measurements of the acoustic energy densities and the corresponding Q-values of ultrasound resonances in microfluidic chips. The acoustic energy was obtained by tracking individual polystyrene microbeads undergoing acoustophoresis in straight water-filled channels in silicon/glass chips. From the measurements we obtain that the acoustic energy density as a function of applied frequency behaves as Lorentzian line shapes, and that the acoustic energy density scales with the applied transducer voltage to the power of two.

Resumé

Anvendelse af stående ultralydsbølger til partikelmanipulering og separation, har vundet ny interesse og udbredt anvendelse indenfor det seneste årti, siden dets udnyttelse i det hurtigt udviklende område, mikrofluidik.

I mange siliciums-baseret separationsaggregater benyttes den såkaldte akustiske trykkraft til at separere partikler opløst i en væske, ved at etablere en halv trykbølge på tværs af en mikrokanal. I dette arbejde anvender vi teoretisk analyse og numeriske simuleringer til at udforske de akustiske resonanser i sådanne mikrokanaler. Analyserne lægger stor vægt på at tage det omgivende chip materiale med i betragtning, og tager derfor skridtet videre fra det sædvanlige halvbølgebillede. Vi viser, at lokaliseringen af den akustiske energitæthed i de aktive kanaler kan optimeres ved at vælge passende dimensioner for kanalbredden i forhold til den omgivende siliciumschip. Dette har givet et simpelt men vigtigt designredskab, som vi benytter til numerisk analyse af to applikationer: (*i*) en mangekanals separationschip til opnåelse af høj gennemstrømning og (*ii*) en trekanals chip til *in situ* kalibrering af den akustiske trykkraft.

Ydermere præsenterer vi modellering af et punktaktueringsapparat. Vi studerer, hvordan positionen af en punktaktuator på chipoverfladen påvirker de akustiske resonanser i mikrokanalerne. For en fast position af punktaktuatoren analyserer vi den totale akustiske energitæthed i systemet som funktion af aktueringsfrekvens, tab af transmitteret energi til omgivelserne og tab af energi fra de viskøse gnidninger i væsken. Dette arbejde har resulteret i fremstillingen af sådan et punktaktueringsapparat af vores samarbejdspartnere i Laurells forskningsgruppe ved Lunds Universitet. Yderligere undersøger vi de teoretiske betingelser for at skabe lige vandfyldte mikrokanaler, som fungerer som akustiske bølgeledere i en mikrochip.

Udover det teoretiske arbejde præsenterer vi eksperimentielle resultater udført ved besøg hos Laurells gruppe. I disse forsøg har vi målt den akustiske energitæthed og tilsvarende Q-værdier for de akustiske resonanser i de mikrofluide chips. Den akustiske energitæthed er målt ved at følge partikelbanerne for polystyren mikropartikler udsat for akustophorese i lige vandfyldte kanaler i siliciumschips. Ved disse målinger finder vi, at den akustiske energitæthed som funktion af aktueringsfrekvens følger Lorentz-kurver, og at den akustiske energitæthed skalerer som kvadratet på spændingen over den aktuerende piezokrystal.

Preface

This thesis is submitted as fulfillment of the prerequisites for obtaining the degree in Master of Science in Engineering at the Technical University of Denmark (DTU). The thesis work is carried out at the Department of Micro- and Nanotechnology (DTU Nanotech) in the Theoretical Microfluidics group (TMF) headed by Professor Henrik Bruus. The duration of the thesis work was 10 months from 1 September 2008 to 30 June 2009 corresponding to a credit of 50 ECTS points.

During the project work many people have been of great help and support. First of all, I would like to thank my supervisor Henrik Bruus for his huge enthusiasm when supervising his students, as well as his eager to understand the world of physics. Henrik has been of magnificent inspiration with his large knowledge, but also with his competences in scientific writing and professional working approaches.

In part of the project I carried out experiments in Professor Thomas Laurell's laboratory at the Department of Electrical Measurements (Elmat), Lund University (LTH), during eight days in April and May. I would like to thank Professor Thomas Laurell, his entire research group and especially PhD student Per Augustsson for great collaboration, help and assistance in the laboratory. I find the atmosphere very pleasant in the Swedish group and I look forward to further collaboration in my continuation of the project as a PhD student.

I would like to thank the three BSc students (known as the Gorkov-boys), Lasse Mejling Andersen, Anders Nysteen and Mikkel Settnes, for many fruitful discussions on the acoustic pressure force and for their inspirational enthusiasm and skills within physics. Moreover, I would like to thank the TMF group for an exceptional working atmosphere being both professional and social rewarding. I also thank DTU Nanotech for a pleasant and positive working environment and my fellow student Mathias Bækbo Andersen for his superb support and company throughout the entire period of the studies at DTU.

At last I would like to thank my family and friends for their support throughout the project.

Rune Barnkob
Department of Micro– and Nanotechnology
Technical University of Denmark
30 June 2009

Contents

List of Figures

List of Tables

List of Symbols

Symbol	Description	Unit
$\equiv$	Equal to by definition	
$\sim$	Of the same order	
$\approx$	Approximately equal to	
$\propto$	Proportional to	
$\ll, \gg$	Much smaller than, much greater than	
$\cdot$	Scalar product	
$\times$	Cross-product or multiplication sign	
$\partial_i = \partial/\partial_i$	Partial derivative with respect to i	$[i]^{-1}$
$\boldsymbol{\nabla}$	Nabla or gradient vector operator	m^{-1}
$\boldsymbol{\nabla}\cdot$	Divergence vector operator	m^{-1}
$\boldsymbol{\nabla}\times$	Rotation vector operator	m^{-1}
∇^2	Laplacian scalar operator	m^{-2}
$\mathcal{O}(x^n)$	Terms of order x^n and higher powers	
$\langle\circ\rangle$	Time average of $\circ$	
$\langle\circ\rangle_i$	Average of $\circ$ over i	
$\lvert\circ\rvert$	Absolute value of $\circ$	
$(\circ)^*$	Complex conjugate of $\circ$	
$\Delta\circ$	A change in $\circ$	
$\delta\circ$	An infinitesimal change in $\circ$	
$\mathrm{Re}\{\circ\}$	Real part of $\circ$	
$\mathrm{Im}\{\circ\}$	Imaginary part of $\circ$	
i	Imaginary unit	
e	Euler's constant, $\ln(\mathrm{e}) = 1$	
x, y, z	Rectangular coordinates	
$\mathbf{e}_i$	Unit vector in i-direction	
$\boldsymbol{r}$	Position vector	m
$\boldsymbol{n}$	Surface normal vector	m
Ω	Domain of interest	
$\mathrm{d}\Omega$	Boundary of domain Ω	

Continued on next page

Symbol	Description	Unit
a_n	Normal acceleration	$\mathrm{m\,s^{-2}}$
$\boldsymbol{g}, g$	Gravitational acceleration	$\mathrm{m\,s^{-2}}$
l, L	Length of channel, length of chip	m
w, W	Width of channel, width of chip	m
h, H	Height of channel, height of chip	m
a	Radius of spherical particle	m
R	Radius of point transducer or fixation pin	m
V	Volume	$\mathrm{m^3}$
ℓ	Actuator displacement	m
α_{per}	Perturbation parameter	m
p_i	i'th order acoustic pressure	$\mathrm{kg\,m^{-1}s^{-2}}$
ρ_i	i'th order acoustic mass density	$\mathrm{kg\,m^{-3}}$
v_i	i'th order acoustic velocity	$\mathrm{m\,s^{-1}}$
$\boldsymbol{v}_i$	i'th order acoustic velocity vector	$\mathrm{m\,s^{-1}}$
ϕ_i	i'th order velocity potential	$\mathrm{m^2\,s^{-1}}$
t	Time	s
f	Frequency	$\mathrm{s^{-1}}$
$\omega = 2\pi f$	Angular frequency	$\mathrm{s^{-1}}$
$\tau = 1/f$	Period	s
n_i	Number of $\lambda/2$ in spatial direction i	
λ	Acoustic wavelength	m
λ^*	Perfect $\lambda/2$-mode wavelength	m
δ	Relative change in wavelength	
α	Aspect ratio parameter	
$\boldsymbol{k}$	Complex-valued wave vector	$\mathrm{m^{-1}}$
$\boldsymbol{k}_0$	Real-valued wave vector	$\mathrm{m^{-1}}$
θ	Dimensionless wavenumber	
c_a	Speed of sound in material a	$\mathrm{m\,s^{-1}}$
Z_a	Acoustic impedance of material a	$\mathrm{kg\,m^{-2}s^{-1}}$
z	Acoustic impedance ratio	
p_{A}, A_j	Pressure amplitudes	$\mathrm{kg\,m^{-1}s^{-2}}$
Q	Q-value of acoustic resonance peak	
Δf_i	FWHM of frequency for the i'th resonance	$\mathrm{s^{-1}}$
Δf	Frequency shift between two resonance peaks	$\mathrm{s^{-1}}$

Continued on next page

Symbol	Description	Unit
E_{ac}	Time-averaged acoustic energy density	$\mathrm{kg\,m^{-1}s^{-2}}$
$\mathcal{E}_{\mathrm{ac}}$	Spatially- and time-averaged energy density	$\mathrm{kg\,m^{-1}s^{-2}}$
$\tilde{c}$	Speed of sound ratio	
$\tilde{\rho}$	Density ratio	
$f_1,\, f_2$	Pre-factors in pressure force expression	
U_0	Amplitude of acoustic potential	$\mathrm{kg\ m^2\,s^{-2}}$
U_{ac}	Time-averaged acoustic pressure force potential	$\mathrm{kg\ m^2\,s^{-2}}$
$\boldsymbol{F}_{\mathrm{ac}}$	Time-averaged acoustic pressure force vector	$\mathrm{kg\ m\,s^{-2}}$
$\boldsymbol{F}_{\mathrm{drag}}$	Stokes drag force vector	$\mathrm{kg\ m\,s^{-2}}$
$\boldsymbol{F}_{\mathrm{g}}$	Gravitational force vector	$\mathrm{kg\ m\,s^{-2}}$
η	Viscosity	$\mathrm{kg\,m^{-1}s^{-1}}$
$\beta\eta$	Bulk viscosity	$\mathrm{kg\,m^{-1}s^{-1}}$
γ	Viscous damping factor	
U_{pp}	Driving peak-to-peak voltage	$\mathrm{kg\ m^2\,C^{-1}\,s^{-2}}$
Z_{el}	Electric impedance	$\mathrm{kg\ m^2\,C^{-2}\,s^{-1}}$
ϕ_{el}	Electric phase	
k_{B}	Boltzmann's constant	$\mathrm{kg\ m^2\,s^{-2}\,K^{-1}}$
T	Temperature	K
D	Diffusion constant	$\mathrm{m^2\,s^{-1}}$
l_{diff}	Diffusion length	m
N, M	Number of measurements	
$\bar{x}$	Weighted mean of variable x	
s_x	Sample standard deviation of variable x	
σ_x^2	Variance of variable x	
$\boldsymbol{u}$	Displacement vector	m
$\boldsymbol{\sigma}$	Cauchy stress tensor	$\mathrm{kg\,m^{-1}s^{-2}}$
λ_{iklm}	Elasticity tensor	$\mathrm{kg\,m^{-2}s^{-2}}$
c_{L}	Longitudinal sound velocity (elastic theory)	$\mathrm{m\,s^{-1}}$
c_{T}	Transverse sound velocity (elastic theory)	$\mathrm{m\,s^{-1}}$
c_{av}	Average sound velocity (elastic theory)	$\mathrm{m\,s^{-1}}$
E	Young's modulus	$\mathrm{kg\,m^{-1}s^{-2}}$
ν	Poisson's ratio	

Chapter 1

Introduction

In this chapter we introduce the concepts of acoustofluidics; the art of combining acoustics with microfluidics to obtain handling and manipulation tools for lab-on-a-chip systems. We briefly review the experimental as well as the theoretical state-of-the-art within acoustofluidics. Next, we point out the needs for theoretical insight, and thus the motivation for carrying out this thesis work.

1.1 Lab-on-a-chip systems

Lab-on-a-chip technology concerns the scaling down of laboratory setups below millimeter scale or smaller. It is a product of the invention of microelectronic chips, which during the past 50 years has led to an entirely new framework within micro- and nanofabrication. The obvious advantages of lab-on-a-chip systems are (*i*) the allowance of small sample quantities and volumes which is often encountered in modern biology and biotechnology, (*ii*) fast biological and chemical reactions and processes due to the high surface to volume ratios, (*iii*) increased possibilities for developing compact and portable point-of-a-care devices, and (*iv*) the utilization of mass production to manufacture cheap devices.

Lab-on-a-chip systems are often incorporating microfluidics, which is the technology of handling fluids on sub-millimeter scales. Dealing with fluids on this scale induces different physics than observed on a macroscopic scale. Microflows are in particular characterized by having a very low Reynolds number (on the order of unity or smaller), corresponding to highly laminar flows, where viscous forces dominate. The laminar flow ensures that flow streamlines do not cross, which leads to high controllability when handling microfluidic systems. But the introduction of laminar flow leads to new challenges, e.g. the missing ability to mix fluids by turbulence. This and other challenges has led to research within areas such as pumping, detection and mixing, utilizing various techniques such like electroosmostic pumping, magnetophoresis, electrophoresis and geometrically controlled mixing. For textbooks and review papers on microfluidics, see [1–8].

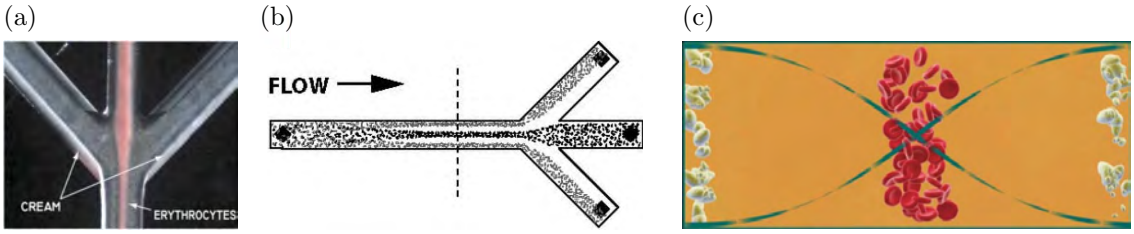

Figure 1.1: (a,b) Illustration of highly functional acoustic separation device to split red blood cells from lipids by utilizing standing acoustic waves in combination with laminar microfluidic flow and a three way flow splitter (trifurcation). (c) Sketch of the traditional transverse half-wavelength picture and the separation of blood cells (node) and lipids (antinodes). Illustrations are from Petersson *et al.* [24, 25].

1.2 Acoustofluidics

Another technique for manipulation and separation is the use of acoustics in fluids leading to the field acoustofluidics. Primarily two non-linear effects are of importance, namely the acoustic pressure force and the acoustic streaming. The acoustic pressure is a time-averaged force acting on particles or cells as they are exposed to an acoustic field. The resulting particle motion is called acoustophoresis. Acoustic streaming is time-averaged motion of the entire carrier fluid due to energy transfer from the acoustic field. Both the acoustic pressure force and acoustic streaming has been known since their description by Faraday in 1831 [9]. Regarding the acoustic pressure force, Kundt is often cited for the demonstration by his famous cork dust experiment in 1874 [10], known as Kundt's tube for determination of the speed of sound in gases. Both phenomena has been theoretically treated in the past [11–23].

1.3 Experimental motivation

The field of acoustofluidics has received renewed interest in the past decade since its application in microfluidics, where the geometric length scales are in the sub-millimeter regime thus requiring acoustic waves in the ultrasonics regime when dealing with water. The research area is constantly developing, as the method is a promising tool for gentle manipulation of cells and particles. Among many already suggested applications are pumping, trapping and sorting devices [24–40]. It is common for the ongoing research that it has mainly been based on experimental studies, while equivalent theoretical understanding is lacking. Most of the research relies on a silicon chip containing an etched channel or cavity structure, which is then bonded with a transparent lid of pyrex glass attached to make visual inspection possible. One or more external piezo transducers are attached and an acoustic resonance pattern is induced in the channels or cavities by tuning the driving frequency of the transducer(s). By careful design of the device geometry, different resonance properties can be achieved.

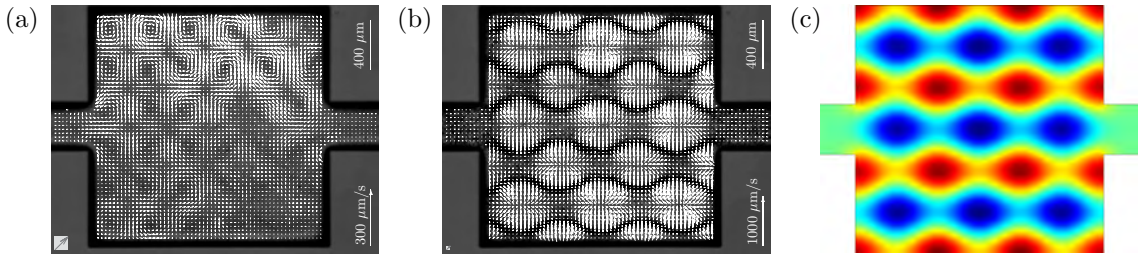

Figure 1.2: (a,b) Experimental images obtained by particle image velocimetry (PIV) from Hagsäter *et al.* [37] at DTU. The images show (a) the acoustic streaming of 1 μm beads and (b) acoustic pressure forces on 5 μm beads. (c) Modeling image of the acoustic pressure for both image (a) and (b); red areas correspond to positive pressures, whereas blue areas correspond to negative pressures. The acoustic streaming and pressure forces occur simultaneously and for same acoustic resonance. Thus the acoustic streaming dominates for small particles, while the acoustic pressure force dominates for larger particles.

Separation of blood cells and fat particles

In 2004 pioneering work within sorting of microparticles was done in the group of Laurell at Lund University, Sweden [24, 25, 32]. Ultrasonic waves from a piezo transducer was for the first time used in combination with a microchannel trifurcation to obtain separation of blood cells from lipid particles, see Fig. 1.1 (a). This application can be a major advancement within e.g. cardiovascular surgery, where it is of crucial importance to be able to clean patients blood from fat particles in a fast, continuous and efficient way.

The now well-known separation technique makes use of the acoustic pressure force, which forces particles to either pressure nodes or pressure antinodes depending on their acoustic properties, such as their size, density and compressibility relative to those of the surrounding fluid. Red blood cells and lipid particles have opposite acoustophoretic properties: the red blood cells move towards the pressure nodes, while conversely the lipids move to the pressure antinodes. To separate the particles a standing half-wavelength pressure mode is applied across a liquid-filled channel with the node in the center of the channel and the antinodes at the channel walls, namely a so-called antisymmetric (odd) mode, see Fig. 1.1 (c). Pumping an axial laminar flow, while acoustic actuating transversely, then separates the particles. The laminar flow is divided by a three way flow splitter (trifurcation) at the end of the channel thus separating the different types of particles, see Fig. 1.1 (b).

The half-wavelength pressure mode is applied by matching the channel width w with respect to the applied actuation frequency f as $f = c_a/(2w)$, where c_a is the speed of sound in the liquid-filled channel. This approximation comes from a simple analytical estimate based only on the channel in one dimension as being the acoustic resonator. By the application discussed above and many others, this traditional transverse half-wavelength picture has proven to be well defined in chip designs of low geometric complexity. Though, thorough theoretical as well as experimental determination of its limitations still remain to be done.

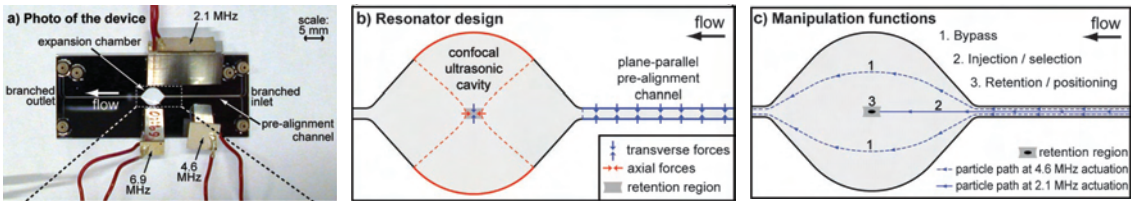

Figure 1.3: Demonstration of selective retention and positioning of cells by ultrasonic manipulation in a microfluidic chamber done by collaboration between the group of Wiklund at KTH and the group of Bruus at DTU. The images are from Svennebring *et al.* [40].

Acoustic effects in microsystems

At DTU in 2007 Hagsäter *et al.* [37] studied experimentally the acoustic effects on particles in liquid-filled microchambers, see Fig. 1.2. By using microparticle image velocimetry (PIV) the transient behavior was recorded, when applying an acoustic field to a silicon chip with a liquid-filled cavity. At a specific acoustic resonance is was shown that the acoustic streaming dominates for small particles, whereas the acoustic pressure force dominates for larger particles.

Acoustic cell handling

Acoustic handling of cells has been extensively studied in the group of Wiklund at KTH, Sweden. In 2009 they demonstrated selective retention and positioning of cells by ultrasonic manipulation in a microfluidic chamber backed up by a theoretical analysis done in the group of Bruus at DTU [40]. They utilized a confocal chamber to establish a centered ultrasonic force field, where they were able to acoustically trap cells as well as demonstrate several other manipulation functions, see Fig. 1.3. Moreover the Wiklund/Bruus team presented in 2009 the ability to spatially separate and confine particle tracks by the use of multiple piezo transducers [39].

1.4 Theoretical foundation and goals

The aim of the current thesis work is to continue the theoretical work done in the group of Bruus at DTU by the two former MSc students, Thomas Glasdam Jensen (TGJ) [41] and Peder Skafte-Pedersen (PSP) [42]. TGJ inialitized the theoretical work on acoustofluidics at DTU Nanotech analyzing the results by Hagsäter *et al.* [37] as presented in Fig. 1.2. In the following MSc project by PSP a thorough analysis of the theoretical background was carried out. Here, PSP showed that energy loss due to transmission of waves plays a major role in the description of the acoustic streaming. Additionally, PSP carried out calculations directly related to the work done in the group of Laurell [38] and the group of Wiklund [40], see Fig. 1.3 and 1.4. Futhermore, during the work of this thesis, three bachelor students Lasse Mejling Andersen, Anders Nysteen and Mikkel Settnes, have worked extensively on treating the trajectories of particles subject to acoustic pressure forces [43].

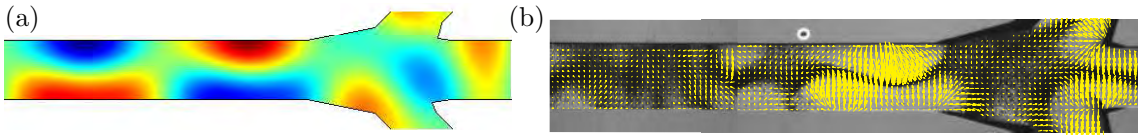

Figure 1.4: Demonstration of (a) color plot (red is positive, blue is negative) of calculated resonance mode corresponding to (b) PIV measurements of a separation chip done in collaboration between the group of Laurell at LTH and the group of Bruus at DTU. The images are from Hagsäter *et al.* [38].

It is clear from the former theoretical work that more extensive resonator models are needed to describe the acoustic pressure fields and energies and thus to understand the acoustic forces. The treatment of acoustic resonances is the main objective of the current thesis. Enabling better understanding of the resonances leads to the possibility to optimize and design future acoustofluidic applications. In these studies we put emphasis on taken into account the physics of the full experimental silicon/glass chip. We give a detailed theoretical analysis of the usual half-wavelength assumption and the relative acoustic energy densities in a silicon/water chip system.

Besides the theoretical work, a part of the thesis has been to carry out simple experiments in the laboratory of the group of Laurell. In this work some of the theoretical predictions were tested and the acoustic energy density was investigated.

1.5 Outline of the thesis

Chap. 2: Governing acoustofluidic theory

We set up the framework of the thesis by introducing the governing acoustofluidic equations. We describe the first-order theory and discuss the acoustic energies and boundary conditions for an acoustic resonator system. Moreover, we analyze the simple analytical resonator example of a single-domain box. Though it is not utilized in the thesis work, we set up the governing elastic equations for isotropic solids, as the experimental work in this thesis has indicated a need for this in future work.

Chap. 3: Numerical simulations in Comsol Multiphysics

The finite element software Comsol Multiphysics is the main tool in this thesis work. Numerical analysis is needed as we consider acoustic resonances of multi-domain systems of complex geometries. This chapter describes the basic concepts for the use of Comsol in this work. It presents an example of an implemented script, and the benchmarking of the script to analytical results.

Chap. 4: Actuation and energy losses

We investigate the influence of taking into account the acoustic energy losses due to radiation of waves to the surroundings and to internal viscous attenuation in a three-dimensional (3D) model system. We discuss the validity of the perturbation approach

and the theoretical prediction of a Lorentzian line-shape fit for energies in lossy systems. Finally, we examine a model system of a point-actuated silicon chip with an internal water-filled microchamber.

Chap. 5: Anti-symmetric single-channel system

In this chapter we study the usual transverse half-wavelength picture. We carry out comprehensive analyses by one-dimensional (1D) and two-dimensional (2D) calculations of the acoustic pressure eigenmodes in a multi-domain chip system. We end the chapter by extending the analysis by 3D COMSOL calculations, and we introduce translational invariant chips.

Chap. 6: Many-channel chips

We carry out two-dimensional COMSOL calculations in order to investigate many-channel systems, which is of high interest due to the need of high throughput in separation devices. Finally, we suggest a three-channel *in situ* calibration chip to measure the acoustic energy density in a given separation chip.

Chap. 7: Waveguide analysis

As a preliminary treatment for future work, we investigate the conditions for a water-filled channel to act as an acoustic waveguide in a surrounding silicon/glass chip. The conditions are tested by 2D and 3D COMSOL models.

Chap. 8: Experimental investigations

Experiments have been carried out at Lund University in collaboration with the group of Laurell. We present investigations of (*i*) the electrical impedances of the piezo transducer, (*ii*) the sedimentation of polystyrene particles, and (*iii*) measurements of the acoustic energy density. Finally, the experiments have acted as an eye-opener to the actual laboratory conditions, which are important to keep in mind when carrying out theoretical analyses.

1.6 Publications during the MSc thesis studies

Peer-reviewed conference proceedings

1. Rune Barnkob, and Henrik Bruus, "Acoustofluidics: theory and simulation of radiation forces at ultrasound resonances in microfluidics devices", ASA 2009,
   Paper no. 2pBB2 in the *157th meeting of the Acoustical Society of America*, Portland, Oregon, 18-22 May 2009

Other conference proceedings

1. Rune Barnkob, and Henrik Bruus, "Theoretical analysis of ultrasound resonances in lab-on-a-chip systems", DFS 2009, *Danish Physical Society, Nordic Meeting*, Copenhagen, 16-18 June 2009

Chapter 2

Basic theory

In this chapter we describe the governing equations of acoustofluidics, which is the foundation for the work presented in the current thesis. The thesis work is based on the simple pressure wave model, where all media are modeled as liquids only sustaining pressure waves and not any shear waves. This is of course not accurate when with dealing elastic solids such as silicon and pyrex glass, however the main qualitative features can be studied. At the end of this chapter we briefly describe the full theory of elastic waves in isotropic solids.

The fundamental acoustofluidic theory is summarized mainly based on acoustic theory found in Lighthill [44], and the theoretical aspects of acoustics in microfluidics found in Bruus [5] and Skafte-Pedersen [42].

2.1 Governing acoustofluidic equations

The governing equations of fluid dynamics are derived from conservation laws, Newtons second law and the continuum hypothesis. The governing equations are the dynamic Navier–Stokes equation for a compressible viscous Newtonian fluid; the kinematic continuity equation; and the thermodynamic equation of state relating pressure and density. Ignoring thermal effects for simplicity and using the Eulerian field description, they become

$$\rho\partial_t \boldsymbol{v} = -\boldsymbol{\nabla} p - \rho\big(\boldsymbol{v}\cdot\boldsymbol{\nabla}\big)\boldsymbol{v} + \eta\nabla^2\boldsymbol{v} + \beta\eta\boldsymbol{\nabla}\big(\boldsymbol{\nabla}\cdot\boldsymbol{v}\big), \tag{2.1a}$$

$$\partial_t \rho = -\boldsymbol{\nabla}\cdot\big(\rho\boldsymbol{v}\big), \tag{2.1b}$$

$$p = p\big(\rho\big), \tag{2.1c}$$

where $p = p(\boldsymbol{r},t)$ is the pressure field, $\rho = \rho(\boldsymbol{r},t)$ is the density field, $\boldsymbol{v} = \boldsymbol{v}(\boldsymbol{r},t)$ is the velocity field, η the viscosity and $\beta \approx 5/3$ is the ratio between the compressional bulk viscosity and the dynamic viscosity. Together the governing equations comprise a set of non-linear coupled partial differential equations, which is hard to solve both analytically as well as numerically. In the following the equations are combined to derive the approximate linear acoustic wave equation. This is done using perturbation theory as

the acoustic pressure waves are generated by slightly perturbing the equilibrium pressure in a compressible fluid.

2.1.1 Perturbation of governing equations

For a compressible fluid we consider a quiescent state $\{p_0,\rho_0,\boldsymbol{v}_0\}$, which corresponds to a homogeneous liquid at rest and in thermal equilibrium. The velocity in the quiescent state is zero $\boldsymbol{v}_0 = \boldsymbol{0}$ and the density and pressure are constants. The pressure p_0 in the quiescent state corresponds to the internal energy per volume in the fluid, which for water corresponds to the energy per volume it takes to free a water molecule into the gas phase, which at room temperature is estimated to $p_0^{\mathrm{wa}} \approx 2.6 \times 10^9$ J m^{-3}.

Assuming the acoustic perturbations of the quiescent state are small, the pressure p, density ρ and particle velocity $\boldsymbol{v}$ can be written as the perturbation expansions

$$p = p_0 + p_1 + p_2 + \dots \,, \tag{2.2a}$$
$$\rho = \rho_0 + \rho_1 + \rho_2 + \dots \,, \tag{2.2b}$$
$$\boldsymbol{v} = \boldsymbol{0} + \boldsymbol{v}_1 + \boldsymbol{v}_2 + \dots \,, \tag{2.2c}$$

where the perturbation parameter α_{per} is made implicit. The first-order perturbation fields p_1, ρ_1 and $\boldsymbol{v}_1$ are the time-dependent linear fields describing the fundamental acoustic wave, whereas the second-order perturbation fields lead to time-independent effects such as the acoustic pressure force and the acoustic streaming.

Second-order Taylor expansion of Eq. (2.1c) in p around $p_0 = p(\rho_0)$ gives

$$p = p_0 + c_a^2\rho_1 + c_a^2\rho_2 + \frac{1}{2}\partial_\rho(c_a^2)\rho_1^2, \tag{2.3}$$

where the speed of sound c_a to first order in medium a has been introduced as the isentropic derivative

$$c_a^2 = \left(\frac{\partial p}{\partial \rho}\right)_s. \tag{2.4}$$

As we handle fluids, c_a is a longitudinal sound velocity. Fluids cannot sustain shear stresses and thus do not have transverse sound velocities.

2.1.2 Zeroth-order perturbation equations

Substituting the perturbation fields Eqs. (2.2) into the set of governing Eqs. (2.1) we obtain the zeroth-order equations

$$\boldsymbol{0} = -\boldsymbol{\nabla} p_0, \tag{2.5a}$$
$$\partial_t \rho_0 = 0, \tag{2.5b}$$
$$p = p_0, \tag{2.5c}$$

which are seen only to have solutions being constant zeroth-order terms.

2.1.3 First-order perturbation equations

Similarly considering the first-order terms we get the first-order equations

$$\rho_0 \partial_t \boldsymbol{v}_1 = -c_a^2 \boldsymbol{\nabla} \rho_1 + \eta \nabla^2 \boldsymbol{v}_1 + \beta \eta \boldsymbol{\nabla} \big(\boldsymbol{\nabla} \cdot \boldsymbol{v}_1 \big), \tag{2.6a}$$

$$\partial_t \rho_1 = -\rho_0 \boldsymbol{\nabla} \cdot \boldsymbol{v}_1, \tag{2.6b}$$

$$p_1 = c_a^2 \rho_1. \tag{2.6c}$$

2.1.4 Second-order perturbation equations

Considering only second order terms we obtain the second-order equations

$$\rho_0 \partial_t \boldsymbol{v}_2 = -\rho_1 \partial_t \boldsymbol{v}_1 - \rho_0 \big(\boldsymbol{v}_1 \cdot \boldsymbol{\nabla} \big) \boldsymbol{v}_1 - \boldsymbol{\nabla} p_2 + \eta \nabla^2 \boldsymbol{v}_2 + \beta \eta \boldsymbol{\nabla} \big(\boldsymbol{\nabla} \cdot \boldsymbol{v}_2 \big), \tag{2.7a}$$

$$\partial_t \rho_2 = -\rho_0 \boldsymbol{\nabla} \cdot \boldsymbol{v}_2 - \boldsymbol{\nabla} \cdot \big(\rho_1 \boldsymbol{v}_1 \big), \tag{2.7b}$$

$$p_2 = c_a^2 \rho_2 + \frac{1}{2} \partial_\rho (c_a^2) \rho_1^2. \tag{2.7c}$$

2.2 First-order acoustofluidics

To describe first-order linear acoustics, the first-order perturbation equations are used to derive the acoustic wave equation.

2.2.1 Inviscid theory

We first limit ourselves to consider the inviscid case by neglecting the viscous damping terms in Eqs. (2.6). Taking the divergence of the Navier–Stokes equation Eq. (2.6a) and inserting the continuity equation Eq. (2.6b) gives the wave equation for the density ρ_1

$$\partial_t^2 \rho_1 = c_a^2 \nabla^2 \rho_1. \tag{2.8}$$

By use of Eq. (2.6c) this leads to the wave equation for the pressure p_1

$$\partial_t^2 p_1 = c_a^2 \nabla^2 p_1. \tag{2.9}$$

Taking the gradient of Eq. (2.6b), inserting the inviscid case of Eq. (2.6a) and requiring an irrotational flow i.e. $\boldsymbol{\nabla} \times \boldsymbol{v} = \boldsymbol{0}$, the wave equation for the velocity $\boldsymbol{v}_1$ can be derived

$$\partial_t^2 \boldsymbol{v}_1 = c_a^2 \nabla^2 \boldsymbol{v}_1. \tag{2.10}$$

The assumption of an irrotational flow is valid for the important case of a velocity field varying time-harmonically as $\boldsymbol{v}_1 = \boldsymbol{v}_1(\boldsymbol{r})\, \mathrm{e}^{-\mathrm{i}\,\omega t}$, where $\omega = 2\pi f$ is the angular frequency and f the frequency. This is directly seen from the fact that $\boldsymbol{v}_1$ becomes a gradient field when substituted into Eq. (2.6a). Note that the assumption of a time-harmonically varying solution changes the time-differential operator into a simple multiplicative factor $\partial_t \to -\mathrm{i}\omega$.

In order to connect the three fields ρ_1, p_1 and $\boldsymbol{v}_1$, we use the irrotational nature of $\boldsymbol{v}_1$ to introduce the first-order velocity potential ϕ_1. Inserting the velocity potential into

Eq. (2.6a) and integrating gives the connection to ρ_1 and p_1. The definition of the velocity potential and the connections to ρ_1 and p_1 read

$$\boldsymbol{v_1} \equiv \boldsymbol{\nabla}\phi_1, \tag{2.11a}$$

$$\rho_1 = -\frac{\rho_0}{c_a^2}\partial_t\phi_1, \tag{2.11b}$$

$$p_1 = -\rho_0\partial_t\phi_1. \tag{2.11c}$$

Assuming time-harmonic solutions and rearranging yields $\boldsymbol{v}_1$ directly in terms of p_1 or ρ_1

$$\boldsymbol{v}_1 = -\frac{\mathrm{i}}{\omega\rho_0}\,\boldsymbol{\nabla}p_1 = -\frac{\mathrm{i}c_a^2}{\omega\rho_0}\,\boldsymbol{\nabla}\rho_1. \tag{2.12}$$

Finally, inserting Eq. (2.11a) into Eq. (2.6b) and utilizing the just presented connective equations leads to the general wave equation in ϕ_1

$$\partial_t^2\phi_1 = c_a^2\nabla^2\phi_1. \tag{2.13}$$

Plane waves and the Helmholtz equation

A commonly encountered solution to the wave equation is the harmonic plane wave, here given for p_1 and using the complex notation,

$$p_1 = p_\mathrm{A}\,\mathrm{e}^{\mathrm{i}(\boldsymbol{k}_0\cdot\boldsymbol{r}-\omega t)}, \tag{2.14}$$

where p_A is the pressure amplitude and $\boldsymbol{k}_0$ is the real-valued wave vector parallel to the direction of propagation. To fulfill the wave equation Eq. (2.9), we get the linear dispersion relation

$$\omega = c_a k_0. \tag{2.15}$$

Keeping the spatial dependence implicit and inserting a time-harmonic solution of the form

$$p_1 = p_1(\boldsymbol{r})\,\mathrm{e}^{-\mathrm{i}\,\omega t} \tag{2.16}$$

into the wave equation Eq. (2.9) yields the Helmholtz equation

$$\nabla^2 p_1(\boldsymbol{r}) = -k_0^2\,p_1(\boldsymbol{r}). \tag{2.17}$$

With a given set of boundary conditions, the Helmholtz equation sets up a classical eigenvalue problem which only allows certain values of the eigenvalue k_0^2 and its corresponding eigenmode $p_1(\boldsymbol{r})$. Using the dispersion relation Eq. (2.15) the eigenfrequencies can be found from $f = \omega/(2\pi) = c_a k_0/(2\pi)$. This current thesis heavily relies on the Helmholtz equation for determination of eigenmodes or resonance states for systems of different composition, geometry and boundary conditions. It is important to note that an eigenvalue problem does not allow the given system to be subject to energy losses e.g. due to viscous attenuation or radiation of waves at boundaries.

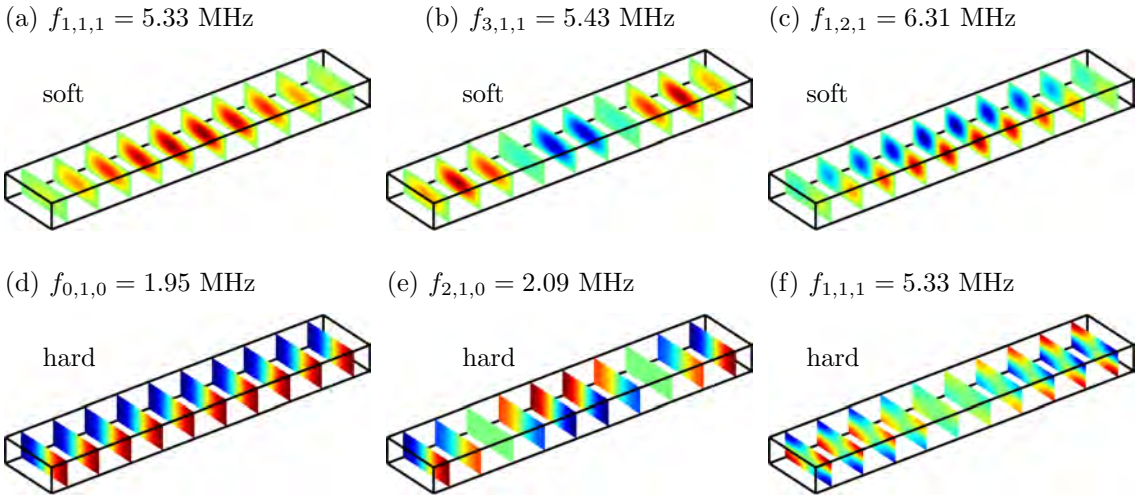

Figure 2.1: Sliced color plot of resonance pressure fields p_1 (red is positive, blue is negative, green is neutral) for a water-filled microchannel of length $l = 2$ mm along x, width $w = 380$ µm along y and height $h = 150$ µm along z. The speed of sound in water is $c_{\mathrm{wa}} = 1483\ \mathrm{m\,s^{-1}}$ as given in Table 2.1. (a,b,c) The water-filled channel is surrounded by an infinitely soft acoustic material making the pressure going to zero at all boundaries, see Eq. (2.19). (a) Resonance $(n_x, n_y, n_z) = (1, 1, 1)$ with $f_{1,1,1} = 5.33$ MHz, (b) $(n_x, n_y, n_z) = (3, 1, 1)$ with $f_{3,1,1} = 5.43$ MHz and (c) $(n_x, n_y, n_z) = (1, 2, 1)$ with $f_{1,2,1} = 6.31$ MHz. (d,e,f) The water-filled channel is surrounded by an infinitely hard acoustic material, see Eq. (2.20). (d) Resonance $(n_x, n_y, n_z) = (0, 1, 0)$ with $f_{0,1,0} = 1.95$ MHz, (e) $(n_x, n_y, n_z) = (2, 1, 0)$ with $f_{2,1,0} = 2.09$ MHz and (f) $(n_x, n_y, n_z) = (1, 1, 1)$ with $f_{1,1,1} = 5.33$ MHz.

2.2.2 Single-domain analysis of water cube

We now consider a specific geometrical setup forming an acoustic resonator. Having an acoustic resonator Ω implies that acoustic resonances (or eigenmodes) occurs for certain specific frequencies $f_j = \omega_j/(2\pi)$. An acoustic resonance at angular frequency ω_j is a state where the acoustic energy density E_{ac} inside the resonator is several orders of magnitude larger than at other frequencies $\omega \neq \omega_j$. In the general case, the resonance frequencies can only be calculated using numerical methods, however, in few cases they may be found analytically.

A simple example of an acoustic resonator is that of a 3D single-domain rectangular box, of which the single-domain plane (2D) and single-domain line (1D) are special cases. Applying the rectangle faces with either zero pressure (soft wall) or zero velocity (hard wall), yields an eigenvalue problem easily solved analytically by applying the method of separation of variables.

As an example we consider a rectangular water-filled channel placed in a silicon chip along the coordinate axes with its opposite corners at $(0, 0, 0)$ and (l, w, h). The silicon chip is surrounded by acoustically soft air. If we imagine that the surrounding silicon chip is infinitely thin, we thus have the water in direct acoustic contact with the air, which is well-approximated by the soft wall condition at all boundaries. Oppositely, if we imagine

the surrounding silicon chip to be acoustically infinitely hard material, we apply the hard wall condition at all boundaries. In both cases the eigenvalue solution to the Helmholtz equation in Eq. (2.17) becomes

$$f_{n_x,n_y,n_z} = \frac{c_{\mathrm{wa}}}{2}\sqrt{\frac{n_x^2}{l^2}+\frac{n_y^2}{w^2}+\frac{n_z^2}{h^2}}, \quad n_x, n_y, n_z = 1, 2, 3, \ldots, \tag{2.18}$$

where the three indexes n_x, n_y, n_z are the number of half-wavelengths in x, y and z, respectively. For pure soft boundary conditions, the corresponding eigenfunction p_1^{soft} becomes

$$p_1^{\mathrm{soft}}(x,y,z) = p_{\mathrm{A}} \sin\left(n_x\pi\frac{x}{l}\right)\sin\left(n_y\pi\frac{y}{w}\right)\sin\left(n_z\pi\frac{z}{h}\right), \quad n_x, n_y, n_z = 0, 1, 2, 3, \ldots, \tag{2.19}$$

whereas for pure hard conditions the corresponding eigenfunction p_1^{hard} is

$$p_1^{\mathrm{hard}}(x,y,z) = p_{\mathrm{A}} \cos\left(n_x\pi\frac{x}{l}\right)\cos\left(n_y\pi\frac{y}{w}\right)\cos\left(n_z\pi\frac{z}{h}\right), \quad n_x, n_y, n_z = 1, 2, 3, \ldots, \tag{2.20}$$

where p_{A} is the pressure amplitude. In Fig. 2.1 are seen examples of the resonant ultrasound waves for the rectangle having pure soft boundary conditions and pure hard boundary conditions, respectively. We notice how the largest contribution to the frequency stems from the modes along the small dimensions as given from Eq. (2.18).

2.2.3 Viscous theory

We move on by including viscous attenuation. Using same approach as in the inviscid case we obtain the modified wave equation for the pressure p_1

$$\partial_t^2 p_1 = c_a^2\nabla^2 p_1 + \frac{1}{\rho_0}[1+\beta]\eta\nabla^2(\partial_t p_1). \tag{2.21}$$

Note the mixed time and space derivatives in the last term representing the effects of viscosity.

Lossy Helmholtz equation

Assuming a time-harmonic first-order pressure field of the form $p_1 = p_1(\boldsymbol{r})\,\mathrm{e}^{-\mathrm{i}\,\omega t}$ leads to the lossy Helmholtz equation,

$$\nabla^2 p_1(\boldsymbol{r}) = -k^2 p_1(\boldsymbol{r}), \tag{2.22}$$

where the wave vector k now is complex

$$k = k_0\frac{1}{\sqrt{1-\mathrm{i}\,2\gamma}} \approx k_0(1+\mathrm{i}\gamma), \tag{2.23}$$

Table 2.1: Acoustic parameters for various materials considered in the thesis. All sound velocities are longitudinal sound velocities. Values for air, water, pyrex glass, polystyrene and iron are from [45]. Values for silicon and PMMA are from [41]. The values are given at $T = 20$ °C. In the last part of the table, the viscous parameters for water are given from [5].

Material (j)	density ρ_j [kg m^{-3}]	speed of sound c_j [m s^{-1}]	impedance $Z_j = \rho_j c_j$ [kg m^{-2} s^{-1}]
air (air)	1.16	343.4	3.99×10^5
water (wa)	998	1483	1.48×10^6
silicon (si)	2331	8490	1.98×10^7
pyrex glass (py)	2230	5640	1.25×10^7
PMMA polymer (PMMA)	1190	1588	1.89×10^6
polystyrene (ps)	1050	2350	2.47×10^6
iron (iron)	7874	5950	4.03×10^7
copper (cu)	8960	3750	3.36×10^7
aluminum (al)	2700	6420	1.73×10^7

Dynamic viscosity, water	η	1.0	mPa s
Bulk viscosity, water	$\beta\eta$	1.7	mPa s

where we have introduced the dimensionless viscous damping coefficient γ,

$$\gamma \equiv \frac{(1+\beta)\eta\omega}{2\rho_0 c_a^2}. \tag{2.24}$$

Considering MHz ultrasonics in water gives $\gamma \approx 10^{-5}$, and we thus use $k = k_0(1 + \mathrm{i}\gamma)$ throughout the thesis. The difference between the inviscid and viscous equations is the change in wave vector $k_0 \to k_0(1 + \mathrm{i}\gamma)$. If we consider the inviscid case $\gamma = 0$, the lossy Helmholtz Eq. (2.22) reduces to the Helmholtz Eq. (2.17).

Possible solutions to the lossy Helmholtz equation are damped harmonic plane waves, which are found directly by substituting k_0 with $k_0(1 + \mathrm{i}\gamma)$ in Eq. (2.14)

$$p_1 = p_\mathrm{A} \mathrm{e}^{\mathrm{i}(\boldsymbol{k}_0\cdot\boldsymbol{r}-\omega t)} \mathrm{e}^{-\gamma \boldsymbol{k}_0\cdot\boldsymbol{r}} = p_1(\boldsymbol{r}) \mathrm{e}^{-\mathrm{i}\,\omega t} \mathrm{e}^{-\gamma \boldsymbol{k}_0\cdot\boldsymbol{r}}. \tag{2.25}$$

These waves are damped on the length-scale of $1/(k_0\gamma) \approx 100$ m. Since the system contains energy losses, an external driving force has to be applied in order to sustain time-harmonic motion. As described in later chapters, this is done experimentally by applying an AC driving voltage at MHz frequency to a piezo transducer, which then vibrates with a time-harmonical acceleration $a\,\mathrm{e}^{-\mathrm{i}\,\omega t}$ and thereby induces an ultrasound pressure field into the system. In order to investigate systems yielding energy losses, we have to solve the given system in time. This will be be introduced in Chap. 4 on acoustic actuation.

The wave equation does not cover the case of arbitrary perturbation velocities. We are therefore limited to consider irrotational velocity fields, $\boldsymbol{\nabla} \times \boldsymbol{v} = \boldsymbol{0}$, which can be shown to be valid for time-harmonic fields and to first-order in the viscosity η. As in the inviscid case we again express the velocity by a first-order scalar potential ϕ_1 as in Eq. (2.11a).

Using same approach as in the inviscid case the connection between the three fields ρ_1, p_1 and $\boldsymbol{v}_1$, can be shown to be

$$\boldsymbol{v_1} \equiv \boldsymbol{\nabla}\phi_1, \tag{2.26a}$$

$$\rho_1 = -\frac{\rho_0 k^2}{\omega^2}\partial_t\phi_1, \tag{2.26b}$$

$$p_1 = -\frac{c_a^2\rho_0 k^2}{\omega^2}\partial_t\phi_1. \tag{2.26c}$$

Finally utilizing this, the lossy Helmholtz equation can be derived for ϕ_1

$$\nabla^2\phi_1 = -k^2\phi_1. \tag{2.27}$$

2.2.4 Acoustic energy density

The acoustic energy density can be used to indicate the strength of the acoustic fields of an acoustic resonator and to characterize the loss of acoustic energy due to viscous damping and radiation losses. Thus we need to define the acoustic energies in a resonator system. Employing the perturbation approach in Eq. (2.2) the lowest order acoustic energy densities become expressions of second order. The kinetic energy density is given by the standard formulation of kinetic energy for a fluid as

$$E_{\text{kin}} = \frac{1}{2}\rho_0 v_1^2 = \frac{1}{2}\rho_0(\boldsymbol{\nabla}\phi_1)^2, \tag{2.28}$$

whereas the potential energy is derived from the energy stored due to compression and expansion

$$E_{\text{pot}} = \int_{V_0}^{V}\frac{p_1}{V}\mathrm{d}V = \frac{1}{2}\frac{p_1^2}{c_a^2\rho_0}. \tag{2.29}$$

As we in the experiments do not resolve the fast oscillatory motion in ultrasonic waves in the MHz regime, we are interested in describing the time-averaged acoustic energy. The time average of a periodic function $f = f(t)$ is defined as

$$\langle f\rangle = \frac{1}{\tau}\int_t^{t+\tau} f\,\mathrm{d}t, \tag{2.30}$$

where τ is the time of a full oscillation period. This definition will also be used later when considering other second-order effects. Combining Eq. (2.28) and Eq. (2.29), the time-averaged acoustic energy density $E_{\text{ac}} = E_{\text{ac}}(\boldsymbol{r})$ becomes

$$E_{\text{ac}} = \frac{1}{2}\rho_0\left[\langle|\boldsymbol{v}_1|^2\rangle + \frac{1}{\rho_0^2 c_a^2}\langle p_1^2\rangle\right] = \frac{1}{2\rho_0}\left[\frac{1}{\omega^2}\langle|\boldsymbol{\nabla}p_1|^2\rangle + \frac{1}{c_a^2}\langle p_1^2\rangle\right], \tag{2.31a}$$

$$= \frac{1}{4\rho_0}\left[\frac{1}{\omega^2}\,|\boldsymbol{\nabla}p_1(\boldsymbol{r})|^2 + \frac{1}{c_a^2}\,|p_1(\boldsymbol{r})|^2\right], \tag{2.31b}$$

where we in the last equality introduce a factor of $\frac{1}{2}$ by use of the relation of the time average of the product of two time-harmonic fields $\langle A(t)B(t)\rangle = \frac{1}{2}\mathrm{Re}\,\{A_0 B_0^*\}$.

2.3 Second-order acoustofluidics

We have now presented the first-order linear acoustofluidic theory. From the linear theory we notice that the harmonic driving $\cos\omega t$ enters all terms, which then averages out over a full oscillation period. The first-order theory therefore leaves no opportunity of achieving a DC drift velocity or an additional DC pressure gradient. However, the second-order perturbation equations in Eqs. (2.7) contain products of two first-order fields leading to terms as $\cos^2\omega t = \frac{1}{2}\cos 2\omega t + \frac{1}{2}$, which has the average of $\frac{1}{2}$ over a full oscillation period.

By time-averaging of the second-order equations Eqs. (2.7) the Navier–Stokes equation can be written as

$$\boldsymbol{\nabla}\langle p_2\rangle = -\langle \boldsymbol{F}\rangle + \eta\Big(\nabla^2\langle \boldsymbol{v}_2\rangle + \beta\boldsymbol{\nabla}\langle\boldsymbol{\nabla}\cdot\boldsymbol{v}_2\rangle\Big), \tag{2.32}$$

where the time-averaged body force density is given by products of first-order fields as

$$\langle \boldsymbol{F}\rangle \equiv \rho_0\big\langle \boldsymbol{v}_1(\boldsymbol{\nabla}\cdot\boldsymbol{v}_1)\big\rangle + \rho_0\big\langle(\boldsymbol{v}_1\cdot\boldsymbol{\nabla})\boldsymbol{v}_1\big\rangle. \tag{2.33}$$

This is the basis for the acoustic pressure force acting on suspended particles in a given medium. The time-averaging of the continuity equation leads to the expression

$$\boldsymbol{\nabla}\cdot\langle \boldsymbol{v}_2\rangle = -\frac{1}{\rho_0}\boldsymbol{\nabla}\cdot\langle\rho_1\boldsymbol{v}_1\rangle, \tag{2.34}$$

which forms the basis for the acoustic streaming induced into a given liquid. Having introduced the two second-order effects, acoustic pressure force and acoustic streaming, we now elaborate more on the pressure force as it plays an important role in parts of the thesis.

2.3.1 The acoustic pressure force

Given the acoustic pressure field p_1 and velocity field $\boldsymbol{v}_1$ it is possible to calculate the acoustic pressure force on a particle with volume V and linear dimension $V^{\frac{1}{3}}$ much smaller than the acoustic wavelength λ. Both for biological cells and for micrometric tracer particles we are in this limit. We now denote the material parameters for the particle with subscripts "p", whereas for the buffer liquid we still use c_a and ρ_0. The speed of sound ratio $\tilde{c}$, the density ratio $\tilde{\rho}$, and the pre-factors f_1 and f_2 are

$$\tilde{c} = \frac{c_\mathrm{p}}{c_a}, \qquad \tilde{\rho} = \frac{\rho_\mathrm{p}}{\rho_0}, \tag{2.35a}$$

$$f_1 = 1 - \frac{1}{\tilde{\rho}\tilde{c}^2}, \qquad f_2 = \frac{2\tilde{\rho}-2}{2\tilde{\rho}+1}. \tag{2.35b}$$

The general expression for the time-averaged acoustic pressure force $\boldsymbol{F}_\mathrm{ac}$ is given by Gorkov [22],

$$\boldsymbol{F}_\mathrm{ac} = -\boldsymbol{\nabla}U_\mathrm{ac}, \tag{2.36a}$$

where the time-averaged acoustic potential is given by

$$U_\mathrm{ac} = -V\left[\frac{f_1}{2\rho_0 c_a^2}\langle p_1^2\rangle - \frac{3f_2\rho_0}{4}\langle|\boldsymbol{v}_1|^2\rangle\right] = -\frac{V}{4\rho_0 c_a^2}\left[2f_1\langle p_1^2\rangle - 3f_2\frac{1}{k^2}\langle|\boldsymbol{\nabla}p_1|^2\rangle\right], \tag{2.36b}$$

where the latter form is obtained by use of Eq. (2.12) and the wave vector $k^2 = k_x^2 + k_y^2 + k_z^2$.

In the case of a single transverse standing pressure wave $p_1 = p_\mathrm{A} \cos(k_y y) \exp(\mathrm{i}\,\omega t)$, it follows from Eq. (2.12) and $\omega = k c_a$ that the time-average of the field squares are related by

$$\langle |\boldsymbol{v}_1|^2 \rangle = \frac{\langle p_1^2 \rangle}{\rho_0 c_a^2}. \tag{2.37}$$

This simplifies Eq. (2.36) to

$$\boldsymbol{F}_\mathrm{ac}(y) = E_\mathrm{ac} k_y V \left[\frac{5\tilde{\rho} - 2}{5\tilde{\rho} + 1} - \frac{1}{\tilde{\rho}\tilde{c}^2} \right] \sin(2k_y y)\, \boldsymbol{e}_y, \tag{2.38}$$

where $\boldsymbol{e}_y$ is the unit vector along the transverse y-direction of the standing ultrasound wave, and where E_ac is the time-averaged acoustic energy density Eq. (2.31) which in this one-dimensional case reduces to

$$E_\mathrm{ac} = \frac{p_\mathrm{A}^2}{4\rho_0 c_a^2}. \tag{2.39}$$

2.4 Multiple-domain systems

The main objective of the thesis is to investigate chip systems, which are multiple-domain systems normally consisting of a silicon chip containing water-filled channels/cavities and bonded with a lid of pyrex glass. The chip in connection with its surroundings, such as holder, piezo-actuator, air, etc., makes up a complex acoustic resonator system. In order to model such systems we need to study matching through the boundary conditions. As we consider acoustic resonances, we omit the notation of the perturbation order of a given field. For material j we denote the zeroth-order density ρ_j, the speed of sound c_j and the first-order pressure field $p_j = p_j(\boldsymbol{r}, t)$.

2.4.1 Acoustic impedances

Besides the acoustic energy, another important acoustic property is the acoustic impedance. The acoustic impedance is especially important when treating transmission and reflection of acoustic waves which occurs in multiple-domain systems, where the acoustic matching of materials plays a major role. For material j we define the characteristic impedance Z_j in terms of density ρ_j and speed of sound c_j as

$$Z_j \equiv \rho_j c_j. \tag{2.40}$$

For more elaborate descriptions of the acoustic impedance, see [5, 44, 46, 47].

2.4.2 Boundary and matching conditions

In the current thesis we employ six types of boundary and matching conditions: (*i*) the continuity condition for pressure and velocity across interior boundaries, (*ii*) the impedance condition, (*iii*) the soft wall condition (zero pressure), (*iv*) the hard wall condition (zero

velocity), (*v*) symmetry condition, and (*vi*) the time-harmonic condition at an oscillating surface. The impedance condition, soft wall condition and hard wall condition are all special cases of the continuity condition. In the following $\boldsymbol{n}$ denotes the local, outward pointing, surface normal vector to the interface under consideration.

Continuity condition

At interfaces between two liquid media we cannot have net forces and regions of no contact. Across an interface this results in continuity of the pressure and continuity in the normal component of the velocity. Expressed in terms of the pressure field, the continuities between the two opposing media a and b read

$$p_a = p_b, \tag{2.41a}$$

$$\frac{1}{\rho_a}\boldsymbol{n}\cdot\boldsymbol{\nabla}p_a = \frac{1}{\rho_b}\boldsymbol{n}\cdot\boldsymbol{\nabla}p_b, \tag{2.41b}$$

where we notice that the pressure field gradients are discontinuous across the interface for $\rho_a \neq \rho_b$.

Impedance condition

We consider a two-domain system consisting of medium a surrounded by medium b. If the surrounding medium b is not infinitely acoustic hard, there will be both transmission and reflection of waves going from medium a to medium b. Assuming that the surrounding medium b (e.g. vacuum or a gas) only carries the transmitted waves from medium a, the pressure waves in our system read

$$p_a(\boldsymbol{r},t) = \left[p_\mathrm{A}\mathrm{e}^{\mathrm{i}\boldsymbol{k}_a\cdot\boldsymbol{r}} + p_\mathrm{B}\mathrm{e}^{-\mathrm{i}\boldsymbol{k}_a\cdot\boldsymbol{r}}\right]\mathrm{e}^{-\mathrm{i}\,\omega t}, \quad \boldsymbol{r}\in\Omega_a, \tag{2.42a}$$

$$p_b(\boldsymbol{r},t) = p_\mathrm{C}\mathrm{e}^{\mathrm{i}\boldsymbol{k}_b\cdot\boldsymbol{r}}\mathrm{e}^{-\mathrm{i}\,\omega t}, \quad \boldsymbol{r}\in\Omega_b, \tag{2.42b}$$

where p_A, p_B and p_C are pressure amplitudes. Utilizing this set of waves the continuity conditions in Eqs. (2.41) can be written into one single condition

$$\frac{1}{\rho_a}\boldsymbol{n}\cdot\boldsymbol{\nabla}p_a = \frac{1}{\rho_b}\boldsymbol{n}\cdot\boldsymbol{k}_b\, p_a, \tag{2.43}$$

which by assuming the boundary to be a plane wall gives the final impedance condition

$$\frac{1}{\rho_a}\boldsymbol{n}\cdot\boldsymbol{\nabla}p_a = \frac{\mathrm{i}\omega}{Z_b}\, p_a, \tag{2.44}$$

where Z_b is the acoustic impedance of the surrounding medium. As mentioned this condition is valid only for harmonic plane waves and thus only for plane boundaries. But nevertheless the condition is used as a simplifying approximation when dealing with solids or liquids bounded by a gas. An investigation for the impedance condition at curved boundaries is seen in Appendix B.

Hard wall condition

If we consider the surrounding medium at an external boundary to be infinitely acoustically hard ($Z_b \to \infty$), ideally it has an infinite acoustic impedance. Making use of the just presented impedance, the so-called hard wall condition appears

$$\boldsymbol{n} \cdot \boldsymbol{\nabla} p_a = 0. \tag{2.45}$$

The hard wall condition is a good approximation in systems where the surrounding medium has a much larger acoustic impedance than that of the subject medium.

Soft wall condition

Oppositely to the hard wall condition, a surrounding medium can be considered to be infinitely soft ($Z_b \to 0$), which is the case of vacuum. If the ratio of the impedance of the subject medium to the impedance of the surrounding medium is close to zero, the impedance boundary condition (2.44) forces the pressure to be close to zero. This gives the so-called soft wall condition

$$p_a = 0. \tag{2.46}$$

Both the hard wall and the soft wall conditions keep the system free of losses at a given boundary, as both conditions do not allow transmissions of waves in or out of the subject medium.

Symmetry condition

If the interface is a symmetry plane, symmetry conditions can be imposed to limit the size of the modeling problem. Depending on the parity, $+1$ (even/symmetric) or -1 (odd/antisymmetric), of the pressure field around e.g. a symmetry line through medium a, the conditions read

$$\boldsymbol{n} \cdot \boldsymbol{\nabla} p_a = 0 \quad \text{(even)}, \tag{2.47a}$$

$$p_a = 0 \quad \text{(odd)}, \tag{2.47b}$$

which is seen to be identical to the hard wall condition and the soft wall condition, respectively.

Time-harmonic acceleration condition

Finally, at a medium/actuator interface we approximate the oscillation of the piezo transducer by a time-harmonic normal acceleration a_n,

$$\frac{1}{\rho_a} \boldsymbol{n} \cdot \boldsymbol{\nabla} p_a = a_n \, e^{-\mathrm{i}\omega t}, \tag{2.48}$$

where we assume that the elastic deformation of the interface is negligible during the actuation and that the transducer delivers a lossless constant acceleration independent of

the load is pushes. This boundary condition is naive, but it will not be considered into greater detail in this thesis work. For more information, see [42].

We here end the description of the simple pressure wave model used throughout the entire thesis. Nevertheless, we describe the elastic wave theory in the next section for use in future work. Hereafter, we present our numerical tool COMSOL MULTIPHYSICS.

2.5 Elastic wave acoustics in solids

During experiments in the group of Laurell, we encountered a discrepancy between the experiments and the above presented simple pressure wave model, where shear waves are neglected. Motivated by this, we in this section briefly describe the theory of elastic waves in solids and we setup the governing equations for elastic waves in isotropic homogeneous solids. Solving these equations is outside the scope of this thesis work, but will be a main topic in continuation of the project. The presented theory is based on Landau and Lifshitz [48].

Linear elastic theory describes how solids deform and build up internal stresses due to loading. The theory relies on deformations being small and that the relationship between stress and strain is linear. The basic entity is the displacement $\boldsymbol{u}(\boldsymbol{r},t)$ of a solid element away from its equilibrium position $\boldsymbol{r}$ to its new temporary position $\hat{\boldsymbol{r}}(\boldsymbol{r},t) = \boldsymbol{r}+\boldsymbol{u}(\boldsymbol{r},t)$. As previously we assume a steady harmonic oscillation of the form $\boldsymbol{u}(\boldsymbol{r},t) = \boldsymbol{u}(\boldsymbol{r})\,\exp(-\mathrm{i}\omega t)$.

In the classical theory of elastic waves, Newton's second law is expressed in terms of force densities. The inertial term is $\rho\partial_t^2\boldsymbol{u} = -\rho\omega^2\boldsymbol{u}$, while the force density is related to the divergence of the stress tensor $\boldsymbol{\sigma}$. For linear elastic theory with small-amplitude oscillations, the Cauchy stress tensor $\sigma_{ik} = \sigma_{ki}$ (ik'th component $\boldsymbol{\sigma}$) is linearly related to the symmetric strain field component $u_{lm} = u_{ml} = \partial_l u_m + \partial_m u_l$ through the rank four elasticity tensor λ_{iklm}. The linear relation is known as Hooke's law

$$\sigma_{ik} = \lambda_{iklm} u_{lm}. \tag{2.49}$$

2.5.1 Isotropic solids

For an isotropic solid the elasticity tensor is fully described by two parameters, Young's modulus E and Poisson's ratio ν, or equivalently by the longitudinal and transverse wave velocities c_L and c_T, respectively,

$$c_\mathrm{L}^2 = \frac{1-\nu}{(1+\nu)(1-2\nu)}\frac{E}{\rho}, \qquad c_\mathrm{T}^2 = \frac{1}{2(1-2\nu)}\frac{E}{\rho}. \tag{2.50}$$

In the isotropic case the Cauchy stress tensor becomes

$$\sigma_{ik} = \left[\partial_i u_k + \partial_k u_i + \frac{\nu}{1-2\nu}(\boldsymbol{\nabla}\cdot\boldsymbol{u})\,\delta_{ik}\right]\frac{E}{1+\nu}. \tag{2.51}$$

The usual equation of motion, where the inertial force density is equated to the divergence of the stress tensor giving

$$\rho\partial_t^2 u_i = \partial_k \sigma_{ik}. \tag{2.52}$$

Table 2.2: Parameters for elastic waves in solids. Listed are the sound velocities for isotropic pyrex glass (borosilicate) and the anisotropic cubic silicon crystal. The elastic coefficients for cubic silicon is found in [49]. Young's modulus and Poisson's ratio is found in [50]. The sound velocities are calculated from these as given in the text. The parameters are given at atmospheric pressure and room temperature.

Speed of sound, pyrex glass	c_{L}	$5603\ \mathrm{m\,s^{-1}}$
	c_{T}	$4852\ \mathrm{m\,s^{-1}}$
	c_{av}	$5155\ \mathrm{m\,s^{-1}}$
Speed of sound, silicon	$c_{\mathrm{L}}^{[100]}$	$8430\ \mathrm{m\,s^{-1}}$
	$c_{\mathrm{T}}^{[100]}$	$5840\ \mathrm{m\,s^{-1}}$
	$c_{\mathrm{L}}^{[110]}$	$9130\ \mathrm{m\,s^{-1}}$
	$c_{\mathrm{T}}^{[110]}$	$5840\ \mathrm{m\,s^{-1}}$
	$c_{\mathrm{T}}^{[110]}$	$4670\ \mathrm{m\,s^{-1}}$
	$c_{\mathrm{L}}^{[111]}$	$9360\ \mathrm{m\,s^{-1}}$
	$c_{\mathrm{T}}^{[111]}$	$5100\ \mathrm{m\,s^{-1}}$
	$c_{\mathrm{av}}^{[100]}$	$6814\ \mathrm{m\,s^{-1}}$
	$c_{\mathrm{av}}^{[110]}$	$6812\ \mathrm{m\,s^{-1}}$
	$c_{\mathrm{av}}^{[111]}$	$6822\ \mathrm{m\,s^{-1}}$
Young's modulus, pyrex glass	E_{py}	63 GPa
Poisson's ratio, pyrex glass	ν_{py}	0.2
Elastic coefficients, silicon	C_{11}	$1.6564 \times 10^{11}\ \mathrm{N\,m^{-2}}$
	C_{12}	$0.6394 \times 10^{11}\ \mathrm{N\,m^{-2}}$
	C_{44}	$0.7951 \times 10^{11}\ \mathrm{N\,m^{-2}}$

The resulting eigenvalue vector equation for the harmonic oscillating eigenmodes becomes

$$\nabla^2 \boldsymbol{u} + \frac{1}{1-2\nu}\boldsymbol{\nabla}(\boldsymbol{\nabla}\cdot\boldsymbol{u}) + \frac{\omega^2}{c_{\mathrm{T}}^2}\boldsymbol{u} = \boldsymbol{0}. \tag{2.53}$$

In an infinite solid it is easy to identify two types of elastic waves. The longitudinal pressure waves appears by taking the divergence of Eq. (2.53), resulting in a displacement formulation of the Helmholtz equation $\nabla^2(\boldsymbol{\nabla}\cdot\boldsymbol{u}) + (\omega^2/c_{\mathrm{L}}^2)(\boldsymbol{\nabla}\cdot\boldsymbol{u}) = 0$. Likewise the transverse shear waves appears by taking the rotation giving the stress formulation of the Helmholtz equation $\nabla^2(\boldsymbol{\nabla}\times\boldsymbol{u}) + (\omega^2/c_{\mathrm{T}}^2)(\boldsymbol{\nabla}\times\boldsymbol{u}) = 0$. We note here how c_{L} and c_{T} becomes the propagation speeds of these two types of waves.

However, in finite solids the elastic waves are reflected at boundaries and generally reflected into both longitudinal and transverse waves. This mixing of longitudinal and transverse waves at boundaries is often expressed through the stress tensor σ_{ik}. If the boundary of the solid is air or vacuum, $\sigma_{ik} = 0$, which implies that the various components components of u_{lm} are coupled, some which are part of $(\boldsymbol{\nabla}\cdot\boldsymbol{u})$ and others which are part of $(\boldsymbol{\nabla}\times\boldsymbol{u})$. This mixing of the purely longitudinal and purely transverse waves complicates the theory of elastic waves in solids.

2.5.2 Sound velocities

As just described we consider both longitudinal and transverse sound velocities when considering elastic waves in solids. Table 2.2 lists the speeds of sound for the primarily considered solids in this thesis, namely pyrex glass and cubic silicon crystal.

The sound velocity for pyrex glass is calculated according to Eqs. (2.50). As the silicon is an anisotropic solid, the sound velocities is based on the elastic coefficients in the corresponding stress tensor. Cubic silicon crystal belongs to the simplest anisotropic group, and it therefore has only three independent elastic coefficients C_{11}, C_{12} and C_{44} [51]. Various combinations [49] of the elastic coeffients and the density gives the sound velocities. The elastic coefficients and the sound velocities for cubic silicon are listed in Table 2.2.

We finally define an average speed of sound for the longitudinal and transverse velocities

$$c_{\mathrm{av}} = \sqrt{c_{\mathrm{L}}^2 + c_{\mathrm{T1}}^2 + c_{\mathrm{T2}}^2}. \tag{2.54}$$

The average values of the sound velocities are given in Table 2.2. From the average speeds of sound, we get a rough estimate of the frequency shift from using the simple pressure model utilizing longitudinal velocities to using the elastic wave theory in solids, where both longitudinal and transverse sound velocities are present. Comparison between the average and longitudinal speed of sound for pyrex glass and the [100] crystal direction in silicon, respectively, gives

$$c_{\mathrm{av}}^{\mathrm{py}} = 0.87\, c_{\mathrm{L}}^{\mathrm{py}}, \quad c_{\mathrm{av}}^{\mathrm{si[100]}} = 0.81\, c_{\mathrm{L}}^{\mathrm{si[100]}}. \tag{2.55}$$

It is seen that the average sound velocity $c_{\mathrm{av}}^{\mathrm{py}}$ for pyrex glass is approximately 13% lower than its longitudinal sound velocity $c_{\mathrm{L}}^{\mathrm{py}}$. For the [100] crystal direction in silicon, this difference is approximately 19%.

Chapter 3

Numerical simulations in Comsol Multiphysics

To solve acoustic problems more complex than the single-domain box presented in Sec. 2.2.2 we employ numerical tools. For this purpose we use the program COMSOL MULTIPHYSICS Version 3.5 (COMSOL), which is a powerful tool for solving partial differential equations (PDEs) using the finite element method (FEM) [52]. The really strong side of COMSOL is its ability to solve coupled multi-physics problems.

COMSOL is equipped with a large number of predefined application modes for various physics problems. The problems are solved using either the graphical user interface (GUI) or by scripting using MATLAB. In both cases the user can modify the governing equations or choose to set up the equations from scratch. In this work the GUI has been used as an initial approach to new problems, while scripting in MATLAB has been the main tool, as it enables the maximum flexibility when it comes to e.g. systematic investigations, postprocessing and utilization of remote high perfomance computing (HPC) facilities.

The governing PDEs and boundary conditions can be represented by three different syntaxes; (*i*) coefficient form, (*ii*) general form, and (*iii*) weak form. We will in this thesis not discuss the advantages of the individual representations, but just turn to the general form which we employ. In the following we describe the general form and show an example of the implementation for solving the Helmholtz equation for a 3D translational invariant silicon/pyrex/water chip geometry, which will be treated in later chapters to investigate the acoustic resonances.

3.1 The general form

The general form for bulk equations in a domain Ω for the m'th variable writes

$$d_{a_m}\frac{\partial u_m}{\partial t} + \boldsymbol{\nabla}\cdot\boldsymbol{\Gamma}_m = f_m, \quad (x,y,z)\in\Omega, \tag{3.1}$$

where u_m is the dependent variable, while d_{a_m}, the flux vector $\boldsymbol{\Gamma}_m$ and source field f_m are coefficients specified by the user, that can be functions of spatial coordinates, dependent variables and time.

The bulk equations are solved subject to the boundary conditions at boundary $\partial\Omega$, which on general form are written as

$$R_m = 0, \qquad (x, y, z) \in \partial\Omega, \tag{3.2a}$$

$$-\boldsymbol{n} \cdot \boldsymbol{\Gamma}_m = G_m + \mu_k \frac{\partial R_k}{\partial u_m}, \quad (x, y, z) \in \partial\Omega, \tag{3.2b}$$

where $\boldsymbol{n}$ is the normal vector pointing outward from the boundary $\partial\Omega$, u_m is the dependent variable and μ_k is a Lagrange multiplier for the n'th boundary element. R_m and G_m are specified by the user. Eq. (3.2a) is a Dirichlet boundary condition and Eq. (3.2b) is a Neumann boundary condition. If $\partial R_k/\partial u_m \neq 0$, Comsol makes sure that Eq. (3.2b) is satisfied by internally adjusting the Lagrange multiplier μ_k. We notice that $\boldsymbol{\Gamma}_m$ is present in both the bulk equations and boundary equations, and it is therefore the users task to choose the variables such that the equations and boundary conditions are mutually fulfilled.

3.1.1 The 3D Helmholtz wave equation on general form

To illustrate the implementation of the general form, we state the implementation of the 3D Helmholtz equation for the acoustic pressure p as given in Eq. (2.17). For a single-domain system with only one flux vector $\boldsymbol{\Gamma}$ and one source field f we write

$$\boldsymbol{\Gamma} \equiv \begin{bmatrix} \partial_x p \\ \partial_y p \\ \partial_z p \end{bmatrix}, \quad f \equiv -k_0^2 p, \tag{3.3}$$

which is seen to make up the Helmholtz equation when substituted into Eq. (3.1).

3.2 Structure of 3D translational invariant acoustics problem

In the following we describe a Comsol/Matlab -script implemented and used in the thesis work to solve eigensolutions for the Helmholtz equation for a multi-domain 3D translational invariant chip geometry as described in Fig. 5.8 in Sec. 5.3. The geometry is a y-symmetric (y, z) cross-section of a silicon chip with an etched water-filled channel and bonded with a pyrex glass lid. We use the material parameters as given in Table 2.1. The full script is seen in Appendix D.

We start by clearing the workspace.

```
2 clear all, flclear fem, close all
```

We then define our material and geometric parameters for later use, which we load into the `fem`-struct.

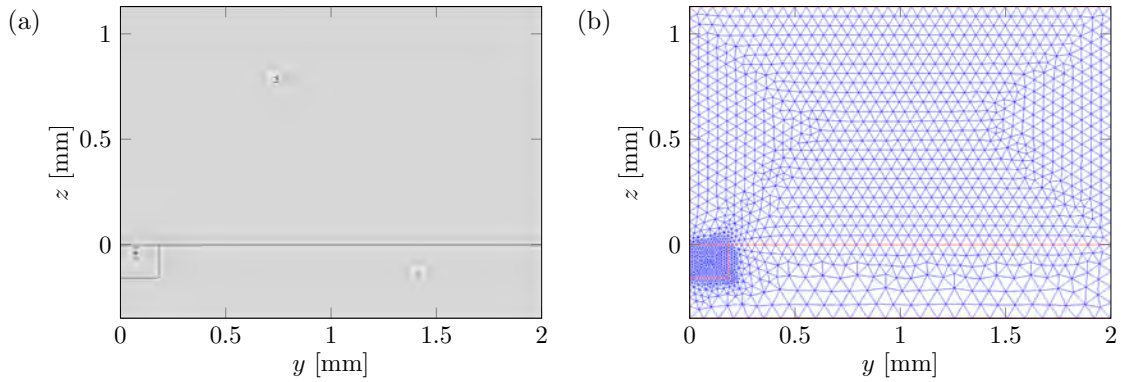

Figure 3.1: (a) Representation of the geometry investigated in the COMSOL example. The geometry is a y-symmetric (y, z) cross-section of a silicon chip with an etched water-filled channel and bonded with a lid of pyrex glass. The origin $(0, 0)$ of the system is placed in the center along y at the interface between the pyrex lid and the water-filled channel. Each material constitutes a domain group. The figure shows the numbering of the boundaries. (b) Illustration of the mesh grid stemming from requiring the presence of 50 mesh elements per wavelength (in this case at a frequency of 2 MHz). Notice that the acoustic wavelength is shortest (many elements) in the water-filled channel and longest (few elements) in the silicon chip.

```
% Constants into fem-struct
fem.const = struct('cWa',cWa,'cSi',cSi,'cPy',cPy,...
    'rhoWa',rhoWa,'rhoSi',rhoSi,'rhoPy',rhoPy,'kx',kx);
```

Here $k_x = \pi/L$ is the wave number for a standing half-wavelength mode along the translational invariant x-direction with L being the chip length. We hereafter draw the geometry consisting of three rectangles; `g1` (pyrex lid), `g2` (water-filled channel), and `g3` (silicon chip). The origin $(0, 0)$ of the system is placed in the center along y at the interface between the pyrex lid and the water-filled channel, see Fig. 3.1 (a).

```
% Geometry
g1 = rect2(W/2,hPy,'base','corner','pos',[0 0]);
g2 = rect2(w/2,hWa,'base','corner','pos',[0 -hWa]);
g3 = rect2(W/2,hSi,'base','corner','pos',[0 -hSi]);
s.objs={g1,g2,g3};
fem.draw=struct('s',s);
fem.geom=geomcsg(fem);
```

Having drawn the geometry we allocate the domains (`fem.equ.ind`) and boundaries (`fem.bnd.ind`) into domain groups and boundary groups, respectively. The domains and boundaries are automatically numbered by COMSOL. We have a domain group for each material; the water, the silicon and the pyrex. For the boundaries, we have four boundary groups, namely one for the continuity condition Eqs. (2.41), one for the soft wall condition Eqs. (2.46), one for the hard wall condition Eqs. (2.45) and one for the y-symmetric condition Eqs. (2.47).

```
fem.equ.ind = {2 1 3};
fem.bnd.ind = {[4 8 6 9] [7 10 11] [1 3 5] [2]};
```

We choose our (y, z)-coordinate system (`fem.sdim`), our dependent variable to be the pressure p (`fem.dim`) and our shape functions to be second-order Lagrange elements (`fem.shape`).

```
% Variables
fem.sdim = {'y','z'};
fem.dim = {'p'};
fem.shape = 2;
```

We choose the representation of the equations to general form (`fem.form`). We use `fem.equ.expr` to define different material parameters (speed of sound and density) for the three domain groups. We define p in all the domain groups (`fem.equ.shape`) and choose the flux vector $\mathbf{\Gamma}$ by `fem.equ.ga` and the source field f by `fem.equ.f`. Due to the definition of `rho` and `c`, the three domain groups have the same $\mathbf{\Gamma}$ and f. We then initialize $p = 0$ by the command `fem.equ.init`.

```
% Governing equations on general form
fem.form = 'general';
fem.equ.expr = {'c',{'cWa','cSi','cPy'},'rho',{'rhoWa','rhoSi','
    rhoPy'}};
fem.equ.shape = {1 1 1};     % Defining p in all domain groups
fem.equ.ga = {{{'py/rho';'pz/rho'}}};
fem.equ.f = {{'-(omega^2/c^2-kx^2)*p/rho'}};
fem.equ.init = {{'0'}};      % p is initially set to 0 everywhere
```

Notice the apparent unnecessary presence of the density `rho` in the Helmholtz equation defined in `fem.equ.ga` and `fem.equ.f`. The presence of the density `rho` is implemented in order to fulfill certain boundary conditions.

The command `fem.bnd.shape` defines p in all the four boundary groups. The boundary conditions for each boundary group are defined by R (`fem.bnd.r`) and g (`fem.bnd.g`) in Eq. (3.2). Boundary group 1 states the continuity condition between the interface between two domains, and R and g are put to zero, such that Comsol fulfills the condition $-\boldsymbol{n} \cdot (\mathbf{\Gamma}_i - \mathbf{\Gamma}_j) = G + \mu(\partial R/\partial p)$ for two opposing domains i an j. Boundary group 2 gives the soft boundary condition by setting $R = 0 \equiv 0 - p$ and boundary group 4 gives the hard boundary condition by setting R and g to zero. Boundary group 3 sets the even (hard) y-symmetric condition or odd (soft) y-symmetric condition.

```
% Boundary conditions on general form
fem.bnd.shape = {1,1,1,1};  % Defining p on all boundaries
fem.bnd.r = {...
    {'0'}, ...       % BC group [1] Interface, continuity
    {'0-p'}, ...     % BC group [2] Air-interface, soft
    {'0-1*p'}, ...   % BC group [3] y-symm.: -1*p (even), 0*p (odd)
    {'0'}};          % BC group [4] Piezo, hard wall
fem.bnd.g = { ...
```

```
70      {'0'}, ...          % BC group [1] Interface, continuity
71      {'0'}, ...          % BC group [2] Air-interface, soft
72      {'0'}, ...          % BC group [3] y-symm.
73      {'0'}};             % BC group [4] Piezo, hard wall
```

The mesh grid is created by the mesh initialization routine `meshinit`. We set a maximum element size for each domain by the `'hmaxsub'`-parameter. The maximum elements sizes `mWa`, `mSi` and `mPy` we define such that we have approximately 50 mesh elements per wavelength. According to COMSOL we must use at least 6 elements per wavelength in order to resolve the acoustic wave dynamics properly. The mesh is extended onto the finite element problem by use of the `meshextend` command.

```
79  fem.mesh = meshinit(fem,'hmaxsub',[2 1 3; mWa mSi mPy]);
80  fem.xmesh = meshextend(fem);
```

Finally the problem is fully defined and ready to be solved. This is done by the eigenvalue solver `femeig`. The properties `'solcomp'` and `'outcomp'` determine which equation component to solve for and which solutions to store. The property `'eigname'` defines our eigenvalue to be solved for, the property `'shift'` sets the value of the eigenvalue in which vicinity the eigensolutions are searched, the property `'neigs'` gives the number of wanted eigensolutions, the property `'linsolver'` chooses the numerical solver and the property `'etol'` sets the eigenvalue tolerance. It is important to remark that solving an eigenvalue problem does not give a meaningful amplitude of the eigenfunction.

```
85  % Solving EVP
86  fem.sol=femeig(fem, ...
87      'solcomp',{'p'}, ...
88      'outcomp',{'p'}, ...
89      'eigname','omega',...
90      'shift',2*pi*0,...
91      'neigs',1, ...
92      'linsolver','spooles',...
93      'etol',1e-8);
```

Besides `femeig` COMSOL has a collection of other solvers. In the current thesis we make use of `femeig` and the stationary solver `femstatic`. By `femstatic` we time-harmonically solve the system for a defined actuation frequency imposed by a time-harmonically vibrating boundary condition with a certain amplitude as defined in Eq. (2.48).

After solving the implemented problem we can use various commands to postprocess the solutions. In this example we use the `postplot`-command to visualize the pressure field, which in Fig. 3.2 (a) is plotted as a color plot.

3.2.1 Validation of analytical solution

In order to benchmark the presented code, we validate our results against the analytical solution for acoustic eigenmodes in the single-domain box presented in Sec. 2.2.2. In the code, we set the all the material parameters to that of water, namely `rhoPy=rhoWa, rhoSi=rhoWa` and `cPy=cWa, cSi=cWa`, while we leave the remaining code unchanged. The

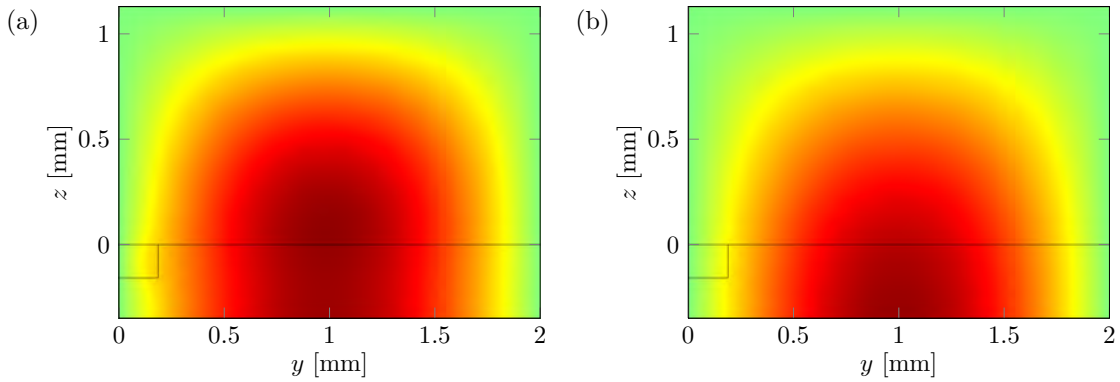

Figure 3.2: Color plot (red is positive, green is neutral) of the eigensolutions for the pressure field p. (a) Pressure eigenmode for the three domains being different materials, namely water, silicon and pyrex glass. The eigenfrequency is $f = 1.9088$ MHz. (b) Pressure eigenmode for all domains being water. The eigenfrequency is $f = 0.4478$ MHz and validates well with the analytic prediction.

expected outcome is the $(n_x, n_y, n_z) = (1, 2, 1/2)$ mode as we search for the eigenmode with the lowest frequency. The eigenmode calculated by the Comsol code is illustrated as a color plot in Fig. 3.2 (b) with a frequency $f_{\text{Comsol}} = 0.4478$ MHz. The analytically calculated frequency from Eq. (2.18) becomes

$$f_{\text{box}} = \frac{c_{\text{wa}}}{2}\sqrt{\frac{n_x^2}{L^2} + \frac{n_y^2}{W^2} + \frac{n_z^2}{(h_{\text{si}} + h_{\text{py}})^2}} = 0.4478 \text{ MHz}, \tag{3.4}$$

for which the Comsol calculated frequency f_{Comsol} approximates up till the tenth digit with the employed mesh fineness. The implemented numerical code is thus validated and ready for use in the resonance analyses in the thesis.

With the numerical tools set we are now ready to study the acoustofluidic equations in time-harmonically actuated systems.

Chapter 4

Actuation of acoustic resonances

Applying ultrasound to an experimental microfluidic setup requires the use of a piezo transducer, a piezo-electric crystal, driven at MHz frequency by an AC voltage. The piezo transducer ideally vibrates with a time-harmonic acceleration, which leads to a time-harmonic varying pressure field in the resonator.

In this chapter we study time-harmonic acoustic actuated resonator systems, which allows for the existence of acoustic energy losses due to viscous attenuation and impedance radiation transmission of waves to the surroundings. We consider an analytical solvable example of a 1D single-domain double-actuated liquid slab. From this analytical model, we can check the validation of the perturbation approach by determining the implicit perturbation parameter, and we can estimate the shape of the acoustic energy density in frequency space. With the analytical example in mind, we numerically investigate a 3D pseudo-realistic model system involving the fundamental physics involved in an experimental setup.

4.1 1D double-actuated liquid slab

We analyze the analytical solvable problem of a 1D double-actuated liquid slab as shown in Fig. 4.1. The liquid slab of length $2L$ is placed between two parallel, harmonically oscillating, planar walls. The walls vibrate in anti-phase around equilibrium positions of $x = \pm L$ with a maximum oscillation amplitude ℓ. The amplitude ℓ is assumed to be small relative to the size of the slab $\ell \ll L$. The velocity v_{wall} of the walls read

$$v_{\text{wall}}(\pm L, t) = \partial_x \phi_{\text{wall}}(\pm L, t) = \pm \omega \ell \mathrm{e}^{-\mathrm{i}\omega t}, \tag{4.1}$$

where the wall velocity v_{wall} is expressed in terms of the velocity potential ϕ_{wall} by use of Eq. (2.11a). As the system is time-harmonically actuated, the first-order velocity potential $\phi_1(x,t)$ fulfills the (lossy) Helmholtz equation as described in Eq. (2.27). The problem is easily solved [5] and the first order pressure field $p_1(x,t)$ in the liquid slab becomes

$$p_1(x,t) = -\mathrm{i}\rho_0 c_a^2 k \ell \, \frac{\cos(kx)}{\sin(kL)} \, \mathrm{e}^{\mathrm{i}\omega t}, \tag{4.2}$$

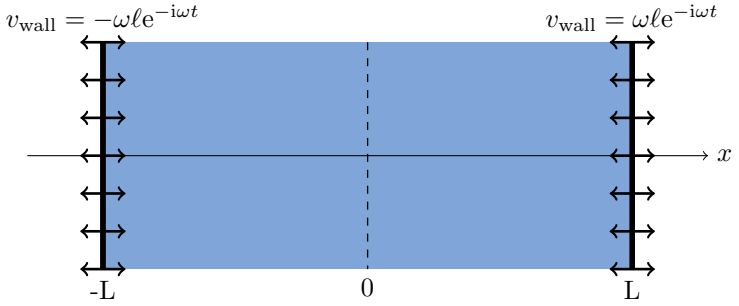

Figure 4.1: Sketch of the 1D single-domain resonator of a liquid slab (blue) between two parallel, harmonically oscillating, planar walls at $x = \pm L$. The walls are vibrating with maximum amplitude ℓ in anti-phase with the velocity $v_{\text{wall}}(\pm L, t) = \pm\omega\ell e^{-i\omega t}$.

where $k = k_0(1 + i\gamma)$ is the complex wavenumber. As discussed in Chap. 2 this definition of k assumes the viscosity to be small. Expanding $p_1(x, t)$ to first order in k around k_0 and making use of $\gamma k_0 L \ll 1$ yields

$$p_1(x,t) \approx -i\rho_0\omega c_a \ell \frac{\cos(k_0 x) - i\gamma k_0 x \sin(k_0 x)}{\sin(k_0 L) + i\gamma k_0 L \cos(k_0 L)} e^{-i\omega t}. \tag{4.3}$$

As the acoustic resonances acquires large pressure amplitudes, the resonances are identified by the minimum in the denominator in Eq. (4.3), i.e. for $k_0 L = n\pi$ for $n = 1, 2, 3, \ldots$ giving

$$k_0 = k_n = n\frac{\pi}{L}, \quad n = 1, 2, 3, \ldots, \tag{4.4a}$$

$$\omega_0 = \omega_n = n\frac{\pi c_a}{L}, \quad n = 1, 2, 3, \ldots, \tag{4.4b}$$

which gives the resonance frequency $f_n = (c_a n)/2L$, which we recognize as the 1D case $f_{1,0,0}$ of the eigenfrequency for the single-domain box in Eq. (2.18). In the inviscid case $\gamma \to 0$ the pressure goes to infinity on resonance.

4.1.1 Perturbation parameter and first-order pressure field

We assume that the walls are *Ferroperm* Pz26 piezo-electric transducers, the displacement amplitude is estimated to $\ell \approx 1$ nm. The value is the estimated static displacement utilizing *Ferroperm*'s online piezo electric calculator [53] for a freely vibrating actuator of size $50 \times 12 \times 1$ mm applied a static voltage of 2 V. Moreover, we consider the vibrational frequency in the low MHz range and the liquid to be water.

Off-resonance we have $\sin(k_0 L) = 1$ and by use of $\gamma \ll 1$ we get the magnitude of the first-order pressure field off-resonance

$$|p_1| = \rho_0\omega c_a \ell \approx 1.5 \text{ kPa}. \tag{4.5}$$

We then find the corresponding first-order density field $|\rho_1| = \frac{1}{c_a^2}|p_1| = \frac{\omega\ell}{c_a}\rho_0$, from which we directly read off the implicit perturbation parameter off-resonance as

$$\alpha_{\text{per}}^{\text{off}} = \frac{\omega\ell}{c_a} \approx 6.7 \times 10^{-7}, \tag{4.6}$$

which gives that the perturbation approach is valid as $\alpha_{\text{per}}^{\text{off}} \ll 1$. On-resonance $\sin(k_0 L) = 0$ and by insertion of the resonance condition Eq. (4.4b) into Eq. (4.3), we get the pressure amplitude

$$|p_1| = \frac{1}{n\pi\gamma}\rho_0\omega c_a\ell \approx 5 \times 10^7 \text{ Pa}, \tag{4.7}$$

where the numerical estimate is for $n = 1$. The only change from the off-resonance magnitude is the multiplication of $1/(n\pi\gamma)$, and the implicit perturbation parameter on-resonance becomes

$$\alpha_{\text{per}}^{\text{on}} = \frac{1}{n\pi\gamma}\frac{\omega\ell}{c_a} \approx 2.2 \times 10^{-2}, \tag{4.8}$$

The on-resonance calculations are close to invalidate the perturbation approach. Nevertheless the estimate of the displacement amplitude is considered to be an upper limit, as it might not reach the static displacement through a MHz oscillation and due to fact that the calculation is based on the piezo transducer being unloaded. We therefore in this naive boundary model assume that the piezo transducer is lossless and perfectly coupled. Secondly, an experimental system includes impedance loss from transmission of waves, which increases the effective damping coefficient γ, leading to a lower estimated pressure amplitude.

4.1.2 The energy of an acoustic resonator

With the objective of calculating the time-averaged acoustic energy density, the square of the absolute pressure field and its corresponding derivative become

$$|p_1(x)|^2 \approx (\rho_0\omega c_a\ell)^2 \frac{\cos^2(k_0 x) + \gamma^2 k_0^2 x^2 \sin^2(k_0 x)}{\sin^2(k_0 L) + \gamma^2 k_0^2 L^2 \cos^2(k_0 L)}, \tag{4.9}$$

$$|\partial_x p_1(x)|^2 \approx (\rho_0\omega^2\ell)^2 \frac{\sin^2(k_0 x) + \gamma^2 k_0^2 x^2 \cos^2(k_0 x)}{\sin^2(k_0 L) + \gamma^2 k_0^2 L^2 \cos^2(k_0 L)}. \tag{4.10}$$

Using the definition of the acoustic energy density in Eq. (2.31), we calculate the spatially averaged acoustic energy density $\mathcal{E}_{\text{ac}}$ over the length of the liquid slab

$$\mathcal{E}_{\text{ac}}(\omega) = \frac{1}{2L}\int_{x=-L}^{L} \frac{1}{4\rho_0}\left[\frac{1}{\omega^2}|\partial_x p_1(x)|^2 + \frac{1}{c_a^2}|p_1(x)|^2\right]\mathrm{d}x, \tag{4.11}$$

which by insertion of the pressure field and its derivative followed by integration gives

$$\mathcal{E}_{\text{ac}}(f) = \frac{\rho_0\omega^2\ell^2}{8L}\frac{L + \frac{1}{3}\gamma^2 k_0^2 L^3}{\sin^2(k_0 L) + \gamma^2 k_0^2 L^2 \cos^2(k_0 L)}. \tag{4.12}$$

We now drive the resonator close to the resonance frequency ω_0, namely $\omega = \omega_0 + \delta\omega$, where $\delta\omega$ is a small perturbation such that $\delta\omega \ll \omega_0$. Further rewriting utilizing $\gamma \ll 1$ yields

$$\mathcal{E}_{\mathrm{ac}}(\omega) = \frac{\mathcal{E}_0}{\left[\frac{2Q}{f_0}(f - f_0)\right]^2 + 1}, \tag{4.13}$$

which shows that the acoustic energy density with these assumptions are described by a Lorentzian line-shape fit, which we know from the description of the classical harmonic oscillator. The energy density is centered around the resonance frequency f_0 with maximum amplitude of the energy density $\mathcal{E}_0 = \mathcal{E}_{\mathrm{ac}}(f_0) = \rho_0 c_a^2 \ell^2/(8L^2\gamma^2)$. The full width at half maximum (FWHM) Δf_0 is defined by $\mathcal{E}_{\mathrm{ac}}(f_0 \pm \Delta f_0) = \mathcal{E}_0/2$ and the corresponding Q-value is defined as $Q = f_0/\Delta f_0 = 1/(2\gamma)$.

The numerical value of the maximum amplitude is estimated to $\mathcal{E}_0 \approx 2.7 \times 10^3$ J m^{-3}, which is approximately a factor of fifty larger than observed experimentally in the current thesis work, see Chap. 8. Again we explain the discrepancy by the naive lossless and perfectly coupled transducer model and the low value of the damping coefficient γ, which does not take into account the impedance losses. Calculating the Q-value for this model system we get $Q = 1/(2\gamma) = 5 \times 10^4$.

Having investigated a simple analytical actuation model we are now ready to numerically analyze a more realistic model system.

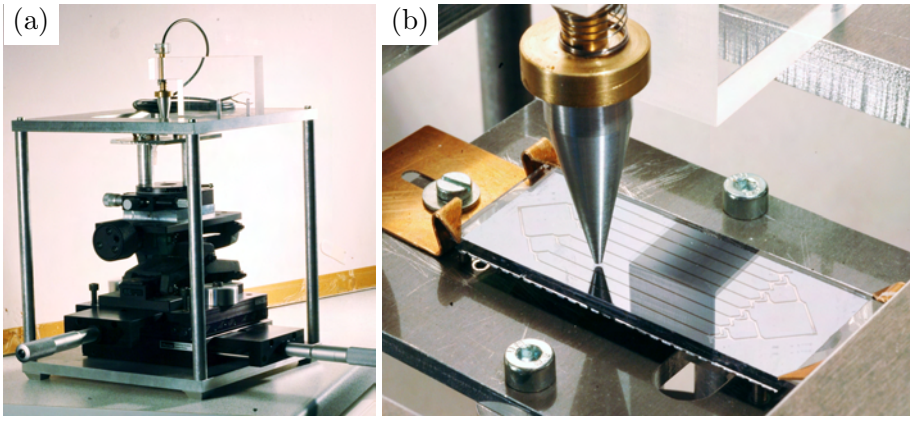

Figure 4.2: Point-actuation device fabricated in the group of Laurell as a result of the analyses in this thesis work. The setup limits the influence from acoustic transmission loss and it limits the transducer area, which is hard to theoretically model properly. The point-actuation device will play an important role in future quantitative comparison between experimental and theoretical models. (a) Full image of the point-actuation device having a spatially-movable chip stage. The chip is acoustically actuated from above by the fixed aluminum horn. (b) Zoom-in of the actuated chip being clamped by four brass pins on top and bottom. The aluminum horn is actuated by an internal air-backed piezo transducer of the type PZ26 from *Ferroperm Piezoceramics A/S*.

4.2 Point-actuation model

In this section we investigate a point-actuated model system. In future experimental work, the point-actuated system is an ideal setup for minimizing influences from transmission loss of wave energy to the surroundings and to minimize the area of the piezo transducer for which proper modeling is cumbersome. This is verified in Chap. 8, where we experimentally investigate the behavior of a piezo transducer.

Compared to a plate transducer, the point transducer delivers much lower power as it has lower area, and the point transducer is thus meant as a nice tool for investigations, but not for practical applications. We believe that a experimental point-actuation device will be of major importance in future work for quantitative studies of resonance spectra in acoustofluidic chips. Based on our analyses, such a device has been fabricated in the group of Laurell, see Fig. 4.2. As a preliminary treatment for future direct-experimentally comparable models, we set up model system.

4.2.1 Model system

The model system must on one hand be simple to allow for a thorough analysis, but on the other hand contain the following four physical aspects: (*i*) a water-filled microchamber inside a silicon chip, (*ii*) a small piezo transducer inducing the ultrasound field inside the system, (*iii*) acoustic radiation to the surrounding air, and (*iv*) a number of small metal pins supporting the silicon chip while ensuring a minimal acoustic coupling to the surroundings.

These prerequisites lead to a rectangular silicon chip of length L, width W, and height H, containing a rectangular water-filled chamber of length l, width w, and height h, as shown in Fig. 4.3. A piezo transducer of circular cross-section and of radius R is acoustically coupled to the chip, and for support, the chip is clamped between four metal pins on top and bottom.

4.2.2 Results

The simulations of the actuated model system are done utilizing Comsol described in Chap. 3. We use scripting and use a maximization algorithm to locate the acoustic resonance frequencies. The time-harmonic solutions are solved by the built-in Comsol-solver `femstatic`. To avoid mesh dependence, the same mesh is applied to all analyses, see Fig. 4.4 (a). To be able to work with a single fixed mesh for varying positions of the actuator and supporting pins, we have defined 23 circular areas on both the top and the bottom surface of the silicon chip. The single actuator and the eight pins can then be put on any of these 46 positions without loss of numerical accuracy. Finally, to ensure sufficient spatial resolution perpendicular to the top and bottom surface, we have inserted narrow slabs with fine meshing at these surfaces. The script is presented in Appendix E.

The analysis is initialized by approximating the locations of the acoustic resonances by an eigenfrequency analysis of the model system being completely inviscid and surrounded by vacuum, i.e using soft-wall boundary conditions. The acoustic resonance

$f_{1,1,1} = 761$ kHz in the water-filled chamber is shown in Fig. 4.4 (b). Note that the acoustic energy completely confines in the water-filled microchamber. We set up the conditions for such confined modes in Chap. 7 on acoustic waveguides.

Viscous damping, impedance radiation and resonance shape

Among the 46 possible circular areas, the actuator is placed at that particular one, which gives the largest resonance energy E_{tot}. Note, that in this example we treat the total acoustic energy in the system, meaning that the energy amplitude is only for internal comparison in the current model example. The amplitude scales with the applied normal acceleration a_n in Eq. (2.48) at the transducer boundary. In this model example $a_n = 1\ \text{m}\,\text{s}^{-2}$, corresponding to a transducer amplitude of approximately $l \approx 40$ fm at a frequency of $f_{1,1,1} = 761$ kHz.

First, we study the lowest resonance mode for an unsupported chip surrounded by air. We vary the viscous damping coefficient γ from 10^{-6} to 10^{-3} as shown in Fig. 4.5 (a). As expected, due to weak damping in the harmonically driven system, the resonance peak $E_{\text{tot}}(f)$ is well approximated by a Lorentzian line shape as given in Eq. (4.13). The resonance frequency f_0 and maximum energy amplitude are found from the maximization algorithm and the Q-values are obtained by fitting the numerical data points to the Lorentzian line shape. We note that the Q-values are large, up to $Q \approx 10^4$. The resonance peaks are very sharp with a width of $\Delta f_0 \approx 10^2$ Hz for $f_0 \approx 10^6$ Hz.

The amplitude and the Q-value of the acoustic resonance decrease significantly as the viscous damping coefficient γ increases from slightly below the value for water ($\gamma \approx 10^{-6}$ corresponds to acetone or heated water) to 1000 times this value ($\gamma \approx 10^{-3}$ corresponds to glycerol). For $\gamma > 10^{-3}$ the damping is so high that the acoustic energy in the water-filled microchamber is negligible, and the acoustic resonance disappears completely.

To study the influence of the surrounding air for the unsupported chip we change the

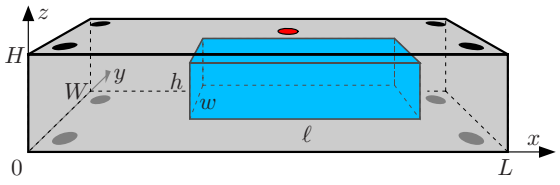

Chip length	L	10.5	mm
Chip width	W	3.2	mm
Chip height	H	1.0	mm
Cavity length	l	4.7	mm
Cavity width	w	1.4	mm
Cavity height	h	0.3	mm
Radius, actuator and pins	R	0.3	mm

Figure 4.3: Sketch of the model system and the geometrical parameters. The used material parameters are given in Table 2.1. Inside the rectangular silicon chip (light gray) of length L, width W, and height H, is placed a rectangular water-filled chamber (blue) of length l, width w, and height h. The lower left corner of the chip is at $(0, 0, 0)$ mm and the lower left corner of the chamber is at $(1.30, 0.68, 0.30)$ mm. The chip is supported by being clamped between four circular metal pins on the top (black disks) and on the bottom (gray disks), just modeled by the silicon/pin interface of circular shape. The acoustic actuation is provided by a cylindrical piezo-element, here modeled by the silicon/actuator interface of circular shape (red disk) shown on the top of the silicon chip. All disks have the radius R.

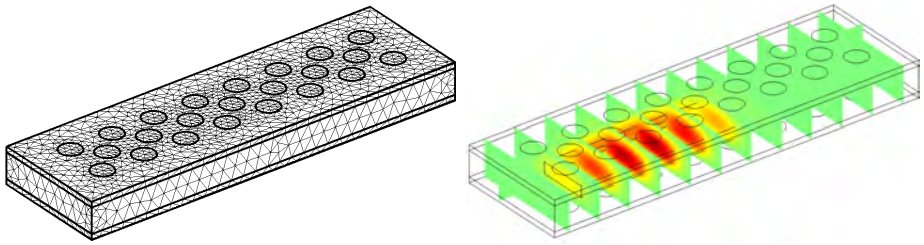

Figure 4.4: (a) The fixed mesh contains 21340 elements, which for the solution at any given frequency yields 33605 degrees of freedom. On the top surface is seen the 23 pre-defined actuator/pin positions. The two slabs with refined mesh ensures a good resolution near the actuator/pin positions. The water-filled microchamber inside the silicon chip is not visible. (b) The pressu´re eigenmode has frequency $f_{1,1,1} = 761$ kHz for the system in vacuum, i.e., $p = 0$ at the chip surface.

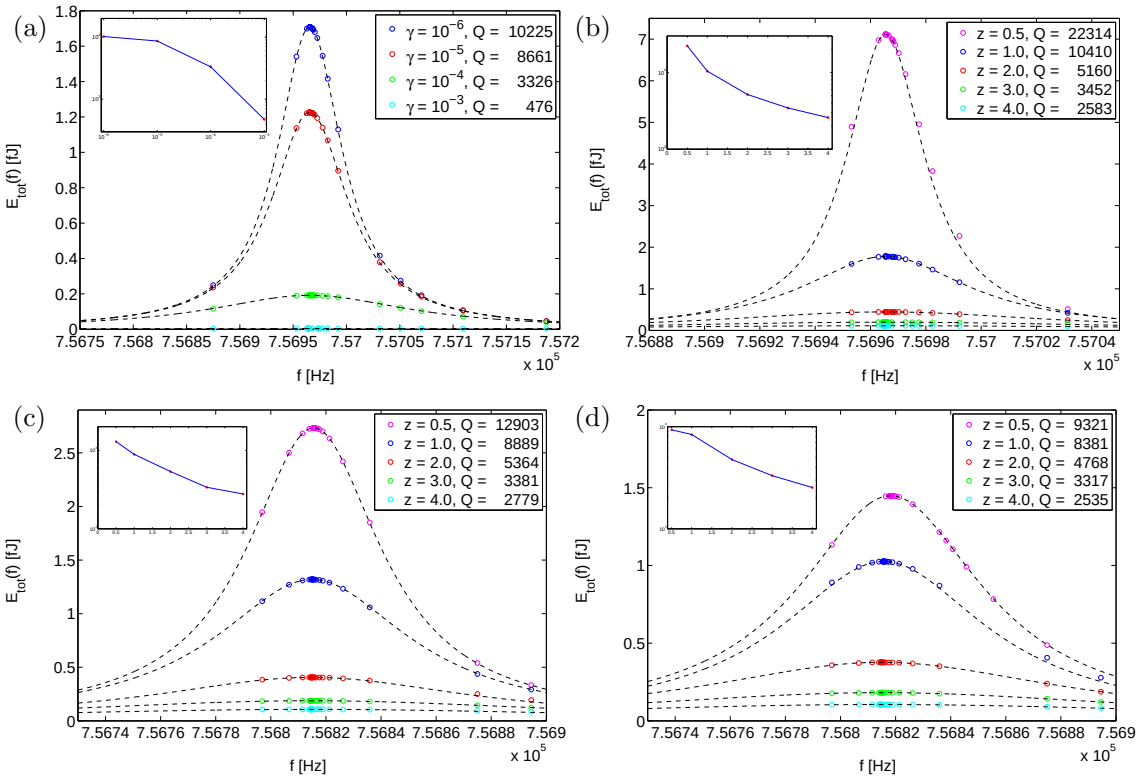

Figure 4.5: The acoustic energy $E_{\rm tot}$ as a function of frequency f for various values of (a) viscous damping coefficient γ without pins for support, (b) normalized impedance $z = Z/Z_{\rm air}$ without pins for support, (c) normalized impedance $z = Z/Z_{\rm air}$ with iron pins for support and (d) normalized impedance $z = Z/Z_{\rm air}$ with silicon pins for support. The numerical data points are clustered around the resonance frequency as a consequence of the method employed to locate the resonance peak. The dashed lines are fits to Lorentzian line shapes. The insets shows Q as a function of (a) γ and (b,c,d) z.

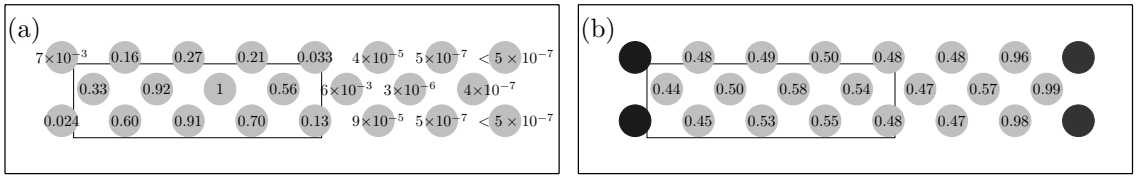

Figure 4.6: (a) The normalized acoustic energy $E_{\text{tot}}(f_0)/E_{\text{max}}$ for the lowest resonance mode in an unsupported rectangular silicon chip (thick black line) for 23 different positions (gray disks) of the circular actuator on the bottom surface. The energies are normalized by the maximum value $E_{\text{max}} = 1.78$ fJ, which is the resonance energy obtained for the actuator positioned at the disk with the value 1. The position of the water-filled microchamber is indicated by the rectangle (thin black line). The resonance energy decreases rapidly as a function of increasing distance between the actuator and the water-filled chamber. (b) The same for a supported chip, where the position of the four silicon support pins are marked by black disks. The numbers are the ratios between the resonance energy for the cases with and without supporting pins.

impedance Z from $0.5Z_{\text{air}}$ to $4Z_{\text{air}}$ corresponding to changes in air pressure from 0.5 bar to 4 bar or gas densities from 0.25 kg m^{-3} to 16 kg m^{-3} at 1 bar. The results for behavior of the resonance peak is similar to the previous sweep in γ, as seen in Fig. 4.5 (b), and the amplitude and Q-value decrease for increasing impedance.

The next step is to include the supporting pins and the associated energy loss through their impedance. We place the pins at the four corner positions at the top and at the bottom surface (the black/gray disks in Fig. 4.6). In Fig. 4.5 (c) we show the resonance peak of the chip supported by iron pins in analogy to the one shown in Fig. 4.5 (b) for an unsupported chip. The iron pins are modeled by changing the impedance boundary condition from $Z = Z_{\text{air}}$ to $Z = Z_{\text{iron}}$. All other other parameters remain unchanged. The main observation is that the resonance amplitude is decreased. This is expected, since the impedance mismatch at the eight pin positions has been decreased from $Z_{\text{air}}/Z_{\text{si}}$ to $Z_{\text{iron}}/Z_{\text{si}}$ thus making a larger energy out-flux possible. This trend continues in the case of silicon pins, which of course are ideally matched acoustically to the silicon chip. In Fig. 4.5 (d), where the eight iron pins have been replaced by eight silicon pins, the resonance energies decrease even further.

Resonance energy and actuator position

Finally, we show the results of changing the position of the actuator on the surface. For simplicity, we begin by considering the unsupported chip. We have calculated the resonance amplitudes for all 46 possible actuator positions. The maximum amplitude $E_{\text{max}} = 1.78$ fJ was found on the bottom surface, where the water-filled chamber is closest to the surface. All 46 resonance amplitudes $E_{\text{tot}}(f_0)$ was normalized by E_{max}, and the resulting values $E_{\text{tot}}(f_0)/E_{\text{max}}$ are shown in Fig. 4.6 (a); each value is placed at the corresponding position on the surface. The resulting values clearly show how the resonance amplitude rapidly decreases as the distance between the microchamber and the actuator increases.

The same calculation was then repeated in the case of supporting silicon pins, the case

of largest loss due to impedance matching between pins and chip. Fig. 4.6 (b) shows the relative decrease in resonance amplitude for each individual actuator position comparing the case with and without support. In most cases the relative energy loss is around 50 % with minor variations.

4.2.3 Concluding remarks

We have established a model, which includes the most significant physical aspects of acoustically driven microfluidic systems near resonance. It acts as a preliminary treatment for future work concerning the quantitative comparison of acoustic frequency spectrum in acoustofluidic chip systems investigated by the point-actuation device shown in Fig. 4.2.

We have shown the presence of the expected decrease of the resonance amplitude as a function of increased viscous damping in the water-filled microchamber and of decreased acoustical impedance mismatch with the surroundings. In particular, we have shown that the position of the actuator has a significant influence of the amplitude of the acoustic resonance. In our simple system we have observed a relative change in resonance amplitudes of about 10^3 by moving the actuator a distance of twice the diameter of the actuator, and about 10^6 for distances of four times the diameter. Moreover, the analysis clearly shows the dominance of the systems eigenresonance as the type of the eigenmode is independent of the position of the actuator.

Chapter 5

Analysis of transverse half-wavelength resonances

In the current chapter we investigate the usual transverse half-wavelength picture by 1D and 2D models. Moreover, we present numerical 3D models for future analysis. The major part of the work is summarized in a peer-reviewed conference proceeding published for the 157th meeting of the Acoustical Society of America, Portland, Oregon, May 2009. The paper is included in Appendix A.

5.1 Analysis of 1D models

For experimental applications it is desirable to work with half-wavelength waves of odd symmetry in the transverse y-direction of the water-filled channel, i.e. $w = \lambda/2$ and thus a resonance frequency $f_{0,1,0} \approx c_{\mathrm{wa}}/(2w)$. A perfect transverse half-wavelength pressure eigenmode is seen in Fig. 2.1 (d), where the surrounding silicon is assumed to be infinitely hard. This is not entirely correct and the question now arises how the width W of a

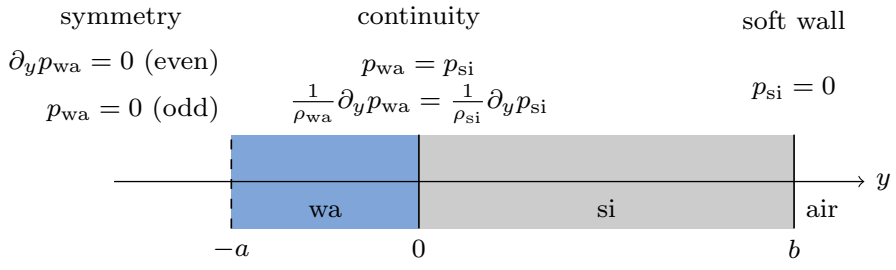

Figure 5.1: Sketch of the 1D model containing half the water-filled channel (wa) and the silicon chip (si). The model includes three boundaries; a symmetric point in the center of the channel ($y = -a$), an interface between channel and chip ($y = 0$), and the outer boundary of the silicon chip ($y = b$). Notice that the boundary condition at the symmetry point gives either even or odd pressure-modes across the channel.

surrounding silicon chip affects this simple estimate for $f_{0,1,0}$.

In Fig. 5.1 is sketched a 1D model for the transverse y-direction, where for simplicity we introduce the lengths $a \equiv w/2$ and $b \equiv (W - w)/2$ for half the width of the channel and the width of the silicon chip from the channel to the edge, respectively. The model is symmetric around the center of the channel, thus leading to two classes of solutions for the pressure, namely even and odd modes.

Using the proper symmetry boundary condition Eq. (2.47) at $y = -a$ and the soft boundary condition Eq. (2.46) at $y = b$, results in cosine (even) or sine (odd) solutions for the pressure waves,

$$p_{\mathrm{wa}}(y) = A_{\mathrm{wa}} \cos\left[k_{\mathrm{wa}}(y + a)\right] \quad \text{(even)}, \tag{5.1a}$$

$$p_{\mathrm{wa}}(y) = A_{\mathrm{wa}} \sin\left[k_{\mathrm{wa}}(y + a)\right] \quad \text{(odd)}, \tag{5.1b}$$

$$p_{\mathrm{si}}(y) = A_{\mathrm{si}} \sin\left[k_{\mathrm{si}}(b - y)\right], \tag{5.1c}$$

where A_{wa} and A_{si} are pressure amplitudes. Employing the interface conditions Eq. (2.41) at $y = 0$ and utilizing that $k_{\mathrm{si}} = k_{\mathrm{wa}} c_{\mathrm{wa}}/c_{\mathrm{si}}$, results in transcendental equations for even and odd pressure eigenmodes

$$\cot(\theta) = z \tan(\alpha\theta) \qquad \text{(even)}, \tag{5.2a}$$

$$\cot(\theta) = -\frac{1}{z} \cot(\alpha\theta) \quad \text{(odd)}, \tag{5.2b}$$

where $\theta \equiv k_{\mathrm{wa}} a$ is the dimensionless wavenumber, $z = Z_{\mathrm{si}}/Z_{\mathrm{wa}} \approx 13.4$ is the acoustic impedance ratio, and α is the aspect ratio parameter given by

$$\alpha \equiv \frac{c_{\mathrm{wa}}}{c_{\mathrm{si}}} \frac{b}{a} = \frac{\text{number of wavelengths in the silicon chip}}{\text{number of wavelengths in the water-filled channel}}. \tag{5.3}$$

From Eq. (5.2) it is now possible for a given α to determine which value of θ that most accurately approximates a perfect $\lambda/2$-mode of wavelength $\lambda^*_{\mathrm{wa}} = 4a$ in the water-filled channel. Expressing the actual wavelength λ_{wa} as a function of the ideal wavelength λ^*_{wa} and a relative shift δ in the wavelength, we get

$$\lambda_{\mathrm{wa}} = \lambda^*_{\mathrm{wa}}(1 + \delta), \tag{5.4}$$

$$\theta = \frac{\pi}{2}(1 + \delta)^{-1}, \tag{5.5}$$

where $\theta = \pi/2$ for $\delta = 0$ thus corresponds to a perfect half-wavelength mode inside the water-filled channel.

5.1.1 Qualitative analysis

Without detailed calculations we can for a fixed value of a immediately give the solutions of this two-domain problem in the extreme limits $b \ll a$, an infinitely thin shell of silicon, and $b \gg a$, an infinitely wide shell of silicon.

For $b \ll a$ the lowest modes are M1 (even, $a = \lambda_{\mathrm{wa}}/4$), M2 (odd, $a = 2\lambda_{\mathrm{wa}}/4$), M3 (even, $a = 3\lambda_{\mathrm{wa}}/4$), M4 (odd, $a = 4\lambda_{\mathrm{wa}}/4$), M5 (odd, $a = 5\lambda_{\mathrm{wa}}/4$), etc. all being

approximately zero at the water/silicon interface. The resonance frequency $f_{0,n,0}$ for mode n is thus $f_{0,n,0} \approx n\, c_{\mathrm{wa}}/(4a)$, for $\alpha \to 0$. Modes for $b \ll a$ are illustrated in the left column of Fig. 5.2.

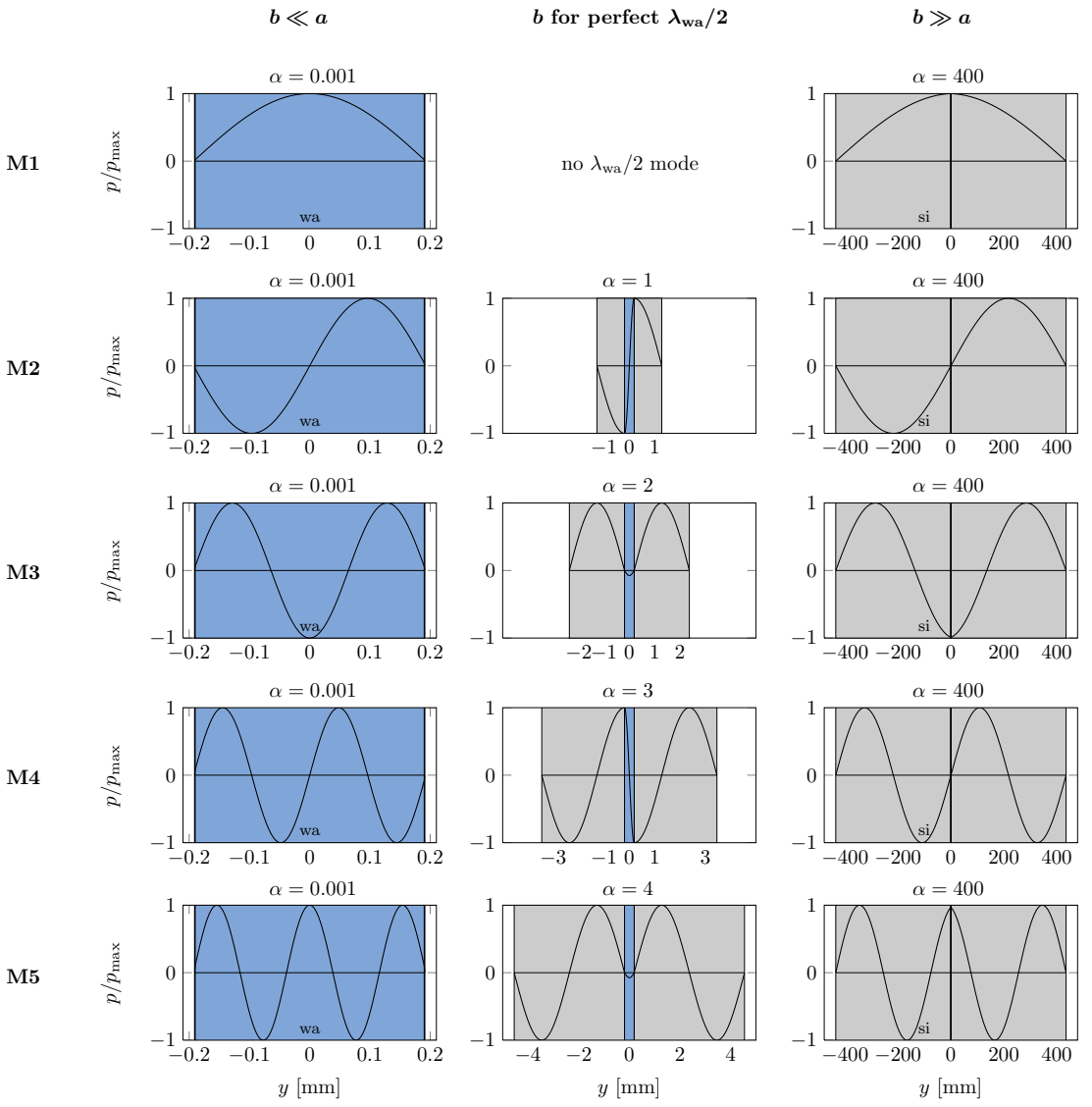

Figure 5.2: Five lowest pressure eigenmodes M1-M5 for varying width $W = w(1 + \frac{c_{\mathrm{si}}}{c_{\mathrm{wa}}}\alpha)$ of the silicon chip and fixed water-filled channel of width $w = 2a = 0.38$ mm. *Left column* shows the pressure modes in the extreme limit $b \ll a$ corresponding to an infinitely thin shell of silicon. In this finite valued case $\alpha = 1/1000$, thus making $b \approx a \times 10^{-3}$. *Right column* shows the pressure modes in the extreme limit $b \gg a$ corresponding to an infinitely wide shell of silicon. Here $\alpha = 400$, thus making $b \approx a \times 10^{3}$. *Center column* shows the pressure modes for the optimal b/a aspect ratio to give perfect half-wavelength modes in the water-filled channel. Every second $\lambda_{\mathrm{wa}}/2$-mode is odd and even, respectively.

For $b \gg a$, i.e. when b is stretched towards infinity, these modes deform continuously into M1 (even, $b = \lambda_{si}/4$), M2 (odd, $b = 2\lambda_{si}/4$), M3 (even, $b = 3\lambda_{si}/4$), M4 (odd, $b = 4\lambda_{si}/4$), M5 (odd, $b = 5\lambda_{si}/4$), all being zero at the outer edge of the silicon. The resonance frequency $f_{0,n,0}$ for mode n is thus $f_{0,n,0} \approx n\, c_{si}/(4b)$, for $\alpha \to \infty$, which clearly decreases towards zero as b increases. Modes for $b \gg a$ are seen in the right column of Fig. 5.2.

Consequently, for any given mode there exists exactly one value of b for which the desired perfect half-wavelength resonance mode with frequency $f = c_{wa}/(4a)$ is obtained. However, since the ideal resonance is an odd mode with exactly one half wavelength inside the water-filled channel, there exists only such a mode in every second case. This is illustrated in the center column of Fig. 5.2.

Fig. 5.3 (a) plots the lowest seven eigenfrequencies as a function of the aspect ratio parameter α. We clearly see that the eigenfrequencies decrease for increasing values of α, and we notice how each mode has the desired value of $f_{0,1,0} \approx 2$ MHz for exactly one value of α. Fig. 5.3 (b) shows the corresponding deviations δ in wavelength from the perfect half-wavelength $\lambda_{wa}/2 = 2a$.

5.1.2 Quantitative analysis

Bearing in mind the qualitative expectations, we quantitatively solve the problem. Inserting $\theta = \pi/2$ into Eq. (5.2) to find solutions for $\delta = 0$, requires α to be an odd positive integer for odd pressure modes, while α is required to be an even positive integer for even pressure modes. These solutions are illustrated in Fig. 5.4, where the components of the transcendental equations are plotted. It is observed in Fig. 5.4 (a) that for $\alpha = 1$, an odd $\lambda/2$-mode is perfectly matching the channel width with $\delta = 0$, while even $\lambda/2$-modes have $\delta \neq 0$. For $\alpha = 2$ as seen in Fig. 5.4 (b), the opposite is the case. From Fig. 5.4 it is also deducted that the largest deviations in δ occurs for the above discussed values of α. This is also observed in the δ versus frequency plot in Fig. 5.3 (b). To sum up, the limits of getting either well-defined or ill-defined modes, forces the aspect ratio b/a to be

$$\delta = 0: \quad \frac{b}{a} = \frac{c_{si}}{c_{wa}}\alpha, \qquad \alpha = 1,3,5\ldots \quad \text{odd}, \qquad \alpha = 2,4,6\ldots \quad \text{even}, \tag{5.6a}$$

$$\delta \text{ large}: \quad \frac{b}{a} = \frac{c_{si}}{c_{wa}}\alpha, \qquad \alpha = 1,3,5\ldots \quad \text{even}, \qquad \alpha = 2,4,6\ldots \quad \text{odd}. \tag{5.6b}$$

In Fig. 5.5 the relative change δ as function of α is plotted as in Fig. 5.3 (b). But only odd half-wavelength modes are plotted and only the mode having the smallest $|\delta|$ for a given α. Thus this graph acts as an design graph in order to optimize the half-wavelength modes. As already discussed the size of the relative change $|\delta|$ periodically has regions with large and small values as a function of α. As α increases, the maximum values of $|\delta|$ decreases. It is seen that well-defined odd modes with $|\delta| \leq 0.1$ exist for aspect ratios as low as $\alpha = 1$ and thus $b/a = c_{si}/c_{wa} \approx 5.7$. The value of the relative change for odd modes

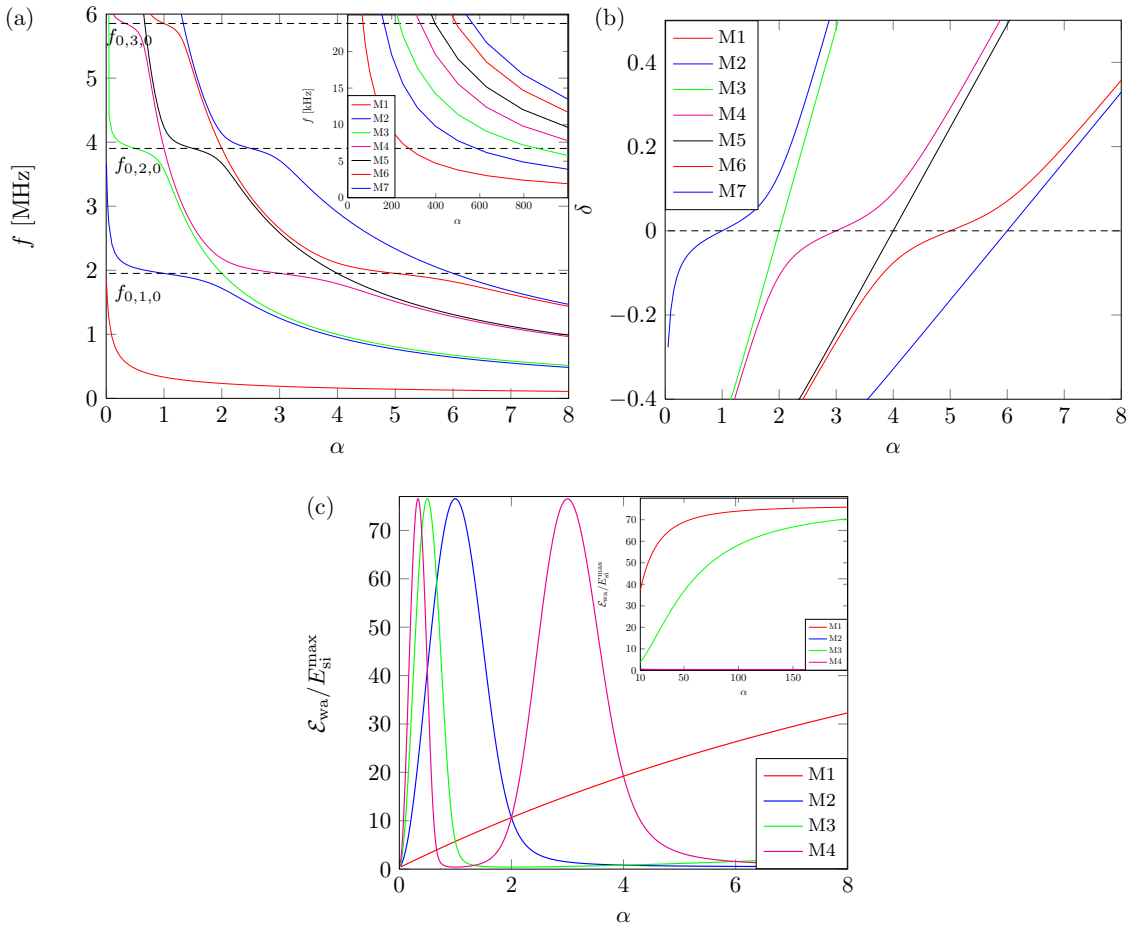

Figure 5.3: 1D COMSOL simulations of the seven lowest eigenmodes, M1-M7. (a) Frequencies as a function of the aspect ratio parameter α. Indicated are $f_{0,1,0}$, $f_{0,2,0}$ and $f_{0,3,0}$. The inset shows f for $100 < \alpha < 1000$. (b) Relative change in wavelength δ from the perfect half-wavelength in the water-filled channel $\lambda^* = 4a$ as a function of aspect ratio parameter α. (c) Ratio $\mathcal{E}_{\mathrm{wa}}/E_{\mathrm{si}}^{\mathrm{max}}$ of the average acoustic energy density $\mathcal{E}_{\mathrm{wa}}$ in water to the maximum acoustic energy density $E_{\mathrm{si}}^{\mathrm{max}}$ in silicon as a function of aspect ratio parameter α. Four clarity, only the four lowest modes M1-M4 are plotted. The inset shows $\mathcal{E}_{\mathrm{wa}}/E_{\mathrm{si}}^{\mathrm{max}}$ for $10 < \alpha < 200$.

approaches $-1/2$ for $\alpha \to 0$, which corresponds to a full-wavelength sine-mode within the channel. $b/a = c_{\mathrm{si}}/c_{\mathrm{wa}}$ is thus a lower limit for the aspect ratio when considering odd half-wavelength modes.

We observe the fact that δ is numerically largest when it is positive, which thus corresponds to a wavelength longer than the channel width. For fixed aspect ratios, modes with frequencies higher than $f_{0,1,0}$ are therefore leading to lower δ than those modes having frequencies lower than $f_{0,1,0}$.

Fig. 5.5 (a) shows marks for the four modes shown in Fig. 5.6. Modes A and B are perfectly matching half-wavelength modes with $\delta = 0$ and show up for the frequency

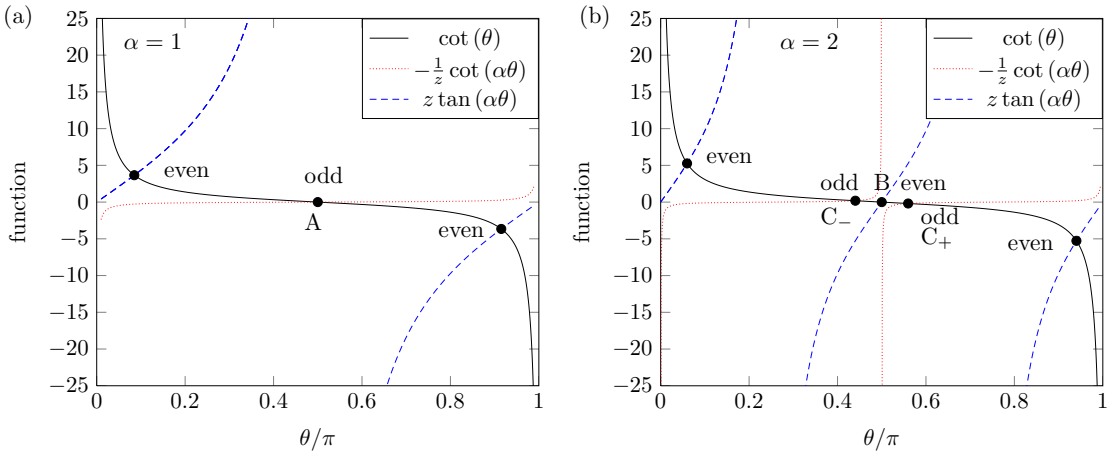

Figure 5.4: Plot of the components in the governing transcendental equation Eq. (5.2) for two values of α. Solutions to the transcendental equation Eq. (5.2a) are marked by filled circles and labeled "even", while solutions to Eq. (5.2b) are marked "odd". (a) $\alpha = 1$ leading to perfectly matching odd mode at $\theta = \pi/2$. (b) $\alpha = 2$ leading to perfectly matching even mode at $\theta = \pi/2$.

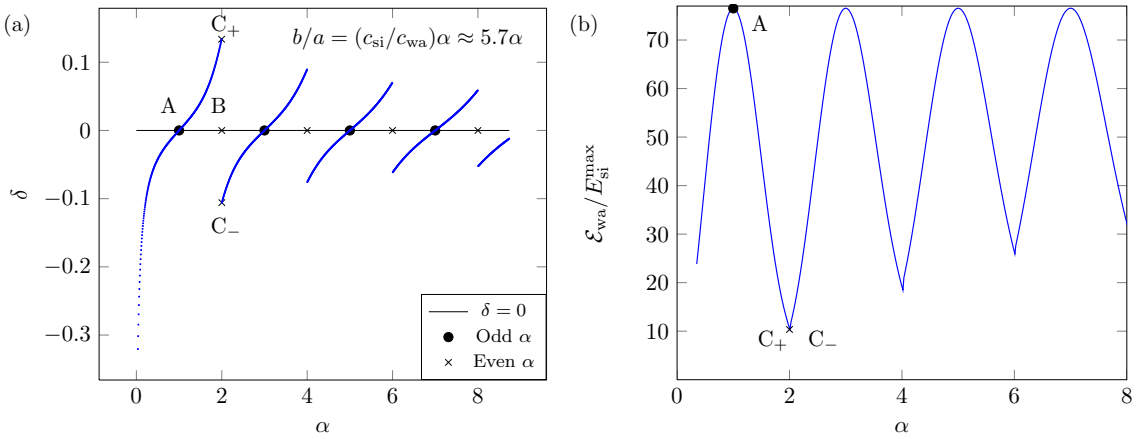

Figure 5.5: Design graphs plotting *only for the modes best approximating perfect odd half-wavelength mode* in the water-filled channel. These plots are ideal for using as design tool if one wants to create an odd standing half-wavelength transverse mode across the channel. (a) Minimum relative change δ found by numerical solutions to Eq. (5.2) as a function of α. Each (α, δ) stems from the mode having the smallest value of δ for that α. Indicated are the even (black crosses) and odd (black dots) integer values of α. The labels A, B, C_+ and C_- link to the corresponding modes shown in Fig. 5.6. The labels illustrate that e.g. a perfect even mode at point B is surrounded by two non-perfect odd modes at point C_+ and C_-. (b) Average acoustic energy density in water to the maximum acoustic energy density in silicon $\mathcal{E}_{wa}/E_{si}^{max}$ as a function of α. Notice in this 1D approximation how the perfectly matching odd half-wavelength mode A has high $\mathcal{E}_{wa}/E_{si}^{max}$, whereas the corresponding ill-matching modes C_+ and C_- has low $\mathcal{E}_{wa}/E_{si}^{max}$.

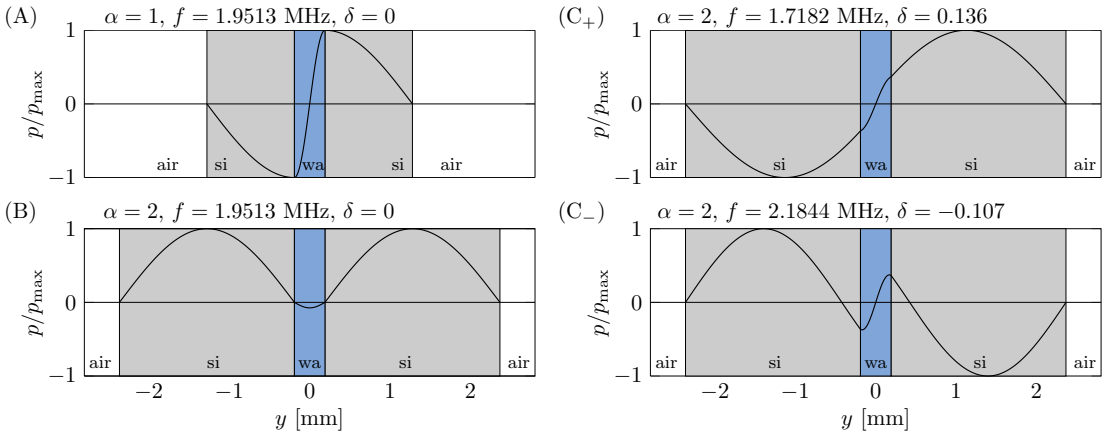

Figure 5.6: Pressure eigenmodes $p(y)$ of the four special cases marked in Figs. 5.4 and 5.5 for the 1D silicon/water (gray/blue) model given a water-filled channel of width $w = 2a = 0.38$ mm. (A) The perfectly matched silicon chip with $\alpha = 1$ ($W = 2.6$ mm) supporting the anti-symmetric half-wavelength pressure mode in the water-filled channel at frequency $f = 1.9513$ MHz. (B) The silicon chip with $\alpha = 2$ ($W = 4.7$ mm) also supports a perfect half-wavelength pressure mode at frequency $f = 1.9513$ MHz, however this mode is symmetric. (C_+) An anti-symmetric eigenmode in the chip with $\alpha = 2$ with a frequency as close as possible, but lower, to the ideal frequency of subfigure (A). Here $f = 1.7182$ MHz and the wavelength in the water-filled channel is 13.6 % too long ($\delta = 0.136$). (C_-) An anti-symmetric eigenmode in the chip with $\alpha = 2$ with a frequency as close as possible, but higher, to the ideal frequency of subfigure (A). Here $f = 2.1844$ MHz and the wavelength in the water-filled channel is 10.7 % too short ($\delta = -0.107$).

$f_{0,1,0} = 1.9513$ MHz. Mode A is odd and exists for $\alpha = 1$, while mode B is even and exists for $\alpha = 2$. For $\alpha = 2$, we get no perfect odd modes, but two odd modes, C_+ and C_-, surrounding mode B. Mode C_+ has $f = 1.7182$ MHz and $\delta = 10.6\%$, while mode C_- has $f = 2.1844$ MHz and $\delta = -10.7\%$. These numerical values and corresponding acoustic energy densities are presented in Table 5.1. For the mode C_- we have $\lambda_{wa} < w/2$, and we observe that the pressure antinodes are positioned a little distance from the channel walls. This may result in bad sorting for devices like that depicted in Fig. 1.1, since particles attracted towards pressure nodes, will be pushed towards the walls if they get to close.

Moreover, we notice that mode A corresponds to mode M2, where the width b of the silicon layer has been chosen to give the perfect odd half-wavelength mode in the water-filled channel. Mode C_+ is mode M2 after stretching b with a factor of 2. The mode is antisymmetric and is not perfect since λ_{wa} is too long. Mode B is the even mode M3 for the same geometry as mode C_+. The wavelength matches perfect, but it is symmetric. Finally, mode C_- is an antisymmetric mode M4, which has too short a wavelength λ_{wa}.

5.1.3 Energy densities

A quantitative measure of the quality of a given eigenmode can be obtained from the expression for the acoustic energy density E_{ac} in Eq. (2.31). The higher the average acoustic energy density $\mathcal{E}_{wa}$ is in the water-filled channel relative to the maximum acoustic

Table 5.1: Values of 1D COMSOL simulations of $\lambda_{\mathrm{wa}}/2$-modes. y-symm. denotes the symmetry.

Mode	α	y-symm.	f [MHz]	δ [%]	$\mathcal{E}_{\mathrm{wa}}/E_{\mathrm{si}}^{\mathrm{max}}$
A	1	odd	1.9513	0	76.5
B	2	even	1.9513	0	0.4
C_+	2	odd	1.7182	13.6	10.7
C_-	2	odd	2.1844	-10.7	10.7

energy density $E_{\mathrm{si}}^{\mathrm{max}}$ in the surrounding silicon chip, the better. This ratio is a direct measure of the amount of useful acoustic energy in the water-filled channel to the amount of useless acoustic energy in the silicon chip. The acoustic energy density is relevant, since it is directly proportional to the acoustic pressure force on suspended particles, see Eq. (2.38)

For the four specific modes A, B, C_+, and C_- shown in Fig. 5.6 we find numerically that $\mathcal{E}_{\mathrm{wa}}/E_{\mathrm{si}}^{\mathrm{max}} = 76.5$, 0.4, 10.6, and 10.6, respectively. Clearly, the perfect anti-symmetric half-wavelength mode in the $\alpha = 1$ chip has the best figure of merit. The perfectly matching mode A gives a larger channel-pressure to chip-pressure, which thus leads to the largest maximum acoustic energy density, see Table 5.1. Better match therefore leads to higher relative energy densities in the channel. The difference from the perfect odd mode A to the least perfect odd modes C_+ and C_- shows to be a factor of seven in this simple 1D approximation. This thus underestimates the importance of correct matching of wavelengths in separation chip designs as this corresponds to the need of a separation channel seven times longer if designed with $\alpha = 2$ instead of $\alpha = 1$.

To get the full overview of the distribution of the 1D energy densities, these are plotted in Fig. 5.3 (c) for the modes M1-M4 as a function of α. It is seen that the energy density ratio varies strongly as a function of the aspect ratio parameter α for the different modes. We clearly see that mode M2 has maximum energy density in the water-filled channel as $\alpha = 1$, where it is a perfect half-wavelength mode with $\delta = 0$, see Fig. 5.3 (b). Observing mode M4 we see that $\mathcal{E}_{\mathrm{wa}}/E_{\mathrm{si}}^{\mathrm{max}}$ has two maxima for the interval $0 < \alpha < 8$; one for $\alpha = 0.2$ being a perfect three-half-wavelength mode in the channel and one for $\alpha = 3$ being a perfect half-wavelength mode in the channel.

Fig. 5.5 (b) plots the energy density ratio $\mathcal{E}_{\mathrm{wa}}/E_{\mathrm{si}}^{\mathrm{max}}$ versus α only for the modes being the best approximating odd half-wavelength modes in the channel. We thus get an overview of which values of α that gives high energy density ratio in the case of designing the widespread acoustic separator utilizing odd half-wavelength modes. For odd α the $\lambda_{\mathrm{wa}}/2$ mode has maximum energy density ratio, while for even α the $\lambda_{\mathrm{wa}}/2$ mode has minimum energy density ratio. Note as α in general increases, the minimum of energy density ratio increases too.

The just presented 1D models acts as a preliminary treatment of the usual transverse half-wavelength picture. They show that 1D wave solutions only exist for propagation in both the water-filled channel and the surrounding silicon chip. For these types of wave solutions the need for geometrically matching was illuminated based on a quantitative measure of the acoustic energy density and the relative deviation from a perfect transverse

half-wavelength mode.

5.2 Analysis of 2D models

We now extend our analysis of the half-wavelength modes from 1D to 2D by extending the analysis with the length direction of the system along the x-axis. As shown in Fig. 5.7, the most prominent change from 1D to 2D is the appearance of oscillations in the axial x-direction, a feature not possible in 1D.

The introduction of axial modes leads to the possibility of having special modes falling off exponentially in the surrounding silicon chip. These modes confine in the water-filled channel and will be treated in Chap. 7. In this section we restrict ourselves to consider resonance modes living in both the water-filled channel and the surrounding silicon chip.

If we consider a translational invariant system along the x-axis, the channel length l equals the chip length L. The pressure wave solutions are then easily obtained by the 1D solutions in Eq. (5.1) multiplied by a standing wave solution $\cos(k_x x)$ with $n_x = 2L/\lambda_x$ number of half-wavelengths. In the following we consider a system having $L > l$, which is solved using 2D Comsol simulations. The Comsol-script is seen in Appendix C. The model is implemented as shown in Chap. 3 with continuity conditions between the two domains and soft wall condition at the edge of the chip.

To enable direct comparison we reuse the 1D widths in 2D for the transverse y-direction. Some of the resulting pressure eigenmodes are shown in Fig. 5.7. We note how the modes (A), (B), (C_+), and (C_-) from the 1D case in Fig. 5.6 also can be identified in the 2D case of Fig. 5.7. However, due to the extra degree of freedom for oscillations in the axial x-direction, it is now possible even in the "bad" $\alpha = 2$ chip to find eigenmodes (D_+ and D_-), which are both close to the ideal frequency $f = 1.95$ MHz of the $\alpha = 1$ chip in panel (A) and at the same time possess the wanted odd (one-node) symmetry in the transverse y-direction. The only drawback is the appearance of several nodes in the axial direction. It is found experimentally that pressure modes with a lower number of axial nodes lead to higher separation efficiencies [38].

As in the 1D case, we can study the quality of the 2D pressure eigenmodes by evaluating the ratio of the acoustic energy density in the water channel relative to that in the

Table 5.2: Data for the six 2D pressure eigenmodes shown in Fig. 5.7. Listed are the value of the aspect parameter α and the symmetries, as well as the resulting frequency f, relative shift in wavelength δ, and energy density ratio obtained by Comsol simulations.

Mode	α	x-symm.	y-symm.	f [MHz]	δ [%]	$\mathcal{E}_{\mathrm{wa}}/E_{\mathrm{si}}^{\max}$
A	1	even	odd	1.9518	0.0	39.2
B	2	even	even	1.9560	1.2	0.2
C_+	2	even	odd	1.7209	13.4	6.3
C_-	2	even	odd	2.1870	−11.7	5.1
D_+	2	even	odd	1.9430	1.4	32.0
D_-	2	odd	odd	1.9616	0.5	36.1

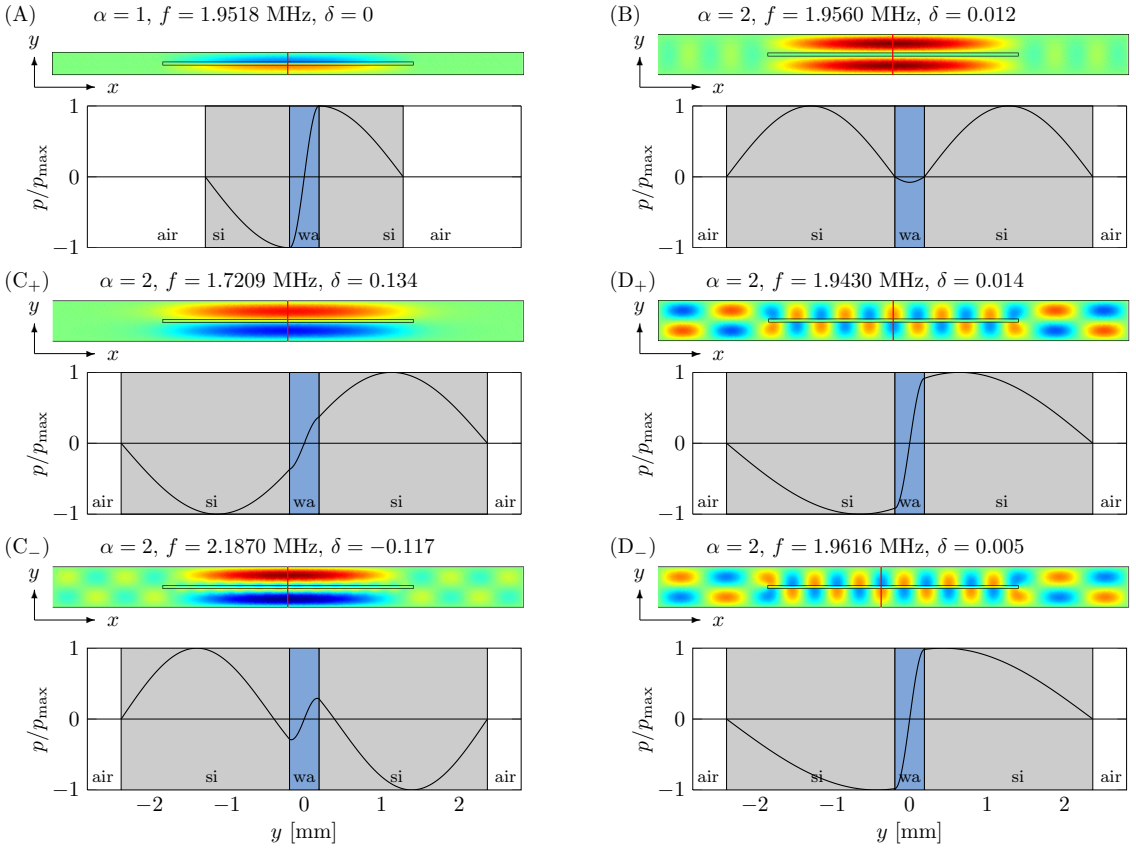

Figure 5.7: 2D COMSOL simulations of six pressure eigenmodes in a water-filled channel (wa/blue) of width $w = 0.38$ mm and length $l = 29.30$ mm. The channel is placed in a silicon chip (si/gray) of width $W = w[1 + \alpha\,(c_{\rm si}/c_{\rm wa})]$ and length $L = 55.00$ mm. The widths here are as in the 1D system of Fig. 5.6. For each mode the pressure amplitude is plotted along the indicated red line in the corresponding 2D color plot of the pressure amplitude. (A) $\alpha = 1$, $W = 2.6$ mm: perfectly matching mode at the ideal frequency $f = 1.95$ MHz having odd (one-node) transverse symmetry and even (zero-node) axial symmetry. (B) $\alpha = 2$, $W = 4.7$ mm: matching mode at $f = 1.95$ MHz very near the ideal frequency, but having the un-wanted even (two-node) transverse symmetry and even (zero-node) axial symmetry. (C$_+$) and (C$_-$) $\alpha = 2$, $W = 4.7$ mm: as in Fig. 5.6 non-matching modes with frequencies far below/above the ideal frequency having the wanted odd (one-node) transverse symmetry and even (zero-node) axial symmetry. (D$_+$) and (D$_-$) $\alpha = 2$, $W = 4.7$ mm: almost matching modes with frequencies near the ideal frequency having the wanted odd (one-node) transverse symmetry, but with many nodes in the axial direction.

silicon chip. The results are listed in Table 5.2. Again, the perfectly matched A-mode has the best figure of merit, however it is seen that also the new D$_+$ and D$_-$ perform well. These three modes have high energy density ratios of 39.2, 32.0 and 36.1, respectively, while the other three modes have ratios around 6 or lower.

The presented 2D models reproduce the transverse half-wavelength picture, but the

models clearly show the presence of pressure oscillations along the axial direction, unless the geometries of the surrounding chip is designed correctly. In Chap. 8 we present experimental investigations of α-chips based on the 2D models to compare the qualitative behaviors of the pressure resonances. Unfortunately, direct comparison of resonance patterns have not yet been possible as a better experimental imaging system is needed.

The quantitative behavior of real chip systems is believed to be poorly approximated by the 2D models as typical experimental chips do have pressure dynamics along the vertical z-direction. We therefore turn our attention to 3D models in the next section.

5.3 Analysis of 3D models

The next natural step is to investigate the antisymmetric half-wavelength modes in 3D models. We consider the system in Fig. 5.8 corresponding to α-chips experimentally investigated in Chap. 8. In the 3D models we consider the height of the silicon chip and the pyrex glass lid. In this section we (*i*) give a rough estimate of the frequency shift from 2D to 3D models, (*ii*) carry out a full 3D Comsol simulation, and (*iii*) introduce translational invariant geometries.

5.3.1 Estimation of frequency shift from 2D to 3D models

Typical experimental chips consist of a silicon chip bonded with a pyrex glass lid, where the bottom of the chip has the acoustically hard piezo transducer as neighboring domain, whereas the top of the pyrex lid has the acoustically soft air as neighboring domain. This enforces a standing pressure wave of approximately the quarter of a wavelength along the vertical z-direction. This will contribute to the chips resonance frequencies.

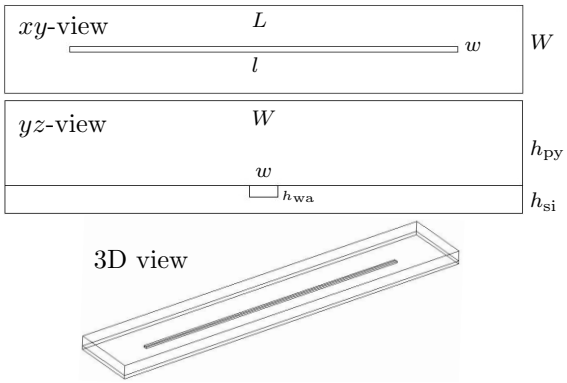

Length, chip	L	50.00	mm
Length, channel	l	40.00	mm
Width, chip:	$W = w\left(1 + \frac{c_{si}}{c_{wa}}\alpha\right)$		
$\alpha = 1$	$W_{\alpha=1}$	2.52	mm
$\alpha = 2$	$W_{\alpha=2}$	4.67	mm
Width, channel	w	0.375	mm
Height, silicon chip	h_{si}	0.350	mm
Height, pyrex lid	h_{py}	1.13	mm
Height, water channel	h_{wa}	0.157	mm

Figure 5.8: Sketch of the 3D chip model. The chip geometries corresponds to α-chips experimentally investigated in Chap. 8. The material parameters are given in Table 2.1. The model system consists of a water-filled channel having width w, length l and height h_{wa}. The channel is etched into a surrounding silicon chip of width W, length L and height h_{si}, and the silicon chip is bonded with a pyrex glass lid of width W, length L and height h_{py}. The origin of the coordinate system is placed at the center of the chip at the interface between the channel and the lid.

We estimate this contribution by making use of the analytical result of the frequency in Eq. (2.18) for a single-domain box. Using Eq. (2.18) we write

$$f_{3\mathrm{D}} \approx f_{2\mathrm{D}} \sqrt{1 + \Big(\frac{c_H}{2H} \frac{n_z}{f_{2\mathrm{D}}} \Big)^2}, \tag{5.7}$$

where $c_H = (c_{\mathrm{si}} h_{\mathrm{si}} + c_{\mathrm{py}} h_{\mathrm{py}})/H$ is a weighted approximate average speed of sound along the chip height $H = h_{\mathrm{si}} + h_{\mathrm{py}}$ and n_z is the estimated number of vertical half-wavelengths. Notice that $f_{3\mathrm{D}}$ reduces to $f_{2\mathrm{D}}$ for $n_z \to 0$ corresponding to no pressure dynamics along the height of the chip. Inserting $n_z = 1/2$ and using the material parameters of Table 2.1 we get $f_{3\mathrm{D}} \approx 2.26$ MHz for $f_{2\mathrm{D}} = 2.00$ MHz. The estimated frequency from the 2D to 3D models is therefore an increase of $\sim 13\%$.

5.3.2 Full 3D-simulation

Full 3D simulations of the acoustic chip systems are computational very expensive in memory, which limits the accuracy of the calculations. In this section, we thus carry out a full 3D simulation for comparison to computational cheap models making use of translational invariance along the axial x-direction.

Utilizing symmetry along x and y, we present in Fig. 5.9 a full 3D Comsol calculation of the lowest transverse antisymmetric pressure eigenmode for the chip having $\alpha = 1$. The model is implemented in the same manner as given in Chap. 3. We apply continuity conditions at the interfaces between the water and silicon domains, soft wall condition at the silicon/air interfaces and hard wall condition at the silicon/piezo transducer interface.

The frequency of the mode is $f = 2.4501$ MHz, which is approximately 0.45 MHz larger than frequencies calculated in the 2D models in Sec. 5.2, and it is about double the size as estimated by Eq. (5.7). Though, we see from the $(x, y, 0)$-projection in Fig. 5.9 (c) that the qualitative behavior of the pressure mode is identical to the 2D calculation in Fig. 5.7 (A).

In Chap. 8 we show experimentally, that the corresponding α-chip is able to focus polystyrene particles to the center of the channel for frequencies at least as low $f \approx 2.0$ MHz. Antisymmetric transverse modes therefore exist experimentally for this frequency and we conclude that there is a discrepancy between the theoretical 3D model and the experiments. We believe that the discrepancy is due to the neglect of the elastic shear waves in the solids in the chip. The size of the discrepancy in frequency is 0.45 MHz, which can be qualitatively justified by the estimated 15–20% drop in speeds of sound between the longitudinal sound velocities and the average of the longitudinal and transverse velcocities in the solids Eq. (2.55). Unfortunately the use of the average speeds of sound in the 3D model, does not contribute to a significant decrease in frequency. We therefore leave the discrepancy for explanation in future work including the elastic wave theory for the solids.

5.3.3 Translational invariant geometries

With the preliminary treatment of the full 3D models, we now turn our focus to translational invariant geometries along the x-axis, such that the length of the chip equals the

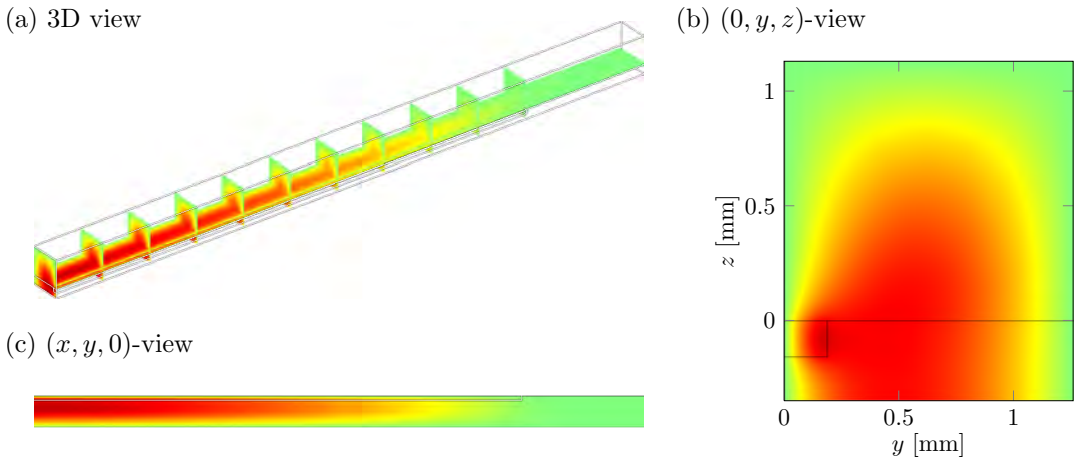

Figure 5.9: 3D COMSOL calculation of the lowest antisymmetric pressure eigenmode for the chip with $\alpha = 1$ with geometrical parameters as in Fig. 5.8 and material parameters as in Table 2.1. The frequency is $f = 2.4501$ MHz. The origin of the coordinate system is placed at the center of the chip at the interface between the channel and the lid, and symmetry at $y = 0$ and $x = 0$ is utilized. The color plots (red positive, green neutral) show the acoustic pressure eigenmodes in (a) three dimensions, (b) a cross-sectional cut at $(0, y, z)$ and (c) a cross-sectional cut at $(x, y, 0)$.

length of the channel $L \equiv l$. This is done (i) to reduce the size of the computations, and (ii) to avoid the presence of the empty areas at the end of the channel. The latter is believed to enable more direct comparison between theory and experiments, as it lowers the number of resonances of low importance. It is seen in Fig. 5.7 that many of the resonances are living in the unimportant area at the chip ends outside the channel. Moreover, during the experimental work of the current thesis, PhD student Per Augustsson from the group of Laurell proved the possibility of realizing translational invariant experimental chips.

We describe the translational invariant problem by choosing the solution of the x-component of the pressure field to $p(x) \propto \cos(k_x x)$ with $n_x = 2L/\lambda_x$. This reduces the 3D Helmholtz equation to a 2D problem in the (y, z)-plane

$$\left[-k_x^2 + \nabla^2 \right] p_i(y, z) = -\frac{\omega^2}{c_i^2} p_i(y, z), \tag{5.8}$$

for the i'th domain material.

The implementation of the translational invariant model is shown in Chap. 3 on the numerical calculations in COMSOL MULTIPHYSICS. The translational solution for the lowest transverse pressure eigenmode with $n_x = 1$ is plotted in Fig. 5.10 (a) for the chip having $\alpha = 1$. The translational invariant calculation reproduces the full 3D simulation in Fig. 5.9, but the frequencies deviate with ~ 60 kHz. This deviation is believed mainly to stem from the poor mesh resolution in the full 3D model. The results from the full 3D model uses 6 elements per wavelength, whereas the results from the translational invariant model uses 50 elements per wavelength.

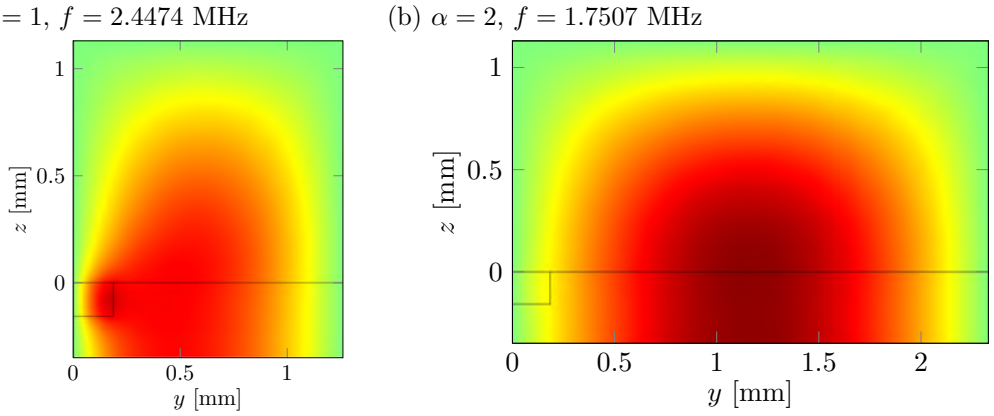

Figure 5.10: 3D COMSOL calculations of the lowest transverse antisymmetric pressure eigenmodes with $n_x = 1$ for translational invariant chips with (a) $\alpha = 1$ and $f = 2.442$ MHz and (b) $\alpha = 2$ and $f = 1.742$ MHz. The geometrical parameters are given in Fig. 5.8, while the material parameters are given in Table 2.1. The origin of the (y, z)-coordinate system is placed at the center of the chip at the interface between the channel and the lid, and we utilize symmetry at $y = 0$.

In Fig. 5.10 (b) we show the calculation of the lowest transverse pressure eigenmode with $n_x = 1$ for the translational invariant model of the chip having $\alpha = 2$. The frequency is $f = 1.742$ MHz, which is lower than the frequency for the corresponding mode for the chip having $\alpha = 1$. We recognize this behavior from Fig. 5.3 (a) in Sec. 5.1 for the 1D model, which predicts that the frequency of each mode decreases, as we increase the size of the surrounding silicon chip.

5.4 Concluding remarks

We have conducted a thorough analysis of the transverse half-wavelength picture in a water-filled channel surrounded by a silicon/glass chip. The 1D and 2D models are well understood, but the 3D analysis must be subject for further extensions, due to the obtained quantitative discrepancy to experimental results. We also need to investigate the distribution of the acoustic energy densities in the 3D models. Moreover, further work with the 3D models can result in a correction for the α-parameter, such that dimensions of the chip can be optimized to give the best possible resonance modes in the water-filled channel.

We are now ready to investigate chip designs of higher complexity, which will be the topic of the next section where we qualitatively analyze two chip applications by our 2D model.

Chapter 6

Many-channel chips

We turn our attention to consider chip systems with two or more channels. As discussed in Chap. 5 it is of importance to match the dimensions of the surrounding chip to that of an internal channel in order to optimize the acoustic resonance. The investigation of many-channel chips is thus the natural extension of the previous analysis on the transverse half-wavelength analysis. We examine two many-channel applications; (*i*) a separation chip with eighth parallel channels for high throughput and (*ii*) a three-channel chip for *in situ* calibration of the acoustic pressure force.

6.1 Parallel channel chips

A natural way to increase throughput is to use parallel channels. A photo of a eight-channel separation chip from the group of Laurell is shown in Fig. 6.1 [35]. For simplicity we study a similar chip design, but we omit the joints at the end of the channels. The main focus of the study is to examine the acoustic energy density in the system for different chip geometries. The analysis is carried out by the 2D Comsol model as used in Chap. 5 for water-filled channels in a surrounding silicon chip. The used material parameters are given in Table 2.1. It is the hope to couple this study to future experimental measurements in

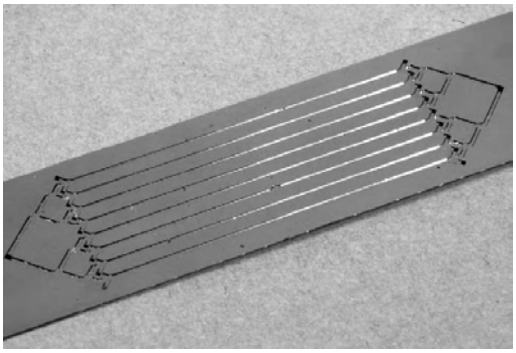

Figure 6.1: Eight-channel separation chip designed and fabricated in the group of Laurell. Photo is from Jönsson *et al.* [35].

Table 6.1: 2D COMSOL simulations of antisymmetric transverse modes in silicon chip containing eight parallel water-filled channels. For two chip designs, $\alpha = 1$ and $\alpha = 0.47$, we present the energy density ratio for the i'th channel $\mathcal{E}_{\rm wa}^{(i)}/E_{\rm si}^{\rm max}$ and the average energy density ratio for all the channels $\mathcal{E}_{\rm wa}^{\rm av}/E_{\rm si}^{\rm max}$.

α	f[MHz]	$\mathcal{E}_{\rm wa}^{\rm av}/E_{\rm si}^{\rm max}$	$\mathcal{E}_{\rm wa}^{(1)}/E_{\rm si}^{\rm max}$	$\mathcal{E}_{\rm wa}^{(2)}/E_{\rm si}^{\rm max}$	$\mathcal{E}_{\rm wa}^{(3)}/E_{\rm si}^{\rm max}$	$\mathcal{E}_{\rm wa}^{(4)}/E_{\rm si}^{\rm max}$
1.00	1.9520	**39.4**	39.4	39.4	39.4	39.4
0.47	1.9496	**16.4**	13.2	20.0	6.9	25.5

the group of Laurell.

We reuse the former channel geometries from the 2D models in Chap. 5 to create the chip with eight parallel channels. Resulting modes for two chips of different values of α are shown in Fig. 6.2. Between two neighboring channels we have the distance $2b = w(c_{\rm si}/c_{\rm wa})\alpha$. The pressure eigenmodes are plotted as color plots (red is positive, blue is negative) and for each color plot we plot the pressure along the transverse y-direction at $l/2$ for one symmetric half. Besides the pressure distributions, we compare the chips based on the spatially averaged energy density for the i'th water-filled channel to the maximum acoustic energy density in the silicon chip $\mathcal{E}_{\rm wa}^{(i)}/E_{\rm si}^{\rm max}$.

We note the obvious difference in homogeneity in pressure amplitudes from the perfectly matching mode in the $\alpha = 1$ chip to the badly matching mode in the arbitrarily chosen $\alpha = 0.47$ chip. Regarding the energy ratios, the perfectly matching chip mode has an homogeneous average energy density ratio of 39.4, whereas the mode in the non-matching chip has an inhomogeneous energy density with an average ratio of 16.4. The results are listed in Table 6.1. The two examples presented clearly demonstrate the importance of designing the chip surrounding the water-filled channel properly. The next step for this analysis is thus to verify the calculations by 3D simulations, which is not a part of the current thesis.

6.2 *In situ* calibration of acoustic pressure forces on particles

When applying standing ultrasound waves in microfluidic systems, it is difficult to measure or calibrate the acoustic pressure force exerted on a particle in solution. Acoustic power sent from the transducer to the microfluidic system suffers losses due to heating in the system and acoustic radiation to the surroundings. These losses are hard to measure, and at the same time it is difficult to mount pressure sensors inside the microfluidic system for direct determination of the acoustic power actually present. Based on the insight obtained in Chap. 5, regarding the global wave nature of the pressure eigenmodes, we present in the following a possible chip design for *in situ* calibration of the acoustic pressure force from a standing ultrasound wave on suspended spherical particles in a microfluidic channel. The method relies on determining the critical flow velocity above which the particles cease to be trapped by the ultrasound forces.

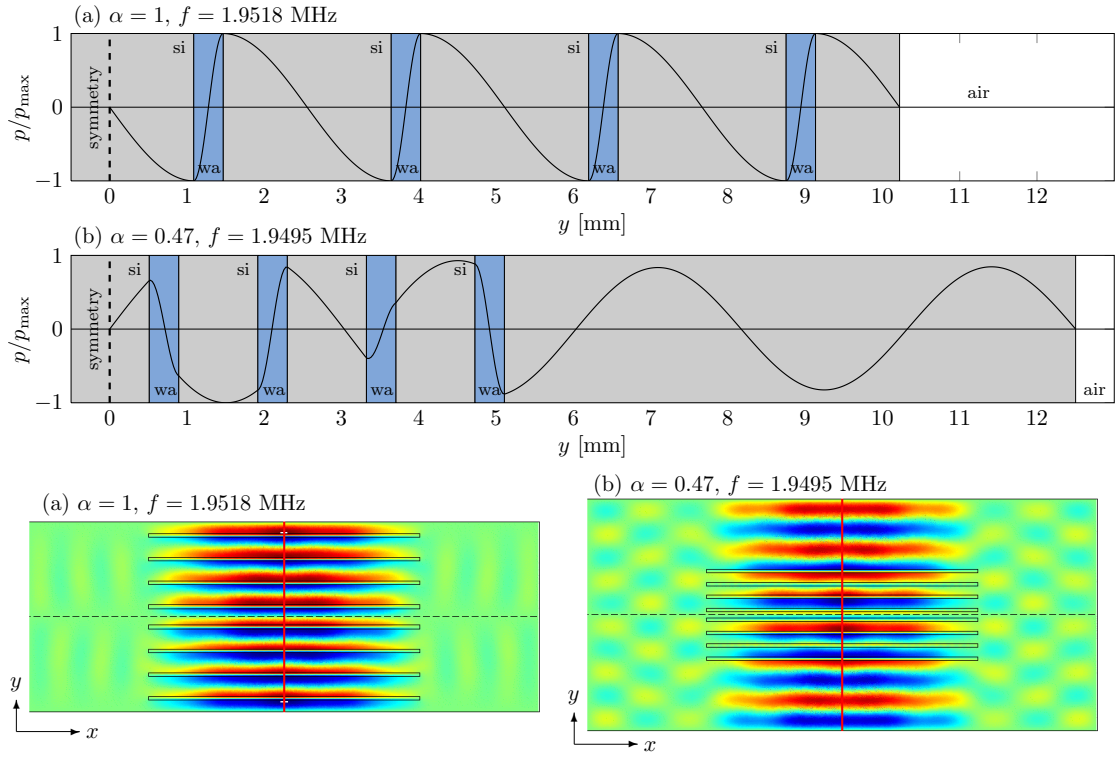

Figure 6.2: 2D COMSOL simulations of silicon chips (si/gray) length $L = 55.00$ mm containing eight parallel water-filled channels (wa/blue) each of width $w = 0.38$ mm and length $l = 29.30$ mm. Two chips are shown; (a) $\alpha = 1$ between channels and to the silicon edge, and (b) $\alpha = 0.47$ between channels and $\alpha = 6.80$ to the silicon edge. For each shown resonance the pressure amplitude is plotted as a surface plot showing the entire chip and as a symmetric cross-sectional plot along the transverse y-direction. For each plot the pressure is normalized to the maximum pressure for that given mode.

6.2.1 The acoustic potential experienced by a particle

According to Eq. (2.36), the acoustic force acting on a particle in solution can be calculated once the pressure eigenmode p is known. Our previous analysis for straight 2D channels of length l and width w have shown that to a good approximation these eigenmodes are given by simple sine/cosine standing waves in a water channel surrounded by infinitely hard walls. Such an idealized 2D pressure eigenmode is given by

$$p_1(x,y) = +p_A \cos(k_x x)\cos(k_y y), \tag{6.1a}$$

$$\nabla p_1(x,y) = -k_x p_A \sin(k_x x)\cos(k_y y)\boldsymbol{e}_x - k_y p_A \cos(k_x x)\sin(k_y y)\boldsymbol{e}_y, \tag{6.1b}$$

$$\boldsymbol{k} = k_x \boldsymbol{e}_x + k_y \boldsymbol{e}_y. \tag{6.1c}$$

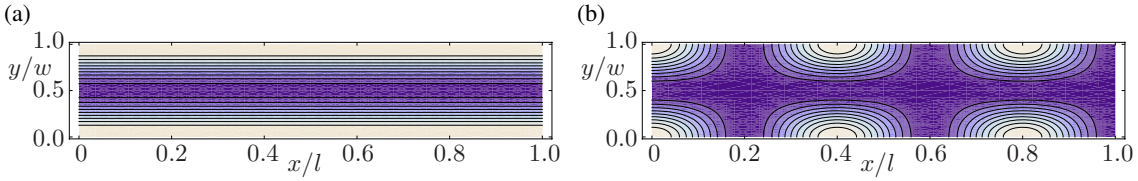

Figure 6.3: (a) Contour plot with 10% contour lines from low (dark) to high (light) of the normalized acoustic potential U_{ac}/U_0 from Eq. (6.3a) for a polystyrene sphere in water given the ideal 1D pressure field p_1 of Eq. (6.1a) with $(k_x, k_y) = (0, \pi/w)$ so that $\theta = 90°$. (b) Similar plot for the 2D pressure field with $(k_x, k_y) = (\pi/(2w), \pi/w)$ so that $\theta \approx 63°$. The parameter values used are given in Table 2.1.

This standing wave can be interpreted as the result of two counter-propagating waves along the direction $\boldsymbol{k}$, which forms the angle θ with the x-axis,

$$\cos\theta = \frac{k_x}{k}, \quad \sin\theta = \frac{k_y}{k}, \quad k = \sqrt{k_x^2 + k_y^2}. \tag{6.2}$$

Inserting this in Gorkov's expression Eq. (2.36), we find the acoustic potential U_{ac} and its amplitude U_0

$$\begin{aligned} U_{\mathrm{ac}} = U_0 \Big[& 2f_1 \cos^2(k_x x)\cos^2(k_y y) - 3f_2 \sin^2(k_x x)\cos^2(k_y y)\cos^2\theta \\ & - 3f_2 \cos^2(k_x x)\sin^2(k_y y)\sin^2\theta \Big], \end{aligned} \tag{6.3a}$$

$$U_0 = \frac{p_{\mathrm{A}}^2 V}{8\rho_{\mathrm{wa}} c_{\mathrm{wa}}^2}. \tag{6.3b}$$

Two numerical examples of the acoustic potential U_{ac} for a polystyrene sphere are shown in Fig. 6.3.

6.2.2 Chip design for *in situ* calibration of the acoustic pressure force

The acoustic pressure force on a suspended particle can be measured *in situ* if it is anti-parallel to the Stokes drag force from the flow of the carrier liquid along the axial x-direction. By gradually increasing the flow velocity v from zero, a critical value v^* can be determined, where the acoustic pressure force no longer traps the particle. At this point $|\boldsymbol{F}_{\mathrm{ac}}| \approx 6\pi\eta a v^*$, and the unknown pre-factor U_0 can be determined. The calibration setup requires that $\boldsymbol{k}$ and $\boldsymbol{e}_x$ are parallel, thus $k_x \neq 0$ while $k_y = 0$. By combining Eq. (2.35b) and Eq. (6.3) with this form of the wave vector, we obtain the acoustic potential and the associated pressure force for calibration purposes on the form

$$U_{\mathrm{ac}}^{\mathrm{calib}} = U_0 \big[2f_1 \cos^2(k_x x) - 3f_2 \sin^2(k_x x) \big], \tag{6.4a}$$

$$\boldsymbol{F}_{\mathrm{ac}}^{\mathrm{calib}} = 2k_x U_0 \left[\frac{5\tilde{\rho} - 2}{2\tilde{\rho} + 1} - \frac{1}{\tilde{\rho}\tilde{c}^2} \right] \sin(2k_x x)\, \boldsymbol{e}_x. \tag{6.4b}$$

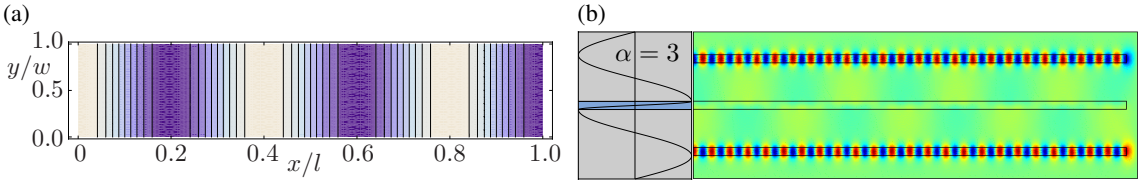

Figure 6.4: (a) Contour plot with 10% contour lines from low (dark) to high (light) of the normalized acoustic potential $U_{\rm ac}^{\rm calib}/U_0$ from Eq. (6.4a) for a polystyrene sphere in water given the pressure field $p_1 = p_{\rm A}\cos(\pi x/2w)$. The parameter values are given in Table 2.1, and moreover $k_x = \pi/(2w)$ while $k_y = 0$ so that $\theta = 0$. (b) Color plot of the pressure eigenmode in the triple-channel $\alpha = 3$ chip. A transverse potential, as in panel (a), suitable for *in situ* acoustic force calibration is set up in the two side channels, while the center channel supports a transverse mode of odd symmetry as in Fig. 5.7 ($\rm D_+$). The left insert shows the single-channel $\alpha = 3$ chip. Note the two anti-nodes in the silicon chip (gray) above and below the water-filled channel (blue).

The potential $U_{\rm ac}^{\rm calib}$ is shown in Fig. 6.4 (a). The condition for trapping becomes $F_{\rm drag} = \max\{|\boldsymbol{F}_{\rm ac}^{\rm calib}|\}$ or

$$6\pi\eta a v^* = 2k_x U_0 \left[\frac{5\tilde{\rho}-2}{2\tilde{\rho}+1} - \frac{1}{\tilde{\rho}\tilde{c}^2}\right]. \tag{6.5}$$

If v^* is measured experimentally, we are therefore able to determine the acoustic energy scale U_0 by

$$U_0 = 3\pi\frac{\eta a v^*}{k_x}\left[\frac{5\tilde{\rho}-2}{2\tilde{\rho}+1} - \frac{1}{\tilde{\rho}\tilde{c}^2}\right]^{-1}. \tag{6.6}$$

We propose a specific chip design which supports a pressure eigenmode close to the one depicted in Fig. 6.4 (a). The idea is to fabricate an $\alpha = 3$ chip. In such a chip a strong pressure eigenmode of odd symmetry exists in the channel as the $\alpha = 1$ chip in Fig. 5.7 (a) but it will also have a strong anti-node in the silicon as the $\alpha = 2$ chip in Fig. 5.7 (b). Now, if two auxiliary side channels parallel to the first channel is placed at these anti-nodes, the pressure mode inside these side channels is very close to the wanted mode of Fig. 6.4 (a). The correctness of this line of reasoning is proved by numerical simulation of the eigenmodes in such a triple-channel $\alpha = 3$ chip as shown in Fig. 6.4 (b).

Chapter 7

Waveguide analysis

In this chapter we investigate the conditions for which a straight water-filled channel of uniform cross-section will act as a waveguide within its surrounding silicon/pyrex chip, such that the acoustic pressure confines in the channel, while it decays exponentially into the surrounding silicon chip and restrain from living outside the water-filled channel.

We first carry out analytical estimates for the geometric requirements, whereafter we numerically examine the predictions by 2D and 3D Comsol models.

7.1 2D acoustic waveguide

7.1.1 Estimation of waveguide conditions

We consider the case where the length L of the silicon/pyrex chip equals the length l of the water-filled channel. This makes the system translational invariant along the axial x-direction as discussed in Sec. 5.3.3. We search solutions for the pressure $p(x, y) = p(x)p(y)$ to the Helmholtz equation Eq. (2.17). We describe the x-component of the solution by the standing resonance wave $p(x) \propto \cos(k_x x)$ with $n_x = 2L/\lambda_x$. This reduces the problem to 1D along the transverse y-direction as sketched in Fig. 5.1 and described as

$$\left[-k_x^2 + \partial_y^2 \right] p_i(y) = -\frac{\omega^2}{c_i^2} p_i(y), \tag{7.1}$$

for the i'th domain material. We notice that $p_i(y)$ may be a hyperbolic function, else only sine/cosine solutions are valid as described in 1D calculations in Sec. 5.1.

Using the proper symmetry boundary condition Eq. (2.47) at $y = -a$ and the soft boundary condition Eq. (2.46) at $y = b$, while demanding that the pressure must fall off exponentially in the chip outside the channel, results in

$$p_{\mathrm{wa}}(x, y) = A_{\mathrm{wa}} \cos\left[k_{\mathrm{wa}}(y + a)\right] \cos(k_x x) \quad \text{(even)}, \tag{7.2a}$$

$$p_{\mathrm{wa}}(x, y) = A_{\mathrm{wa}} \sin\left[k_{\mathrm{wa}}(y + a)\right] \cos(k_x x) \quad \text{(odd)}, \tag{7.2b}$$

$$p_{\mathrm{si}}(x, y) = A_{\mathrm{si}} \sinh\left[k_{\mathrm{si}}(y - b)\right] \cos(k_x x). \tag{7.2c}$$

where A_{wa} and A_{si} are pressure amplitudes. Inserting Eqs. (7.2) in Eq. (7.1) gives the equations for the wave vectors k_{wa} and k_{si}

$$-k_x^2 - k_{\text{wa}}^2 = -\frac{\omega^2}{c_{\text{wa}}^2}, \tag{7.3a}$$

$$-k_x^2 + k_{\text{si}}^2 = -\frac{\omega^2}{c_{\text{si}}^2}. \tag{7.3b}$$

Notice that Eq. (7.3b) cannot be fulfilled for $k_x \leq k_{\text{si}}$ if $\omega \neq 0$. Employing the interface conditions Eq. (2.41) at $y = 0$, results in transcendental equations for even and odd pressure eigenmodes

$$\frac{\cot(k_{\text{wa}}a)}{k_{\text{wa}}a} = \frac{\rho_{\text{si}}}{\rho_{\text{wa}}}\frac{b}{a}\frac{\tanh(k_{\text{si}}b)}{k_{\text{si}}b} \quad \text{(even)}, \tag{7.4a}$$

$$\frac{\tan(k_{\text{wa}}a)}{k_{\text{wa}}a} = -\frac{\rho_{\text{si}}}{\rho_{\text{wa}}}\frac{b}{a}\frac{\tanh(k_{\text{si}}b)}{k_{\text{si}}b} \quad \text{(odd)}, \tag{7.4b}$$

which together with Eqs. (7.3) describe the full problem for even and odd pressure eigenmodes that decay exponentially into the silicon.

Critical limit

We consider the critical limit where the wave in silicon starts decaying exponentially. We define this critical limit where the curvature of the pressure field in the silicon disappears $\partial_y^2 p_{\text{si}}(x, y) = 0$ and thus decays linearly

$$p_{\text{si}}(x, y) = A_{\text{si}} k_{\text{si}} (y - b) \cos(k_x x). \tag{7.5}$$

At the critical limit the wave stops propagating in the silicon giving the wave vector $k_{\text{si}} \to 0$. As $\tanh(k_{\text{si}}b)/k_{\text{si}}b \to 1$ for $k_{\text{si}} \to 0$, Eqs. (7.4) become

$$\frac{\cot(k_{\text{wa}}a)}{k_{\text{wa}}a} = \frac{\rho_{\text{si}}}{\rho_{\text{wa}}} \quad \text{(even)}, \tag{7.6a}$$

$$\frac{\tan(k_{\text{wa}}a)}{k_{\text{wa}}a} = -\frac{\rho_{\text{si}}}{\rho_{\text{wa}}} \quad \text{(odd)}, \tag{7.6b}$$

which have solutions for $k_{\text{wa}}a \approx \pi$ (even) and $k_{\text{wa}}a \approx \pi/2$ (odd), respectively. Together with Eqs. (7.3) we get the waveguide conditions

$$L \leq \frac{w}{2}\frac{c_{\text{si}}}{c_{\text{wa}}} n_x \quad \text{(even)}, \tag{7.7a}$$

$$L \leq w\frac{c_{\text{si}}}{c_{\text{wa}}} n_x \quad \text{(odd)}, \tag{7.7b}$$

where n_x is the number of axial half-wavelengths. We see that the constraint on obtaining waveguide modes is determined by the correct relation between between n_x and L.

7.1.2 Numerical verification of 2D waveguide conditions

To verify the derived waveguide conditions we implement a translational invariant 2D model in COMSOL as described in Chaps. 3 and 5. The COMSOL script is seen in Appendix F. In the following we consider the antisymmetric modes and thus only the constraint in Eq. (7.7b).

Fig. 7.1 (a) shows the pressure eigenmodes solved for a water-filled channel of width $w = 375$ μm in a chip width $\alpha = 1$. Three cases are shown for fixed length $L = 40$ mm but varying $n_x = [0.1, 1, 10] \times L/(\frac{c_{\rm si}}{c_{\rm wa}} w)$ corresponding to values of n_x being 2, 19 and 186, respectively. These three solutions are exactly the same for constant $n_x = 1$ and L being 21.47 mm, 2.15 mm and 0.21 mm, respectively.

The waveguide condition is not fulfilled for $n_x = 2$ (dotted line) and the pressure eigenmode lives in the silicon. We recognize this mode as the perfectly matching antisymmetric mode discussed in Fig. 5.6 (A). For $n_x = 19$ (dashed line) the waveguide condition is exactly fulfilled and the pressure eigenmode decays linearly into the silicon. For $n_x = 186$ (solid line) the waveguide condition is very well realized and the pressure eigenmode decays exponentially into the silicon.

Table 7.1 gives the corresponding results for the three pressure eigenmodes for $n_x = 2, 19, 186$ for fixed $L = 40$ mm. As clearly visible in Fig. 7.1 (a), we see that the modes for ($n_x = 19, 186$) have lower wavelengths in the water-filled channel as the perfectly matching mode for n_x. The mode for $n_x = 19$ is 4% smaller than $w/2$, whereas the pressure eigenmode for $n_x = 186$ is 54% smaller than $w/2$. Adversely, the energy density ratio $\mathcal{E}_{\rm wa}/\mathcal{E}_{\rm si}$ is 38.5 for $n_x = 2$, 52.8 for $n_x = 19$, and 54.9 for $n_x = 186$. As the width of the chip increase, the advantage in energy density ratio are even more profound for the

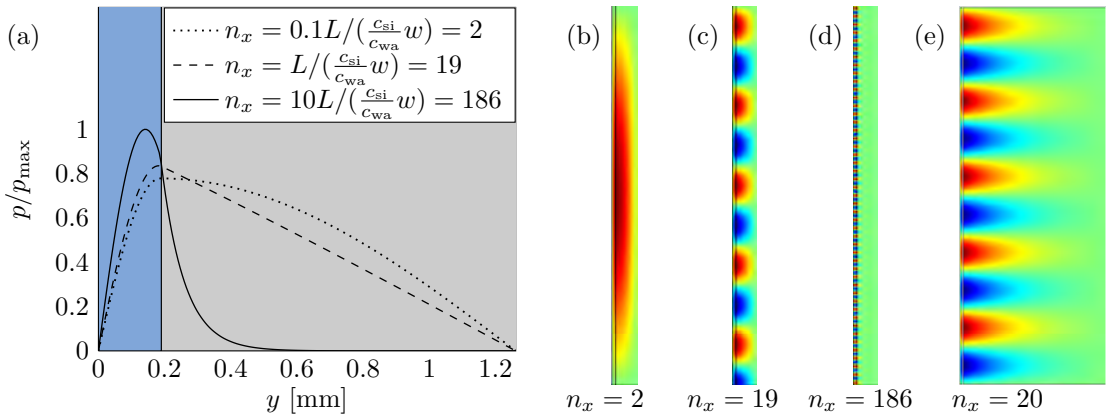

Figure 7.1: 2D COMSOL calculations for waveguide modes in water-filled microchannel of width $w = 375$ μm inside a silicon chip with $\alpha = 1$. The system is translational invariant along the axial x-direction. (a) Pressure eigenmodes for fixed $L = 40$ mm with $n_x = [0.1, 1, 10] \times L/(\frac{c_{\rm si}}{c_{\rm wa}} w)$ corresponding to values of n_x being 2, 19 and 186, respectively. (b,c,d) 2D color plots (red is positive, blue is negative) of the pressure eigenmodes for $n_x = 2$, $n_x = 19$ and $n_x = 186$, respectively. Notice that only a single-symmetric quarter of the chip is plotted. (e) 2D color plot of pressure eigenmode for $n_x = 20$ for a silicon chip with $\alpha = 7$.

Table 7.1: Results of 2D COMSOL simulations of antisymmetric waveguide modes for a water-filled channel of width $w = 375$ µm in a silicon chip having $\alpha = 1$. Presented are results for three mode types; a non-guiding mode, a mode exactly at the guiding limit and a mode strongly guiding the acoustic energy. δ is the relative deviation in half-wavelength from $w/2$ and $\mathcal{E}_{\mathrm{wa}}/\mathcal{E}_{\mathrm{si}}$ is the energy density ratio between the average acoustic energy density in the water-filled channel to the average acoustic energy density in the silicon chip.

Mode type		L [mm]	n_x	L [mm]	n_x	f [MHz]	δ [%]	$\mathcal{E}_{\mathrm{wa}}/\mathcal{E}_{\mathrm{si}}$
No guide	$L > w\frac{c_{\mathrm{si}}}{c_{\mathrm{wa}}}n_x$	40.0	2	21.47	1	1.9783	-0.1	38.5
Limit	$L = w\frac{c_{\mathrm{si}}}{c_{\mathrm{wa}}}n_x$	40.0	19	2.15	1	2.0606	-4.0	52.8
Guide	$L < w\frac{c_{\mathrm{si}}}{c_{\mathrm{wa}}}n_x$	40.0	186	0.21	1	4.3307	-54.3	54.9

wave guiding modes as no acoustic energy exists in the silicon. Note that the considered energy density ratio $\mathcal{E}_{\mathrm{wa}}/\mathcal{E}_{\mathrm{si}}$ is the ratio between the spatially averaged energy densities as the maximum energy density in silicon $E_{\mathrm{si}}^{\mathrm{max}}$ is no longer a proper measure due to the decaying modes in the silicon.

In Figs. 7.1 (b,c,d) are shown the three discussed pressure eigenmodes as color plots (red is positive, blue is negative) for the chip having $\alpha = 1$. Notice that only a single-symmetric quarter of the chip is plotted. Fig. 7.1 (e) shows the pressure eigenmode for $n_x = 20$ for a chip having $\alpha = 7$. From this it is clear that the pressure eigenmode confines completely into the water-filled channel.

As a last remark, it is clear that waveguide modes may be of high importance, since they confine the energy into the water no matter the width of the surrounding silicon.

7.2 3D acoustic waveguide

We turn to the case of creating a three-dimensional waveguide in the water-filled channel surrounded by the silicon/pyrex chip. In a translational invariant chip as discussed in Sec. 5.3 and described in Fig. 5.8, the problem reduces to a two-dimensional problem of three different domains. As we cannot solve the problem analytically, we rely on the former 1D estimate for the 2D waveguide condition and the use of COMSOL.

We modify the 2D waveguide condition to give a rough estimate for the 3D waveguide condition. The modification consists of simply substituting the speed of sound for silicon c_{si} to an approximated weighted average speed of sound $c_{\mathrm{H}} = (c_{\mathrm{si}}h_{\mathrm{si}} + c_{\mathrm{py}}h_{\mathrm{py}})/H$ of the silicon/glass chip with its total height $H = h_{\mathrm{si}} + h_{\mathrm{py}}$

$$L \leq \frac{w}{2}\frac{c_{\mathrm{H}}}{c_{\mathrm{wa}}}n_x \quad \text{(even)}, \tag{7.8a}$$

$$L \leq w\frac{c_{\mathrm{H}}}{c_{\mathrm{wa}}}n_x \quad \text{(odd)}. \tag{7.8b}$$

Using the chip parameters as given in Fig. 5.8 and Table 2.1, we get the average speed of sound $c_{\mathrm{H}} \approx 6300\ \mathrm{m\,s^{-1}}$ for the silicon/glass chip. If we consider a chip of length $L = 40$ mm

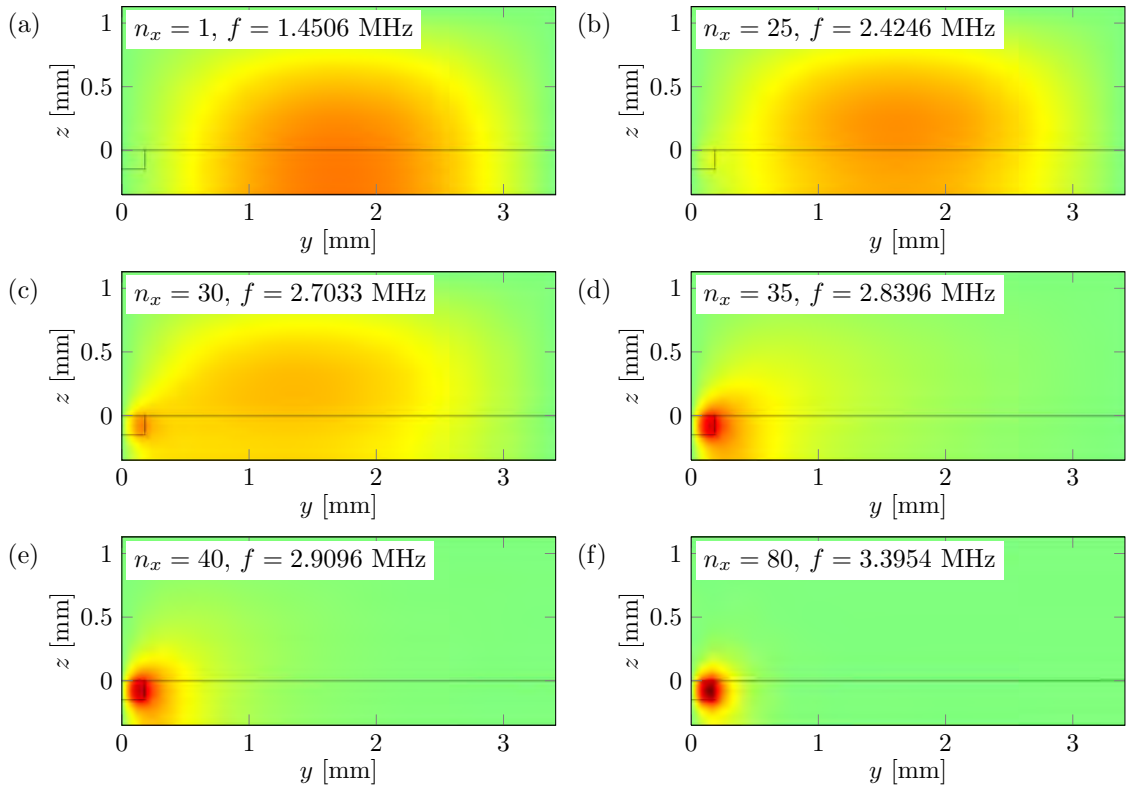

Figure 7.2: 3D COMSOL simulations of water-filled channel acting as an acoustic waveguide within a surrounding silicon/glass chip as sketched in Fig. 5.8. The chip has $\alpha = 3$ and is translational invariant along the axial x-direction with identical channel and chip lengths of $L = l = 40$ mm. The color plots (red is positive, green is neutral) show the lowest transverse antisymmetric pressure eigenmodes plotted for one symmetric half along the transverse y-direction. The chip length L is constant, while n_x is varied from (a) $n_x = 1$ to (f) $n_x = 80$. As n_x increases, the pressure eigenmode moves from mainly living in the silicon/glass chip to be almost completely confined inside the water-filled channel. For the fixed length of $L = 40$ mm, the main transition between two mode types occurs for n_x between 30 and 35.

we get the approximate requirement on the number n_x for antisymmetric modes

$$n_x \gtrapprox \frac{1}{w}\frac{c_{\mathrm{wa}}}{c_{\mathrm{H}}} L \approx 25 \quad \text{(odd)}. \tag{7.9}$$

We test the estimate of the 3D waveguide condition by COMSOL calculations shown in Fig. 7.2. The model chip has $\alpha = 3$ and is translational invariant along the axial x-direction with identical chip and channel lengths of $L = l = 40$ mm. The color plots (a–f) show the lowest transverse antisymmetric pressure eigenmodes plotted for one symmetric half along the transverse y-direction. The chip length L is kept constant, while the number n_x is varied from panel (a) $n_x = 1$ to panel (f) $n_x = 80$. As n_x increases, the pressure eigenmode moves from mainly living in the silicon/glass chip to be almost completely confined inside the water-filled channel. For the fixed length of $L = 40$ mm, the main

transition between two mode types occurs for n_x between 30 and 35. The estimate in Eq. (7.9) deviates 15–20% from the waveguide condition on n_x obtained by the numerical COMSOL calculations. This is not bad if we recall that the estimate is based on a 1D model.

7.3 Concluding remarks

We have carried out basic studies of the conditions for the water-filled channel to act as an acoustic waveguide within a surrounding silicon/glass chip. The conditions state a relationship between the channel/chip length L and the number n_x of axial half-wavelengths nodes in the pressure mode. The utilization of the water-filled channel as an acoustic waveguide seems to be promising as more acoustic energy can be obtained and more interesting, it opens the possibility for the creation of channel structures of higher geometric complexity as known from e.g. waveguides in optics. More analysis therefore has to be done within this field.

Chapter 8

Experimental investigations

In the current chapter we describe a series of experiments carried out by the author during eight days in April and May in Professor Laurell's laboratory at the Department of Electrical Measurements, Lund University. The experiments were set up and executed in close collaboration with PhD-student Per Augustsson.

The purpose of the experiments was to test theoretical predictions of resonance modes, the acoustic focusing force and the acoustic energy density. In the following we (*i*) describe the involved chips and the experimental setup, (*ii*) investigate the electrical impedance of the piezo transducer for different mechanical loads, (*iii*) describe sedimentation experiments of spherical polystyrene microbeads to calibrate the experimental parameters and (*iv*) finally determine the acoustic energy density and the corresponding transverse separation mode by simple stop-flow ultrasonic experiments.

8.1 Experimental setup

A microfluidic silicon/glass chip is acoustically actuated by a piezo transducer. The chips are fabricated by standard photolithography technique by Per Augustsson in the group of Laurell. The chips are shown in Fig. 8.1. Panel (a) shows a photograph of the four silicon/glass chips and panel (b) shows the corresponding sketch with marked dimensional parameters found in Table 8.1. The four chips are of the α-type treated in Chap. 5. Each α-chip consists of a glass-bonded silicon chip etched with a single straight rectangular channel. The four α-chips only differ by their widths. The microchannel is entered through inlet and outlet holes on top of the chip through the glass lid. At each hole a silicone tube has been attached using silicone glue.

Photographs of the experimental setup are seen in Fig. 8.2. In panel (a) is shown a full view of the setup including pump, syringe, chips, holder and microscope. Panel (b) shows how the chip is mounted on the piezo transducer and fixed in a PMMA holder, such that the chip is only in contact with the holder through its inlet/outlet silicone tubing and the piezo transducer. The chip is acoustically coupled to the transducer by a thin intermediate layer of glycerol.

The piezo transducer is made of hard PZT and is of the type Pz26 from Ferrop-

Table 8.1: Geometric parameters of fabricated α-chips and the piezo transducer.

Width, channel	w	0.377 mm	Length, channel	l	40.0 mm
Width, chip:	$W = w\left(1 + \frac{c_{\mathrm{si}}}{c_{\mathrm{wa}}}\alpha\right)$		Length, chip	L	50.0 mm
$\alpha = 1$	$W_{\alpha=1}$	2.5 mm	Length, piezo	L_{PZT}	50.0 mm
$\alpha = 2$	$W_{\alpha=2}$	4.7 mm	Height, channel	h_{wa}	0.157 mm
$\alpha = 3$	$W_{\alpha=3}$	6.8 mm	Height, si-chip	h_{si}	0.350 mm
$\alpha = 4$	$W_{\alpha=4}$	9.0 mm	Height, glass-lid	h_{py}	1.13 mm
Width, piezo	W_{PZT}	12.0 mm	Height, piezo	h_{PZT}	1.0 mm
Radius, lid holes	$R_{\alpha=1,2}$	0.5 mm	Radius, lid holes	$R_{\alpha=3,4}$	1 mm

erm Piezoceramics A/S. The piezo transducer is actuated by applying a harmonically oscillating voltage drop generated from a tone generator Hewlett Packard 33120A. The voltage is amplified by a T&C Power Conversion Inc AG Series Amplifier, while the applied peak-to-peak voltage across the piezo transducer is measured by a Tektronix TDS 1002 oscilloscope. The channel is observed by an Olympus BX51WI microscope with an attached CCD camera of the type Infinity 1 from MediaCybernetics.

To carry out the ultrasonic experiments a liquid sample is led through the channel of the chip. The sample liquid is distilled water mixed with 0.01 % Tween20, which is a polysorbate surfactant reducing the adhesion of microbeads to the channel walls. As shown by the sedimentation experiments described in Sec. 8.3 below, the influence of the added Tween20 on the density and viscosity is negligible. In the sample liquid are 5 µm polystyrene microbeads from Sigma-Aldrich. The calibrated diameter of the polystyrene microbeads is (5.16 µm ± 0.08 µm). We use bead concentrations between 0.01 and 0.05 g/mL. The sample liquid is held in a 1 mL plastic syringe, where a small magnet is added. By stirring with an external magnet we avoid sedimentation of the microbeads

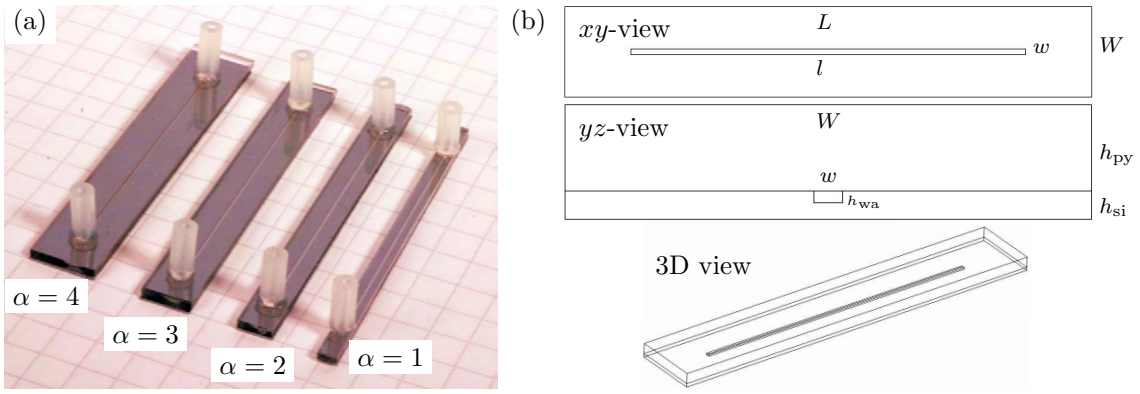

Figure 8.1: Microfluidic silicon/glass chips of the α-type fabricated by Per Augustsson in the group of Laurell. (a) Photograph of the four α-chips. (b) Sketch of the four α-chips with indicated dimensional parameters presented in Table 8.1. The four α-chips consist of a glass-bonded silicon chip etched with a straight single channel.

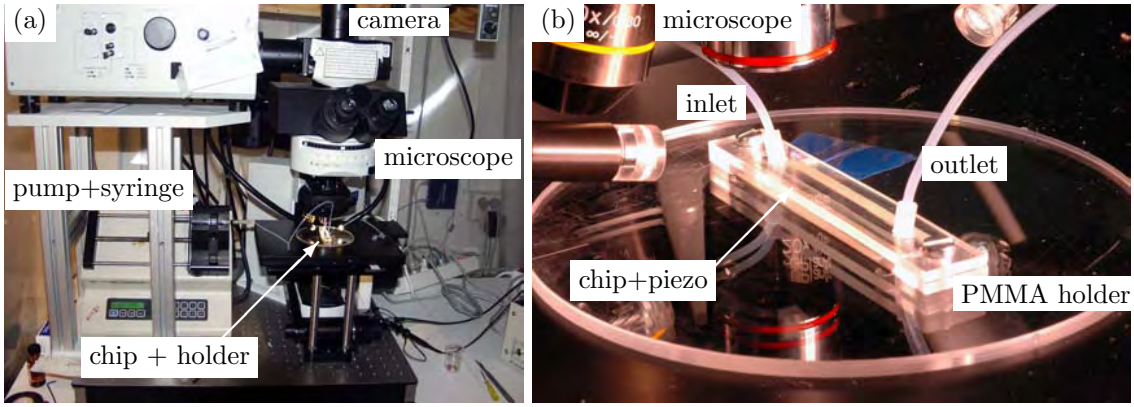

Figure 8.2: (a) Full view of the experimental setup showing a silicon/glass chip in a PMMA holder investigated by microscope with attached CCD camera. A microflow is pumped into the chip by a syringe pump. (b) Close up of the microfluidic silicon/glass chip and PMMA holder illuminated by external light sources. The microfluidic inlet and outlet are shown.

in the syringe, which reduces the chance of getting an inhomogenous distribution of microbeads in the liquid channel. A syringe pump of the type WPI SP210IWZ is used to pump the sample liquid into the microfluidic chip through plastic tubes.

8.2 Investigation of the piezo transducer

The piezo transducer, 50 mm × 12 mm × 1 mm, has its ideal acoustic resonance frequency at $f_{\text{piezo}} = 2.075$ MHz obtained by the Ferroperm online piezo electric calculator [53]. The displacement amplitude and the energy delivered from the piezo transducer depend on its applied frequency. This fact complicates the experiments as the frequency cannot just be tuned arbitrarily away from f_{piezo} without a significant decrease in the acoustic energy density. The energy loss may be compensated by amplifying the applied voltage, but this induces other complications such as additional heating of the system. Ideally we are interested in knowing the exact behavior of the piezo transducer, as it will enable us to compare energy/frequency spectra for various chips. Such a thorough investigation is outside the scope of this thesis and in the following we present an investigation limited to the electrical impedances of the piezo transducer at different acoustic loads.

Fig. 8.3 presents the measured frequency spectra of the electrical impedance Z_{el} and phase ϕ_{el} of the piezo transducer as the piezo transducer is subject to different acoustic loads. The spectra are shown in six cases added up chronologically as; (*i*) the piezo transducer hangs freely, (*ii*) the piezo transducer rests on the holder, (*iii*) glycerol is added on top of the piezo transducer, (*iv*) the chip is added on the piezo with an intermediate layer of glycerol, (*v*) the PMMA-lid is pressing down the chip through the silicone tubings or (*vi*) the PMMA-lid pressing down the chip in direct contact. The chip has $\alpha = 3$ and a water-filled channel.

The frequency spectra clearly illustrate that the piezo transducer has a large number of resonance frequencies, which is seen via the many local minima in electric impedance Z_{el}

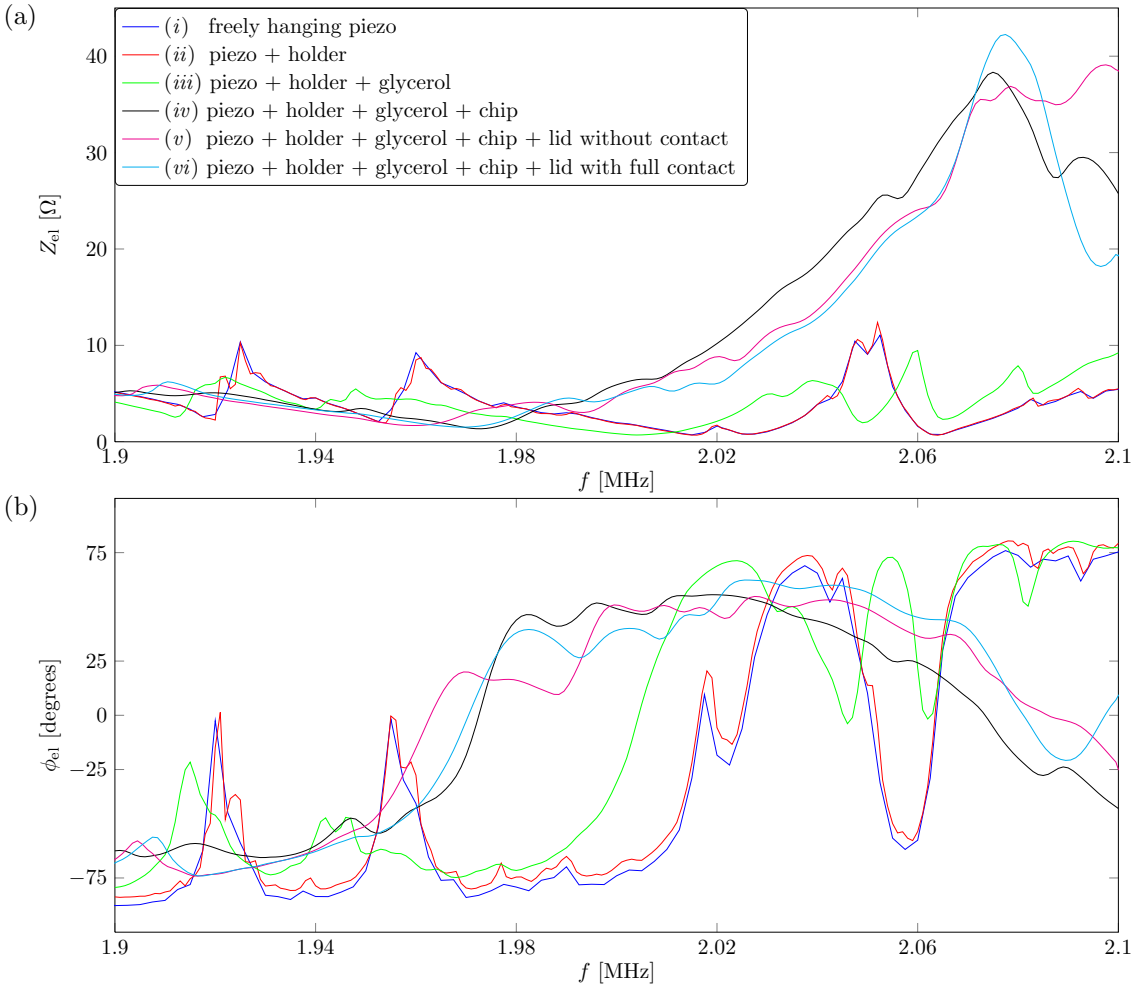

Figure 8.3: Frequency spectrum of the (a) electric impedance Z_{el} and (b) electric phase ϕ_{el} for the piezo transducer, while the piezo transducer is mechanically loaded in various combinations. Six cases of loads are shown.

accompanied by shifts in the electric phase ϕ_{el}. In addition we notice that the location and behavior of the resonances are very sensitive to the given load. Only similar cases are case (i) the piezo transducer hanging freely and case (ii) the piezo transducer resting on the holder. This justifies a disregarding of the acoustic influence from the holder. Additional, it is observed that the increase in load decreases the amount of local resonances resulting in more smooth spectra.

To sum up, the impedance measurements illuminate that the resonances of the piezo transducer are highly sensitive to different loads. This makes the acoustic behavior of the resonance systems hard to predict without being able to predict the behavior of the actuating piezo transducer itself. An opportunity for higher piezo stability is to switch the type of the piezo transducer from a Pz26 to a Pz27 as the Pz27 model has a much

lower Q-value [54].

8.3 Sedimentation of microbeads

To calibrate the liquid sample containing the microbeads, a series of sedimentation experiments were carried out.

Theoretical sedimentation times

The sedimentation time t for a microbead of radius a is theoretically approximated by assuming a non-accelerating flow. The resulting Newtons second law for the bead in the vertical z-direction includes the viscous Stokes drag $F_{\text{drag}} = 6\pi\eta a v_z$ and the specific gravitational force $F_g = -\frac{4}{3}\pi a^3 g(\rho_{\text{p}} - \rho_{\text{wa}})$ [5]. We get

$$t = \frac{9}{2}\frac{\eta}{a^2 g(\rho_{\text{p}} - \rho_{\text{wa}})}\, h_{\text{wa}}, \tag{8.1}$$

where h_{wa} is the sedimentation depth, η is the liquid viscosity, g is the gravitational acceleration and ρ_{p} and ρ_{wa} is the density of the particle and liquid, respectively. For polystyrene microbeads in water we have $a = 5.16/2$ µm and material parameters as given in Table 2.1. We get a sedimentation time

$$t \approx 208 \text{ s}. \tag{8.2}$$

A phenomenon that might play a role during the sedimentation experiments is diffusion. Utilizing the Einstein relation for the diffusion constant D [5] at room temperature yields

$$D = \frac{k_{\text{B}}T}{6\pi a\eta} \approx 8.5 \times 10^{-14}\ \text{m}^2\,\text{s}^{-1}, \tag{8.3}$$

which used to estimate the diffusion length l_{diff} during a sedimentation time of $t \approx 200$ gives

$$l_{\text{diff}} = \sqrt{D\,t} \approx 4\ \text{µm}. \tag{8.4}$$

The approximated diffusion length l_{diff} is small in comparison to the channel height h_{wa} and for this reason we neglect diffusion in the sedimentation experiments as well as in the latter experiments.

Table 8.2: Experimental sedimentation times for (5.16 µm ± 0.08 µm) polystyrene microbeads. Listed are the average sedimentation time t, the uncertainty Δt and the number of measurements N.

Liquid sample	$t \pm \Delta t$ [s]	N
Distilled water	182 ± 5	4
Distilled water (0.01 % Tween20)	179 ± 6	3

Experimentally measured sedimentation times

The liquid sample was pumped through the channel while the microbeads were focused to the channel center by acoustically actuating the chip. Due to the presence of a vertical acoustic pressure gradient as discussed in Chap. 5, the microbeads were vertically pushed towards the channel lid. The flow was stopped and some microbeads were trapped at the channel lid, while the remaining microbeads sedimented to the channel bottom. The ultrasound were turned off, and the sedimentation times were determine by following the beads in the microscope focus until they reached the bottom of the channel.

The sedimentation times t and the uncertainty Δt are presented in Table 8.2 as a result of a number of measurements N. The experiments deviate $13 - 14$ % from the theoretical prediction in Eq. (8.2). The small deviations may be found due to the theoretical approximation of constant flow velocity. Other uncertainties may be the channel height h_{wa}, sizes of the microbeads and other parameters such as the viscosity and densities. The measurements show fair accuracy in applying the Stokes drag in this confined system.

Additionally, the sedimentation times were measured for the sample liquid being either pure distilled water or distilled water with 0.01 % Tween20. The sedimentation times for the microbeads in the two mixtures did not differ significant and hence we conclude that the addition of 0.01 % Tween20 does not influence the water parameters such as density and viscosity.

8.4 Measuring the acoustic energy density

The acoustic energy density is crucial to determine as theoretical and experimental comparison of acoustic energy densities are needed in order to understand and hence optimize the experimental configurations. Possible optimization parameters can be the acoustic impedances of the surroundings to the chip. Also the chip design itself can be optimized to support local resonances with high relative acoustic energy densities, which is e.g. important in focus/separation experiments, where the acoustic energy density in the liquid-filled channels is directly proportional to the pressure force Eq. (2.38). However, the acoustic energy density is rarely determined in applications in the acoustofluidic literature. The objective of the current section is thus to determine the acoustic energy density and to examine its physical dependencies. Prior to the investigation two main expectations are set up.

Firstly, from Eq. (2.31) we expect the acoustic energy density to be proportional to the square of the applied pressure. If the voltage across the piezo transducer is directly proportional to the pressure delivered, we expect the acoustic energy density to be directly proportional to the square of the voltage applied to the piezo transducer. Secondly, from Eq. (4.13) we expect the acoustic energy density near a resonance to behave as a Lorentzian shape-line as function of the applied frequency.

The acoustic energy density is measured by observing the transient acoustophoretic focusing of the microbeads. First, the driving frequency is tuned to an acoustic resonance that strongly focuses the polystyrene microbeads to the center of the channel. The ultrasound field is turned off and a fresh solution of the liquid sample is pressed into the

channel. Then the ultrasound field is turned back on, and the transient focusing of the microbeads to the channel center is recorded by a CCD camera. From the frames of the resulting movie we can then determine the transverse paths $y(t)$ of the microbeads.

8.4.1 Theoretical transverse bead trajectory

The path of a microbead moving under acoustophoresis is given by the position vector $\big(x(t), y(t)\big)$. For more elaboration on acoustophoretic bead trajectories, see [43]. We set up a simple analytical expression for the transverse part $y(t)$ in the limit of a long axial wavelength $k_x \approx 0$. By neglecting inertial effects at the low microbead speeds, we balance the acoustophoretic force $F_{\rm ac}$ in Eq. (2.38) with the Stokes drag force $F_{\rm drag} = 6\pi\eta a\frac{\mathrm{d}y}{\mathrm{d}t}$ [5]. This results in a first-order non-linear differential equation for the transverse path $y = y(t)$

$$\frac{\mathrm{d}y}{\mathrm{d}t} = \psi_y \sin(2k_y y), \tag{8.5}$$

where

$$\psi_y = \frac{2k_y a^2 E_{\rm ac}}{9\eta}\left[\frac{5\tilde{\rho}-2}{5\tilde{\rho}+1} - \frac{1}{\tilde{\rho}\tilde{c}^2}\right]. \tag{8.6}$$

Separating the variables y and t, and using the fact that $\frac{\mathrm{d}\tan(s/2)}{\mathrm{d}s} = \frac{1}{\sin(s)}$ leads to the expression for the time t it takes a particle starting at $y(t_0) = y_0$ to reach within a microbead radius a of the position $y(t)$

$$t = t_0 - \frac{1}{2k_y\psi_y}\log\left(\frac{\tan\big[k_y y_0\big]}{\tan\big[k_y y(t)\big]}\right), \tag{8.7}$$

which is derived assuming y_0 and $y(t)$ to have same sign. Additional rewriting gives the microbead position $y(t)$

$$y(t) = \frac{1}{k_y}\arctan\left[\mathrm{e}^{k_y\psi_y(t-t_0)}\,\tan(k_y y_0)\right], \tag{8.8}$$

which will be used later to fit the acoustic energy density $E_{\rm ac}$ and wavelength $\lambda_y = 2\pi/k_y$ to the experimental (t, y)-data of the particle trajectories.

8.4.2 Analysis of data

The transverse path $y(t)$ is extracted from the video recordings by employing the free video analysis tool *Tracker 2.6* [55]. This software enables tracking a polystyrene microbead by simple manual mouse-clicking on the microbead position y for each movie frame for which the time t is known. First, the initial and end frames are chosen. Next a reference frame is chosen and the width of the channel is used to set a reference length scale. Due to the manual selection of microbeads, reference frame and length scale, the approach is connected with high uncertainties. Also the probable existence of axial modes leads to inhomogeneities in strength of the acoustic focusing force along the x-direction. With

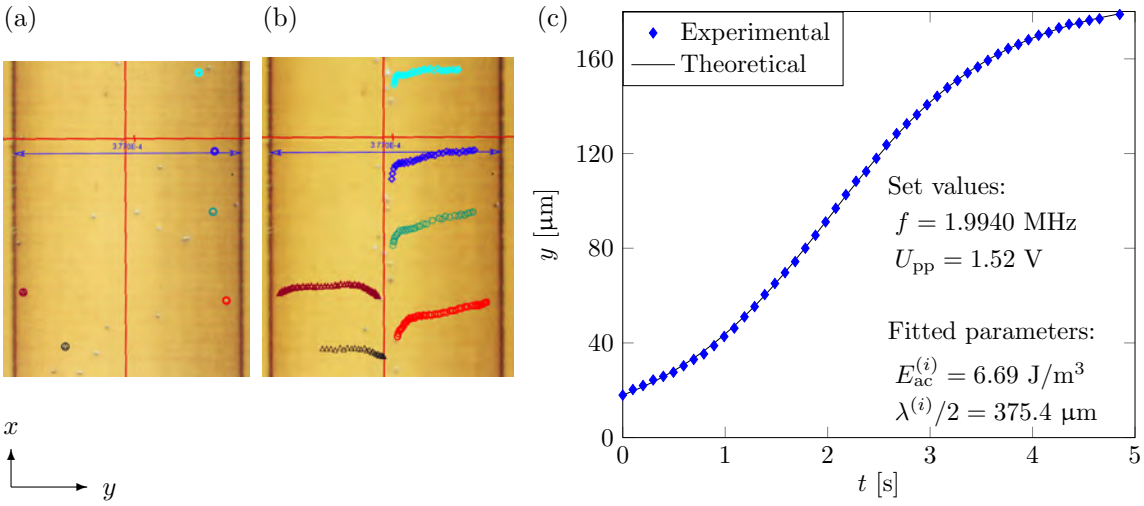

Figure 8.4: Example of extracting the acoustic energy density $E_{\mathrm{ac}}^{(i)}$ and the acoustic half-wavelength $\lambda^{(i)}/2$ from tracking the i'th single microbead at driving frequency $f = 1.9940$ MHz and driving voltage $U_{\mathrm{pp}} = 1.52$ V. The experimental data is a movie with a series of frames analyzed by the free video analysis tool *Tracker 2.6* [55]. (a) First image frame before applying ultrasound to focus the microbeads (colored circles) horizontally to the center of the channel. A reference frame (red) and a reference length scale (blue) are chosen. (b) Last image frame showing the paths of the focused microbeads. Notice the overall flow of the microbeads in the negative x-direction. This is assumed to be due to drifting in the flow caused by trapped bubbles etc. These flows are neglected as we only consider the transverse focusing. (c) Transverse trajectory curve $y(t)$ (blue points) resulting from tracking the i'th microbead and the fitted path (black line) based on Eq. (8.8) with the two fitting parameters: the acoustic energy density $E_{\mathrm{ac}}^{(i)}$ and the half-wavelength $\lambda^{(i)}/2$ of the transverse standing pressure wave.

these uncertainties in mind, at least five microbead tracks have been determined for each given movie to result in better statistics.

An example of tracking a bead trajectory is seen in Fig. 8.4 for a driving frequency of $f = 1.9940$ MHz and a driving voltage of $U_{\mathrm{pp}} = 1.52$ V. Panel (a) shows starting position, panel (b) shows the microbead trajectories and panel (c) shows the resulting path fitted by the theoretical expression for $y(t)$ Eq. (8.8). The theoretical fitting path $y(t)$ for the i'th particle track from Eq. (8.8) is obtained by fitting the acoustic energy density $E_{\mathrm{ac}}^{(i)}$ and the half-wavelength $\lambda^{(i)}/2 = \pi/k_y^{(i)}$. The is done utilizing the `MATLAB` least-squares routine `lsqcurvefit()`. In the given case we find $E_{\mathrm{ac}}^{(i)} = 6.69$ J/m^3. We also note that the fitted value for $\lambda^{(i)}/2 = 0.375$ mm is very close to the expected value of the channel width $w = 0.377$ mm.

Uncertainties

For each focus movie of N particle tracks the weighted average of the acoustic energy density $\langle E_{\mathrm{ac}} \rangle_N$ and half-wavelength $\langle \lambda \rangle_N/2$ are calculated from the fitted energy densities

$E_{\mathrm{ac}}^{(i)}$ and fitted half-wavelengths $\lambda^{(i)}/2$ with respect to the number of tracking points $n^{(i)}$ for the i'th particle path. The weighted average $\langle x \rangle_N$ for N particle paths is calculated as

$$\langle x \rangle_N = \frac{\sum_{i=1}^{N} x^{(i)}\, n^{(i)}}{\sum_{i=1}^{N} n^{(i)}}, \tag{8.9}$$

for which the corresponding sample standard deviation s_x is calculated as

$$s_x = \sqrt{\frac{\sum_{i=1}^{N} (x^{(i)} - \langle x \rangle_N)^2}{N-1}}. \tag{8.10}$$

For each movie we extract $\langle E_{\mathrm{ac}} \rangle_N$, $\langle \lambda \rangle_N/2$, s_E and $s_\lambda/2$. In the latter when analyzing the wavelength from a number of movies M, we make use of the weighted mean given by

$$\bar{x} = \sigma_{\bar{x}}^2 \sum_{j=1}^{M} \frac{\langle x \rangle_N^{(j)}}{\left(s_x^{(j)}\right)^2}, \tag{8.11}$$

where the variance $\sigma_{\bar{x}}^2$ of the weighted mean is given by

$$\frac{1}{\sigma_{\bar{x}}^2} = \sum_{j=1}^{M} \frac{1}{\left(s_x^{(j)}\right)^2}. \tag{8.12}$$

Finally we adopt the notation Δx for the standard deviation of the weighted mean given by $\Delta x \equiv \sqrt{\sigma_{\bar{x}}^2}$. We therefore expect our measured x-values to be within $x = \bar{x} \pm \Delta x$.

In the next subsections we fit theoretical curves to our data points. For each fit we run a goodness-of-fit test by the `CHI2GOF()`-function in MATLAB and make sure that the null-hypothesis is never rejected at 5% significance.

8.4.3 Acoustic energy density versus driving voltage

In the current section we determine the acoustic energy density E_{ac} as a function of the driving voltage U_{pp}. In the experiments we tuned the piezo frequency to a resonance yielding a strong transverse focusing force; in this case $f = 1.9976$ MHz. The values of $\langle E_{\mathrm{ac}} \rangle_N$, $\langle \lambda \rangle_N/2$, s_E and $s_\lambda/2$ are listed in Table 8.3. The extracted acoustic energy densities $\left\langle E_{\mathrm{ac}}\left(U_{\mathrm{pp}}^{(j)}\right)\right\rangle_N$ are fitted to a power function of the form

$$E_{\mathrm{ac}}^{\mathrm{fit}}(U_{\mathrm{pp}}) = a_1 U_{\mathrm{pp}}^{a_2}, \tag{8.13}$$

where the fitting parameters are a_1 and a_2.

In Fig. 8.5 are seen U_{pp}-sweeps for two chips; $\alpha = 1$ (a,b) and $\alpha = 2$ (c,d). For $\alpha = 1$ the fitting parameters have values of $(a_1, a_2) = (12.13, 2.09)$, whereas for $\alpha = 2$ the fitting parameters have values of $(a_1, a_2) = (3.64, 2.4)$. From the data points for $\alpha = 1$ it is evident that the exponent $a_2 \approx 2$ meaning that the acoustic energy density is proportional to the square of the driving voltage. This result is clearly indicating that the delivered

pressure from the piezo transducer is directly proportional to its applied peak-to-peak voltage.

For $\alpha = 2$ the exponent $a_2 \approx 2.4$ deviates a bit from the expected, which is assumed to be an outcome of the poor number of fitting points. Though, it is still clear that the acoustic energy density is approximately a factor of 3 lower for $\alpha = 2$ than for $\alpha = 1$. This might be experimental evidence for the α-analysis in Chap. 5, stating that for antisymmetric resonances at these frequencies, the acoustic energy density in the channel will be stronger for $\alpha = 1$ than for $\alpha = 2$. Though, we keep in mind the experimental and theoretical lack in information about the influence on the piezo transducer when changing e.g. chips and glycerol.

The vertical uncertainty bars show the standard deviations s_E and $s_\lambda/2$ defined in Eq. (8.10), while the horizontal uncertainty bars show the estimated experimental uncertainty $\Delta U_{\rm pp} \approx 0.04$ V on $U_{\rm pp}$. Notice that the vertical uncertainty increases with increasing $U_{\rm pp}$ leading to lower frame-resolution as the beads move faster.

In Fig. 8.5 (b,c) are shown the measured half-wavelengths $\langle \lambda(U_{\rm pp}^{(j)}) \rangle_N/2$. The experimental half-wavelength is close to the expected width of the channel $w = 0.377$ mm and the majority of the data points are within the interval of uncertainty $\lambda = \bar{\lambda} \pm \Delta x$.

Perturbation parameter and magnitude of first-order fields

From the quantitative measurements of the acoustic energy density, we can determine the first-order fields and the implicit perturbation parameter. We consider the $U_{\rm pp}$-sweep for the chip with $\alpha = 1$, where we have that the acoustic energy density is $E_{\rm ac} \approx 50$ J/m^3 for $U_{\rm pp} = 2$ V. We use the 1D energy expression in Eq. (2.39) to estimate the magnitude $p_{\rm A}$ of the corresponding first-order pressure field in the water-filled channel

$$p_{\rm A} = 2\sqrt{\rho_{\rm wa} c_{\rm wa}^2 E_{\rm ac}} \approx 7 \times 10^5 \text{ Pa}, \tag{8.14}$$

Table 8.3: Extracted values of the acoustic energy density $\langle E_{\rm ac} \rangle_N$ and the half-wavelength $\langle \lambda \rangle_N/2$ as function of driving voltage $U_{\rm pp}$ across the piezo transducer at driving frequency $f = 1.9976$ MHz. s_E and $s_\lambda/2$ are the standard deviations of the acoustic energy density and the half-wavelength, respectively. The data is plotted in Fig. 8.5.

$U_{\rm pp}$ [V]	$\langle E_{\rm ac} \rangle_N$ [J/m^3]	s_E [J/m^3]	$\langle \lambda \rangle_N/2$ [μm]	$s_\lambda/2$ [μm]
0.44	0.65	0.06	383.45	17.82
0.60	4.00	0.67	387.97	20.52
0.80	7.30	0.67	373.96	7.62
0.80	8.17	1.33	375.10	20.15
1.00	15.24	2.61	380.97	5.39
1.04	12.23	3.60	380.86	12.00
1.28	22.61	3.27	397.14	21.30
1.32	17.81	3.01	378.76	10.29
1.60	32.16	6.00	382.57	9.29
1.88	45.30	6.00	377.07	17.06

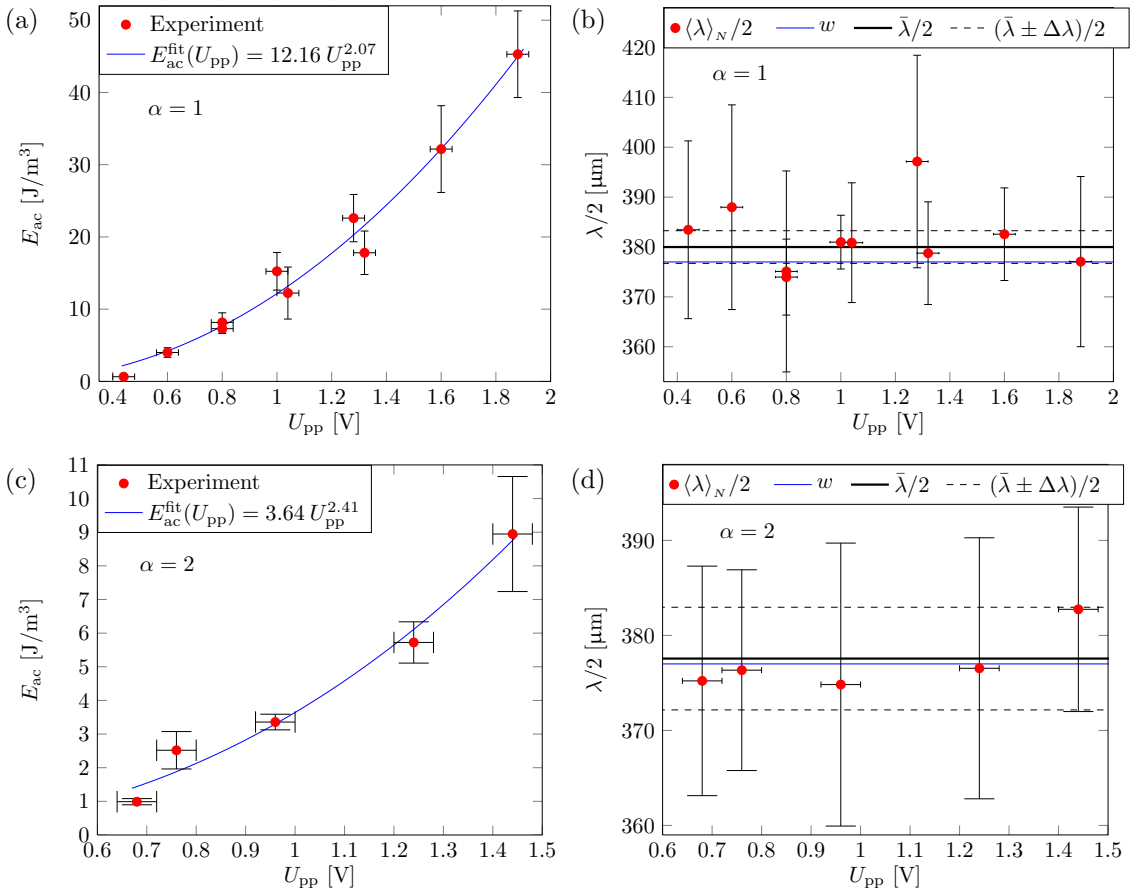

Figure 8.5: Experimentally measured acoustic energy density E_{ac} and half-wavelength $\lambda/2$ versus driving voltage U_{pp} for the chip with $\alpha = 1$ (a,b) and for the chip with $\alpha = 2$ (c,d). The applied piezo frequency is $f = 1.9976$ MHz. The vertical uncertainty bars show the standard deviations s_E and $s_\lambda/2$ defined in Eq. (8.10), while the horizontal uncertainty bars show the experimental uncertainty $\Delta U_{pp} \approx 0.04$ V on U_{pp}. (a,c) Plot of the experimentally measured $\langle E_{ac}(U_{pp}^{(j)})\rangle_N$ (red circles) with its corresponding uncertainties (thin black lines). The data are fitted well with the fitting function $E_{ac}^{fit}(U_{pp})$ (blue curve) Eq. (8.13). For $\alpha = 1$ the fitting parameters are $(a_1, a_2) = (12.13, 2.09)$, whereas for $\alpha = 2$ the fitting parameters are $(a_1, a_2) = (3.64, 2.4)$. The fit is poor for $\alpha = 2$ due to the few experimental points, but it is still clear that the acoustic energy density is approximately a factor of 3 lower for $\alpha = 2$ than for $\alpha = 1$. (b,d) Plot of the experimentally measured $\langle\lambda(U_{pp}^{(j)})\rangle_N/2$ (red circles) with its corresponding uncertainties (thin black lines). In addition is plotted the weighted mean average $\bar{\lambda}$ (thick black line), the channel width $w = 377$ µm (thin blue line) and the uncertainty interval $(\bar{\lambda} \pm \Delta\lambda)/2$ (dashed lines). The plotted data is listed in Table 8.3.

for which the implicit perturbation parameter $\alpha_{per} = p_A/p_0 \approx 3 \times 10^{-4}$ if we assume that $p_0 \approx 2.6 \times 10^9$ Pa as stated in Chap. 2. For the magnitude ρ_A of the first-order density

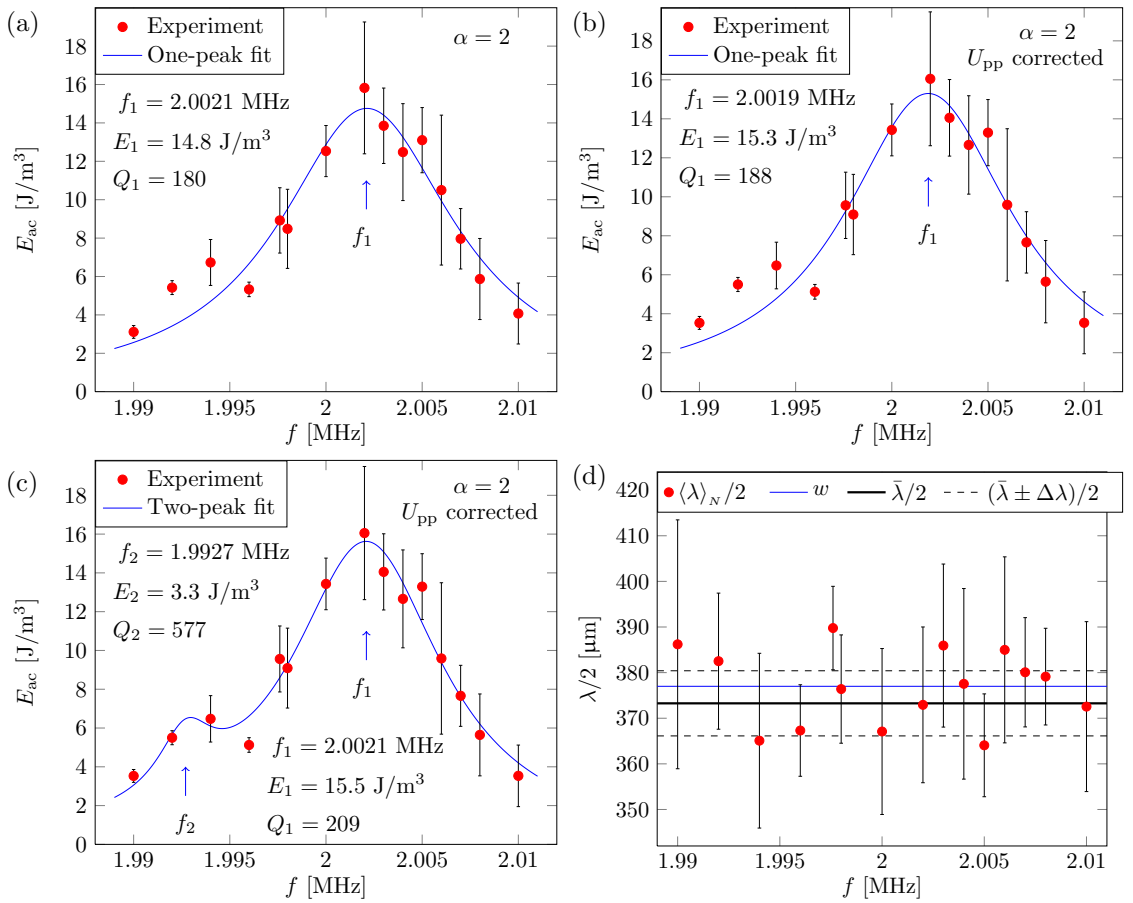

Figure 8.6: Experimentally extracted acoustic energy density E_{ac} and half-wavelength λ versus applied piezo frequency f. The chip has $\alpha = 2$. (a,b,c) Plot of the measured $\langle E_{ac}(f^{(j)})\rangle_N$. The uncertainty bars show the standard deviation s_E defined in Eq. (8.10) (a,b) Fitting of the data points to the one-peak Lorentzian fit $E_{ac}^{fit1}(f)$ in Eq. (8.16). (b) The data points are corrected for variations in U_{pp} resulting in a slightly better fit. (c) The data points are fitted to the two-peak Lorentzian fit $E_{ac}^{fit2}(f)$ in Eq. (8.17). We consequently consider the presence of two resonances in the investigated frequency interval located at frequencies $f_1 = 1.992$ MHz and $f_2 = 2.002$ MHz with Q-values $Q_1 \approx 570$ and $Q_2 \approx 210$. (d) Plot of the experimentally measured $\langle\lambda(f^{(j)})\rangle_N/2$ (red circles) with its corresponding standard deviation s_λ (thin black lines). In addition is plotted the weighted mean average $\bar{\lambda}$ (thick black line), the channel width $w = 377$ µm (thin blue line) and the uncertainty interval $\Delta\bar{\lambda}$ (dashed lines). The plotted data is listed in Table 8.4.

we get

$$\rho_A = \frac{1}{c_{wa}^2} p_A \approx 0.30 \text{ kg m}^{-3}, \tag{8.15}$$

for which we get approximately the same value of the implicit perturbation parameter α_{per}. With this, we conclude that the perturbation approach is well fulfilled for these specific experiments as the perturbation parameter is less than a promille.

Table 8.4: Extracted values of the acoustic energy density $\langle E_{\rm ac}\rangle_N$ and the half-wavelength $\langle\lambda\rangle_N/2$ as function of driving frequency f. s_E and $s_\lambda/2$ are the standard deviations of the acoustic energy density and the half-wavelength, respectively. The data is plotted in Fig. 8.6.

f MHz	$U_{\rm pp}$ [V]	$\langle E_{\rm ac}\rangle_N$ [J/m^3]	s_E [J/m^3]	$\langle\lambda\rangle_N/2$ [µm]	$s_\lambda/2$ [µm]
1.9900	1.40	3.11	0.33	386.21	27.28
1.9920	1.48	5.42	0.36	382.51	14.92
1.9940	1.52	6.73	1.20	365.08	19.15
1.9960	1.52	5.33	0.38	367.31	10.03
1.9976	1.44	8.92	1.70	389.77	9.14
1.9980	1.44	8.48	2.06	376.40	11.87
2.0000	1.44	12.53	1.33	367.09	18.19
2.0020	1.48	15.82	3.43	372.93	17.07
2.0030	1.48	13.85	1.96	385.93	17.87
2.0040	1.48	12.48	2.52	377.54	20.89
2.0050	1.48	13.10	1.70	364.07	11.27
2.0060	1.56	10.50	3.90	384.99	20.39
2.0070	1.52	7.96	1.57	380.08	11.98
2.0080	1.52	5.87	2.11	379.12	10.60
2.0100	1.60	4.07	1.59	372.55	18.62

8.4.4 Acoustic energy density versus driving frequency

In this section we resolve the acoustic energy density $E_{\rm ac}$ as a function of the applied frequency f across the piezo transducer. The experiment is carried out using the chip having $\alpha = 2$. The driving frequency is varied between 1.9900 MHz and 2.0100 MHz, while the applied peak-to-peak voltage tentatively is kept constant, but varied between 1.44 V and 1.60 V. We later use the dependency of $E_{\rm ac}$ on $U_{\rm pp}$ to correct all the measured values of $\langle E_{\rm ac}\rangle_N$ to correspond to the same average driving voltage $U_{\rm pp} = 1.48$ V. The values of $\langle E_{\rm ac}\rangle_N$, $\langle\lambda\rangle_N/2$, s_E and $s_\lambda/2$ are listed in Table 8.4.

The measured $\left\langle E_{\rm ac}\big(f^{(j)}\big)\right\rangle_N$ are now fitted to a Lorentzian shape line as expected from Eq. (4.13). In the following we utilize two fitting functions; (i) a one-peak Lorentzian fit

$$E_{\rm ac}^{\rm fit1}(f) = \frac{E_1}{\left[\frac{2Q_1}{f_1}(f-f_1)\right]^2 + 1}, \tag{8.16}$$

which is fitted by the three unknown variables E_1, f_1 and Q_1 and (ii) a two-peak Lorentzian fit

$$E_{\rm ac}^{\rm fit2}(f) = \frac{E_1}{\left[\frac{2Q_1}{f_1}(f-f_1)\right]^2 + 1} + \frac{E_2}{\left[\frac{2Q_2}{f_2}(f-f_2)\right]^2 + 1}, \tag{8.17}$$

where the additional three fitting variables E_2, f_2 and Q_2 are introduced.

In Fig. 8.6 are shown the results from the frequency sweep. (a) and (b) show fitting to experimental data by the one-peak Lorentzian fit $E_{\rm ac}^{\rm fit1}(f)$. The plot in (b) has been corrected relatively for its variations in peak-to-peak voltage $U_{\rm pp}$, whereas the plot in (a) has

not. It is seen that the correction makes the fitting slightly better. Though the correction, data points having small uncertainties around $f = 1.992$ MHz are off the fit. In (c) the experimental data are corrected for variations in U_{pp} and the data are now fitted by the two-peak Lorentzian fit $E_{\mathrm{ac}}^{\mathrm{fit2}}(f)$ meaning that we consider the presence of two resonance frequencies. The large peak around $f_1 = 2.002$ MHz fits much better, but the smaller peak around $f_2 = 1.992$ MHz is poorly fitted due to the low number of data points. The Q-values are fitted to be $Q_2 \approx 570$ and $Q_1 \approx 210$. Using the definition of $Q_i = f_i/\Delta f_i$ the full widths at half maximum are $\Delta f_1 \approx 9.6$ kHz and $\Delta f_2 \approx 3.5$ kHz.

The frequency shift Δf between the two resonances is $\Delta f = \left|f_1 - f_2\right| \approx 10$ kHz. As the experiments show continuous focusing in the entire frequency range we assume that the two resonance modes are both of antisymmetric type. Additionally we know from Chap. 5 that the acoustic energy densities for symmetric resonance modes are significantly lower than those for antisymmetric resonance modes, thus leading to antisymmetric resonance peaks dominating the frequency spectrum. A reasonable assumption is that f_2 has n_x axial half-wavelengths along l, while f_1 has n_x+1. In Fig. 8.7(a) are seen three neighboring axial modes calculated in the non-shear simple pressure wave 2D model used in Chap. 5. The modes are calculated based on the geometric parameters in Table 8.1 and the longitudinal sound velocities for water and silicon stated in Table 2.1. The frequency shifts are around 12 kHz, which are close to Δf. In Fig. 8.7(b) are seen three modes calculated in the non-shear 3D translational invariant model used in Chap. 5. The results for this model are listed in Table 8.5 for $n_x \in [1\ ;\ 21]$. As discussed previously there is a discrepancy between the two models. For this model the internal frequency shifts between the axial modes are 40 to 45 for the same number of axial half-wavelengths as in (a). Based on the results from the two models, the size of Δf seems reasonably enough to state that the resonance modes at f_1 and f_2 differ by a single half-wavelength in the axial direction.

As observed in Fig. 8.7(a) the resonance peak at f_2 has a lower acoustic energy density than the resonance peak at f_2. A reasonably explanation may be found due to the fact that the axial modes shifts along x as a new half-wavelength is contributed.

8.5 Concluding remarks

We have measured the acoustic energy density and Q-values of the ultrasound resonances in α-chips. We have shown as expected that the acoustic energy density scales with the applied piezo voltage to the power of two. Furthermore, we obtain that the acoustic energy density versus driving frequency are fitted well to Lorentzian shape lines. From these we can obtain the resonance frequency and the corresponding Q-value for the resonance. By the acoustic energy density, we also know the magnitude of all the first-order fields. These quantitative measurements are the first of their kind within the use of ultrasound waves in microfluidic, and thus the results will be sent for publishing in a peer-reviewed journal paper.

Though the determination of useful results, the experiments can be improved substantially by using particle image velocimetry (PIV) making use of a high speed camera. PIV

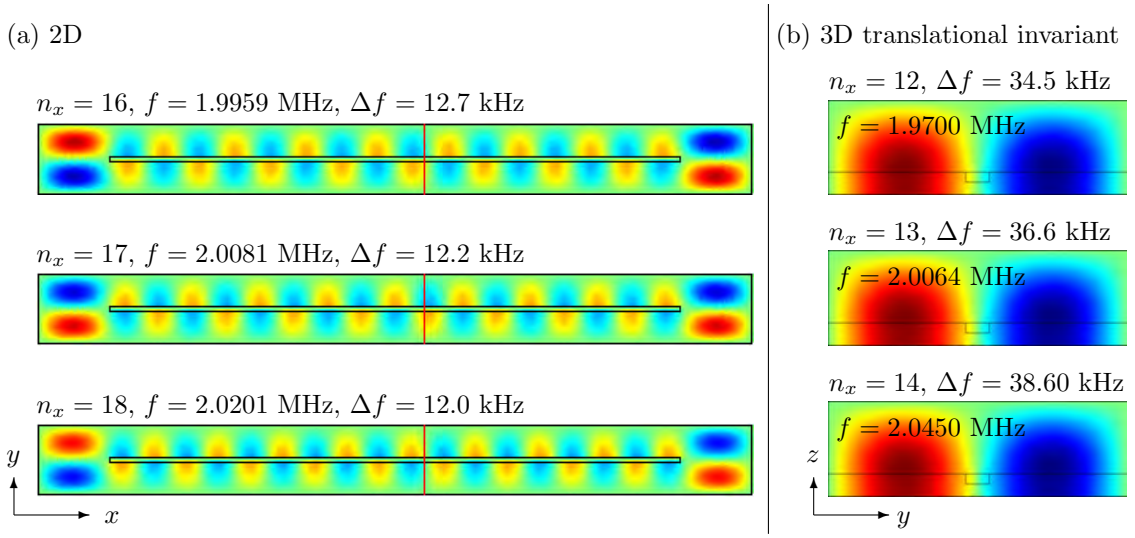

Figure 8.7: Model of Δf between neighboring resonance modes for a chip of $\alpha = 2$. The modes are calculated based on the geometric parameters in Table 8.1 and the longitudinal sound velocities for water and silicon stated in Table 2.1. (a) Non-shear 2D model. (b) Non-shear 3D translational invariant model. The corresponding results are listed in Table 8.5.

Table 8.5: Model of shift in resonance frequencies $\Delta f = f_{n_x} - f_{n_x-1}$ as a function of axial half-wavelengths n_x for a chip of $\alpha = 2$. The model is a 3D translational invariant non-shear model introduced in Chap. 5. The calculations are done using the geometric parameters listed in Table 8.1 and the longitudinal sound velocities given in Table 2.1. Three of the modes are shown in Fig. 8.7(b).

n_x	f_{n_x} [MHz]	Δf [kHz]	n_x	f_{n_x} [MHz]	Δf [kHz]	n_x	f_{n_x} [MHz]	Δf [kHz]
1	1.7419	0.00	8	1.8465	24.26	15	2.0854	40.41
2	1.7470	5.15	9	1.8735	27.04	16	2.1275	42.05
3	1.7556	8.54	10	1.9032	29.67	17	2.1710	43.51
4	1.7674	11.88	11	1.9353	32.20	18	2.2158	44.78
5	1.7826	15.14	12	1.9700	34.47	19	2.2612	45.84
6	1.8009	18.26	13	2.0064	36.62	20	2.3083	46.67
7	1.8222	21.34	14	2.0450	38.60	21	2.3083	47.23

will allow a higher accuracy on measuring the acoustic energy and it will allow for the possibility to identify the resonance patterns, which have not been possible in the current setup. A combination of PIV and the point-actuation device in Fig. 4.2 is promising for recording energy versus frequency spectra suitable for direct quantitative comparison to theory.

Chapter 9

Conclusion

In this thesis we have described the basic theory for a simple pressure wave model for acoustic resonances in microsystems where shear waves are neglected. Throughout the thesis, the simple pressure wave model is used to investigate acoustic resonances in full chip models.

We have investigated a three-dimensional pseudo-realistic full-resonator model of a point-actuation system, which has led to the fabrication of a point-actuation system in the group of Laurell. This device will play a major role in future work to compare theory and experiments.

We have theoretical and numerical analyzed the widely used transverse half-wavelength picture and shown that, although not entirely correct, this picture is accurate enough to be useful. Furthermore, we have shown that it is crucial to take the entire geometry of the chip into account and match the dimensions of the surrounding silicon to those of the water channel. The analyses are based on 1D, 2D and 3D models. From the modeling of the three-dimensional chip structures, we suggest to use translational invariant experimental chips as these are easier modeled theoretically, and since they avoid the existence of areas without acoustic importance for the resonances in the water-filled channel. The analysis of the transverse half-wavelength picture is numerically applied for the simulation of two applications; (*i*) a many-channel separation chip to achieve larger throughput, and (*ii*) a three-channel *in situ* calibration chip.

Moreover, 2D and 3D theoretical and numerical approaches are used to investigate the fundamental conditions for establishing acoustic waveguides in acoustofluidic systems.

Additional to the theoretically modeling work, the author has carried out experiments in the laboratory of the group of Laurell. The electrical impedances of the utilized piezo transducer was investigated when being subject to different acoustic loads, and the sedimentation times for polystyrene microbeads were calibrated. The acoustic energy density and Q-values were measured by tracking of individual polystyrene particles undergoing acoustophoresis in straight water-filled channels in silicon/pyrex microchips. The acoustic energy densities were obtained by fitting the microbead tracks to a theoretical curve predicted by the balance between the acoustic pressure force and the Stokes drag force. It was found as expected that the acoustic energy density scales with the applied piezo

voltage to the power of two. Furthermore, it was shown that the acoustic energy densities as function of applied ultrasound frequency behave as Lorentzian line shapes, from which the resonance frequencies and resonance Q-values can be obtained. For these quantitative measurements, it is found that the theoretical perturbation approach is valid, as the implicit perturbation parameter is less than a promille.

During the experimental work a discrepancy between the three-dimensional simple pressure wave model and the experiments was found. The discrepancy is assumed to be due to shear waves in the solids being neglected. Thus, we have presented the basic theory for elastic waves in isotropic solids, which creates the basis for future calculations of the acoustic resonances in the investigated microchip systems.

9.1 Outlook

Although we have treated many aspects of the ultrasound resonances in microchips, plenty of work are still to be done. The theoretical acoustofluidic work will continue in the group of Bruus in the PhD-project "Acoustofluidics: ultrasound manipulation of biomolecules and cells in microfluidic systems" with the author of this thesis as the PhD student.

As concluded, the simple pressure wave model has proven to be useful, but future modeling work needs to take into account the theory of elastic waves in solids in order to account for the discrepancy in frequency between the simple pressure wave model and experiments.

Also, the experimental measurements of the acoustic energy density has to be extended with the objective to measure acoustic frequency spectra, which will make a solid basis for comparison between theory and experiments. The experiments can be obtained using the point-actuation device fabricated in the group of Laurell as it eliminates the loss of acoustic energy due to transmission of waves and because the use of a point transducer limits the transducer boundary, which is still a weak point in the theoretical models.

As just mentioned, effective modeling of the piezo transducer is still a weak point when investigating the acoustic resonances. Here more work has to be done both theoretical as well as experimental. An interesting experiment is to directly measure the displacement amplitude of the piezo transducer by e.g. laser techniques.

Moreover, a promising topic is the creation of acoustic waveguides in the microchips, but more work is needed as we only state the basics in this thesis. The first objectives is to carry out more thorough investigations of the waveguide conditions and to verify these by numerically modeling taking into account the elastic wave theory in solids. Finally, the investigations must be verified experimentally.

Also the influence of temperature on the acoustic resonances is of major importance, and here both theoretical as well as experimental investigations has to be done and mutually verified.

More generally for the acoustofluidic theory, we need to fully understand the phenomenon of acoustic streaming and the secondary Bjerknes forces, as they are shown to be non-negligible for particles of radii < 1 μm and radii > 20 μm, respectively [43].

Appendix A

Peer-reviewed conference proceeding published at 157th meeting of the Acoustical Society of America

R. Barnkob and H. Bruus

Proceedings of Meetings on Acoustics

Volume 6, 2009 http://asa.aip.org

157th Meeting
Acoustical Society of America
Portland, Oregon
18 - 22 May 2009
Session 2pBB: Biomedical Ultrasound/Bioresponse to Vibration

2pBB2. Acoustofluidics: theory and simulation of radiation forces at ultrasound resonances in microfluidic devices

Rune Barnkob and Henrik Bruus*

***Corresponding author's address: Department of Micro- and Nanotechnology, Technical University of Denmark, DTU Nanotech, Building 345 east, Kongens Lyngby, 2800, -, Denmark, Henrik.Bruus@nanotech.dtu.dk**

Theoretical analysis is combined with numerical simulations to optimize designs and functionalities of acoustofluidic devices, i.e. microfluidic devices in which ultrasound waves are used to anipulate biological particles. The resonance frequencies and corresponding modes of the acoustic fields are calculated for various specific geometries of glass/silicon chips containing water-filled microchannels. A special emphasis is put on taking the surrounding glass/silicon material into account, thus going beyond the traditional transverse half-wavelength picture. For the resonance frequencies, where the largest possible acoustic powers are obtained in the microfluidic system, the time-averaged acoustic radiation force on single particles is determined. Schemes for in situ calibration of this force are presented and discussed.

Published by the Acoustical Society of America through the American Institute of Physics

 [DOI: 10.1121/1.3186746]
Received 27 May 2009; published 6 Jul 2009

1. INTRODUCTION

The studies of acoustic radiation forces on particles have a long history. The analysis of incompressible particles in acoustic fields dates back to the work in 1934 by King [1], while the forces on compressible particles were calculated in 1955 by Yosioka and Kawasima [2]. Their work was admirably summarized in 1962 in a short paper by Gorkov [3]. The use of ultrasound standing waves for particle manipulation and separation has received renewed interest in the past decade since its application in the emerging field microfluidics [4]–[20].

In these recent papers, standing ultrasound resonances have been established in flat microfluidic channels of height $h \approx 150\ \mu$m, width $w \approx 400\ \mu$m, and length $\ell \approx 4$ cm embedded in a silicon/glass chip with an area several square centimeter large and a height $H \approx 1$ mm. A wide spread assumption is that due to the large acoustic impedance ratio of the order of 13 between silicon/glass and water, the leading resonance at frequency f is given by the half-wavelength condition $\lambda/2 = c_{\mathrm{wa}}/(2f) = w$. This leads to $f \approx 2$ MHz. This is of course not exactly true. By taking the whole silicon/glass/water resonator into account, we study theoretically the deviations from this idealization to be expected in actual devices.

Another particular problem with the application of standing ultrasound waves in microfludic systems concerns the calibration of the acoustic radiation force. Acoustic power sent from the actuator to the microfluidic system suffers losses due to heating in the system and acoustic radiation to the surroundings. These losses are hard to measure, and at the same time it is difficult to mount pressure sensors inside the microfluidic system for direct determination of the acoustic power actually present. We present a possible *in situ* calibration of the acoustic radiation force from a standing ultrasound wave on suspended spherical particles in a microfluidic channel. The method relies on determining the critical flow velocity above which the particles cease to be trapped by the ultra sound forces.

2. BACKGROUND THEORY

Linear acoustics and acoustic radiation forces are treated in many textbooks. Basic theory can be found in Lighthill [21] and theoretical aspect of acoustics in microfluidics, acoustofluidics, can be found in Bruus [22]. In this work we rely on the formulation of Gorkov [3].

2.1. Governing equations and boundary conditions

We consider a silicon/glass chip containing a microchannel filled with an aqueous solution of particles. A piezo actuator is glued to the chip, such that when applying an AC voltage at MHz frequency, the piezo element vibrates and induces a time-harmonic ultrasound pressure field $p_1 \exp(-\mathrm{i}\,\omega t)$, where $\omega = 2\pi f$ is the angular frequency and f the frequency. Here, we use the complex representation of the harmonic time dependence. In the following the time-harmonic factor is implicitly assumed, and we just write the amplitude p_1. Likewise for the velocity field $\boldsymbol{v}_1$ of the carrier liquid.

Before the onset of the external ultrasound field the solution is in a quiescent state at constant uniform pressure p_{wa} and zero velocity. The viscosity of the carrier liquid has a negligible influence on the acoustic radiation forces. Consequently, to a good approximation, the pressure field p_1 and velocity field $\boldsymbol{v}_1$ inside the chip and the microchannel are governed by simple linear acoustics of inviscid fluids, i.e. the Helmholtz wave equation for the pressure and potential flow for the velocity,

$$\nabla^2 p_1 = -\frac{\omega^2}{c_{\mathrm{wa}}^2}\, p_1, \tag{1a}$$

$$\boldsymbol{v}_1 = -\frac{\mathrm{i}}{\omega\rho_{\mathrm{wa}}}\boldsymbol{\nabla} p_1. \tag{1b}$$

Here, c_{wa} and ρ_{wa} is the speed of sound and the density of the carrier liquid, respectively. Note that in this simple model we neglect the shear waves in the solids.

At a boundary characterized by the surface normal vector $\boldsymbol{n}$, we employ three different boundary conditions in this work: the hard wall (zero velocity) condition, the soft wall (zero pressure) condition, and the continuity condition for pressure and velocity across interior boundaries,

$$\boldsymbol{n}\cdot\boldsymbol{\nabla} p_1 = 0, \qquad \text{(hard wall)}, \tag{2a}$$

$$p_1 = 0, \qquad \text{(soft wall)}, \tag{2b}$$

$$\frac{1}{\rho_a}\boldsymbol{n}\cdot\boldsymbol{\nabla} p_1^{(a)} = \frac{1}{\rho_b}\boldsymbol{n}\cdot\boldsymbol{\nabla} p_1^{(b)}, \quad \text{and} \quad p_1^{(a)} = p_1^{(b)}, \quad \text{(continuity)}. \tag{2c}$$

TABLE 1. Physical parameters used in the model for polystyrene beads in water inside a silicon chip.

Speed of sound, water	c_{wa}	1483 m s^{-1}	Density, water	ρ_{wa}	998 kg m^{-3}
Speed of sound, silicon	c_{si}	8490 m s^{-1}	Density, silicon	ρ_{si}	2331 kg m^{-3}
Speed of sound, pyrex	c_{py}	5647 m s^{-1}	Density, pyrex	ρ_{ps}	2230 kg m^{-3}
Speed of sound, polystyrene	c_{ps}	1700 m s^{-1}	Density, polystyrene	ρ_{ps}	1050 kg m^{-3}
Speed of sound ratio $c_{\mathrm{ps}}/c_{\mathrm{wa}}$	β_{ps}	1.15	Density ratio $\rho_{\mathrm{ps}}/\rho_{\mathrm{wa}}$	γ_{ps}	1.05
Compressibility factor, polystyrene	f_1	0.276	Density factor, polystyrene	f_2	0.034

2.2. Acoustic resonances

The acoustically soft water inside the channel surrounded by the acoustically hard silicon/glass chip forms an acoustic cavity. This implies that acoustic resonances occur for certain specific frequencies ω_j, $j = 1,2,3,\ldots$. An acoustic resonance at frequency ω_j is a state where the average acoustic energy density inside the cavity is several orders of magnitude larger than at other frequencies $\omega \neq \omega_j$. By tuning the applied frequency to one of these resonance frequencies, the acoustic forces become so strong that they in a reliable way can be used to manipulate particles suspended in the carrier liquid.

The exact values of the resonance frequencies ω_j depend on the geometry of the acoustic cavity and of the material parameters of the liquid in the cavity as well as the surrounding material. Specifically, the relevant material parameters are the speed of sound c_{wa} and density ρ_{wa} of the water and likewise the speed of sound c_{si} and density ρ_{si} of the silicon chip, see Table 1. In the general case, the resonance frequencies can only be calculated using numerical methods, however, in few cases they may be found analytically.

For a rectangular channel of length l, width w, and height h, surrounded by an acoustically infinitely hard material, the resonance frequencies may be found analytically. This case approximates our experimental system reasonably well. Neglecting the inlet and outlet, our microchannel is indeed rectangular. Moreover, since the parameters listed in Table 1 yields an acoustic impedance ratio $(\rho_{\mathrm{si}}c_{\mathrm{si}})/(\rho_{\mathrm{wa}}c_{\mathrm{wa}}) = 13.4$ much larger than unity, the silicon surrounding our rectangular water channel can to a good approximation be treated as an infinitely hard material. In that case the normal velocity on all walls is zero, which according to Eq. (1b) is equivalent to Neumann boundary conditions $\boldsymbol{n}\cdot\boldsymbol{\nabla} p_1 = 0$ for the pressure. It is easily verified that with this boundary condition the pressure p_1 solving Eq. (1a) for a rectangular box placed along the coordinate axes with its opposite corners at $(0,0,0)$ and (l,w,h) is

$$p_1(x,y,z) = p_{\mathrm{a}}\cos(k_x x)\cos(k_y y)\cos(k_z z), \quad \text{with} \quad k_j = n_j\frac{\pi}{L_j}, \quad n_j = 0,1,2,3,\ldots \tag{3}$$

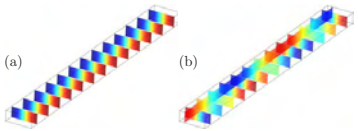

FIGURE 1. Color plot (red positive, blue negative) of the pressure field p_1 at resonance in a water-filled microchannel of length $l = 5$ mm along x, width $w = 0.5$ mm along y, and height $h = 0.2$ mm along z, surrounded by an infinitely hard acoustic material, see Eq. (3). (a) Resonance $(n_x,n_y,n_z) = (0,1,0)$ with $f_{0,1,0} = 1.48$ MHz, and (b) $(n_x,n_y,n_z) = (3,1,0)$ with $f_{3,1,0} = 1.55$ MHz.

where p_a is the pressure amplitude, and where $L_x = l$, $L_y = w$, and $L_z = h$. The corresponding three-index resonance frequencies $f_{n_x,n_y,n_z} = \omega_{n_x,n_y,n_z}/(2\pi)$ are given by

$$f_{n_x,n_y,n_z} = \frac{c_{wa}}{2}\sqrt{\frac{n_x^2}{l^2}+\frac{n_y^2}{w^2}+\frac{n_z^2}{h^2}}, \quad \text{with} \quad n_x,n_y,n_z = 1,2,3,4,\ldots. \tag{4}$$

Two examples of resonant standing ultrasound waves are shown in Fig. 1.

2.3. The acoustic radiation force

Given the acoustic pressure field p_1 and velocity field $\boldsymbol{v}_1$ it is possible to calculate the acoustic radiation force on a particle with volume V and linear dimension $V^{\frac{1}{3}}$ much smaller than the acoustic wavelength λ. Both for biological cells and for micrometric tracer particles we are in this limit. The material parameters, with subscripts "wa" for the water and "p" for the particle, enter as the speed of sound ratio β and the density ratio γ,

$$\beta = \frac{c_p}{c_{wa}}, \qquad \gamma = \frac{\rho_p}{\rho_{wa}}, \tag{5}$$

which appear in the pre-factors f_1 and f_2 as

$$f_1 = 1 - \frac{1}{\gamma\beta^2}, \qquad f_2 = \frac{2\gamma-2}{2\gamma+1}. \tag{6}$$

The general expression for the time-averaged acoustic radiation force $\boldsymbol{F}_{ac}$ is given by Gorkov [3],

$$\boldsymbol{F}_{ac} = -V\boldsymbol{\nabla}\left[\frac{f_1}{2\rho_{wa}c_{wa}^2}\langle p_1^2\rangle - \frac{3f_2\rho_{wa}}{4}\langle|\boldsymbol{v}_1|^2\rangle\right] = -\frac{V}{4\rho_{wa}c_{wa}^2}\boldsymbol{\nabla}\left[2f_1\langle p_1^2\rangle - 3f_2\frac{1}{k^2}\langle|\boldsymbol{\nabla}p_1|^2\rangle\right], \tag{7}$$

where the latter form is obtained by use of Eq. (1b) and $k^2 = k_x^2 + k_y^2 + k_z^2$.

3. ANALYSIS OF TRANSVERSE HALF-WAVELENGTH MODES

For experimental applications it is desirable to work with half-wavelength waves of odd symmetry in the transverse y-direction of the water-filled channel, i.e. $w = \lambda/2$ and thus a resonance frequency $f_{0,1,0} \approx c_{wa}/(2w)$. For such modes the acoustic radiation force focuses hard particles at the pressure node in the vertical xz-plane along the center line of the channel, see Fig. 1(a). The question now arises how the width W of surrounding silicon chip affects this simple estimate for $f_{0,1,0}$.

3.1. Analysis of 1D models

In Fig. 2 is sketched a 1D model for the transverse y-direction, where for simplicity we introduce the lengths $a \equiv w/2$ and $b \equiv (W-w)/2$ for half the width of the channel and the width of the silicon chip from the channel to the edge, respectively. The model is symmetric around the center of the channel thus leading to two classes of solutions for the pressure, namely even and odd modes.

Using the proper symmetry boundary condition at $y = -a$, either Eq. (2a) for even or Eq. (2b) for odd modes, and the soft boundary condition Eq. (2b) at $y = b$, results in cosine (even) or sine (odd) solutions for the pressure waves,

$$p_{wa}(y) = A_{wa}\cos[k_{wa}(y+a)], \quad \text{(even)}, \tag{8a}$$
$$p_{wa}(y) = A_{wa}\sin[k_{wa}(y+a)], \quad \text{(odd)}, \tag{8b}$$
$$p_{si}(y) = A_{si}\sin[k_{si}(y-b)], \tag{8c}$$

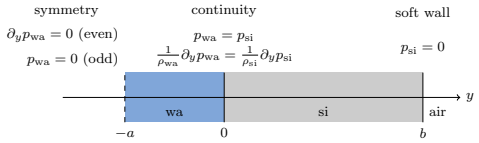

FIGURE 2. Sketch of the 1D model containing half the water-filled channel (wa) and the silicon chip (si). The model includes three boundaries; a symmetric point in the center of the channel ($y = -a$), an interface between channel and chip ($y = 0$), and the outer boundary of the silicon chip ($y = b$). Notice that the boundary condition at the symmetry point gives either even or odd pressure-modes across the channel.

where A_{wa} and A_{si} are pressure amplitudes. Employing the continuity condition Eq. (2c) at $y = 0$ and utilizing that $k_{si} = k_{wa}c_{wa}/c_{si}$, results in transcendental equations for even and odd pressure eigenmodes

$$\cot(\theta) = z\tan(\alpha\theta), \quad \text{(even)}, \qquad \text{and} \qquad \cot(\theta) = -\frac{1}{z}\cot(\alpha\theta), \quad \text{(odd)}, \tag{9}$$

where $\theta = k_{wa}a$ is the dimensionless wavenumber, $z = (\rho_{si}c_{si})/(\rho_{wa}c_{wa}) \approx 13.4$ is the acoustic impedance ratio, and α is the aspect ratio parameter given by

$$\alpha \equiv \frac{c_{wa}}{c_{si}}\frac{b}{a} = \frac{\text{number of wavelengths in the silicon chip}}{\text{number of wavelengths in the water channel}}. \tag{10}$$

From Eq. (9) it is now possible for a given value of α to determine which value of $k_{wa} = 2\pi/\lambda_{wa}$ that most accurately approximates a perfect half-wavelength mode $\lambda_{wa}^* = 4a$ in the water-filled channel. Expressing the actual wavelength λ_{wa} as a function of the ideal wavelength λ_{wa}^* and a relative shift δ in the wavelength, we get

$$\lambda_{wa} = \lambda_{wa}^*(1+\delta). \tag{11}$$

For a perfect half-wavelength mode we have $\theta = \pi/2$, and the relative shift in wavelength is zero, $\delta = 0$.

In Fig. 3 is shown a graphic representation of the even and odd pressure eigenmode solutions for $\alpha = 1$ and 2. The perfect half-wavelength solution, $\theta/\pi = 0.5$ is odd in the case of $\alpha = 1$ (marked A) and even for $\alpha = 2$ (marked B). In the latter case two odd solutions (marked C_- and C_+) are nearly half-wavelength modes with values of θ/π close to 0.5. The actual pressure modes $p(y)$ for the four cases A, B, C_+, and C_- are shown in Fig. 4.

A quantitative measure of the quality of a given eigenmode can be obtained from the expression for the acoustic energy density $\mathscr{E}$,

$$\mathscr{E}(\boldsymbol{r},f) = \frac{1}{4\rho(\boldsymbol{r})}\left[\frac{1}{(2\pi f)^2}|\boldsymbol{\nabla}p_1(\boldsymbol{r})|^2 + \frac{1}{c^2}|p_1(\boldsymbol{r})|^2\right]. \tag{12}$$

The higher the average acoustic energy density $\langle\mathscr{E}_{wa}\rangle$ is in the water-filled channel relative to the maximum acoustic energy density $\mathscr{E}_{si}^{max}$ in the surrounding silicon chip, the better. For the four specific modes A, B, C_+, and C_- shown in Fig. 4 we find numerically that $\langle\mathscr{E}_{wa}\rangle/\mathscr{E}_{si}^{max} = 76.5$, 0.4, 10.6, and 10.6, respectively. Clearly, the perfect anti-symmetric half-wavelength mode in the $\alpha = 1$ chip has the best figure of merit.

3.2. Analysis of 2D models

We now extend our analysis of the half-wavelength modes from 1D to 2D by taking the length direction of the system along the x-axis into account on top of the transverse direction along the y-axis. As shown in Fig. 5, the most prominent change from 1D to 2D is the appearance of oscillations in the axial direction along the x-axis, a feature not possible in 1D. The third dimension can be neglected due to the absence of dynamics in this direction for channels with a height less than half a wavelength [17].

86 Peer-reviewed conference proceeding published at 157th meeting of the Acoustical Society of America

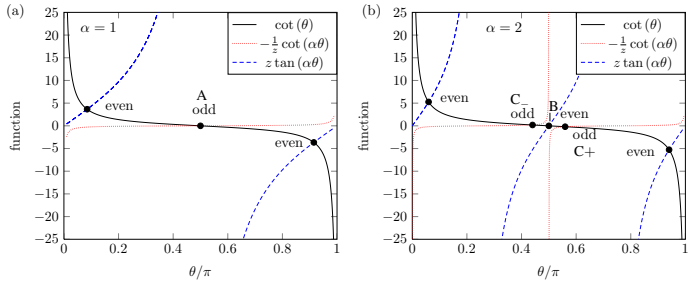

FIGURE 3. Graphic representation of the even and odd pressure eigenmode solutions in the 1D silicon/water model to the transcendental equations given in Eq. (9) for (a) $\alpha = 1$ and (b) $\alpha = 2$. The perfect half-wavelength solution, $\theta/\pi = 0.5$ is odd in the case of $\alpha = 1$ (marked A) and even for $\alpha = 2$ (marked B). In the later case two odd solutions (marked C$_-$ and C$_+$) are nearly half-wavelength modes with values of θ/π close to 0.5.

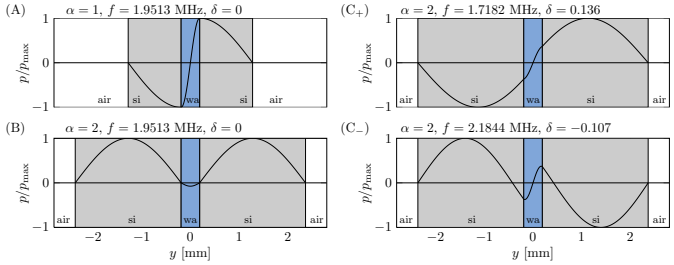

FIGURE 4. Pressure eigenmodes $p(y)$ of the four special cases marked in Fig. 3 for the 1D silicon/water (gray/blue) model given a water channel width of $w = 2a = 0.38$ mm. (A) The perfectly matched silicon chip with $\alpha = 1$ supporting the anti-symmetric half-wavelength pressure mode in the water channel at frequency $f = 1.9513$ MHz. (B) The silicon chip with $\alpha = 2$ also supports a pressure eigenmode at $f = 1.9513$ MHz, however this mode is symmetric. (C$_+$) An anti-symmetric eigenmode in the $\alpha = 2$ chip with a frequency as close as possible, but lower, to the ideal frequency of panel (A). Here $f = 1.7182$ MHz and the wavelength in the water channel is 13.6% too long ($\delta = 0.136$). (C$_-$) An anti-symmetric eigenmode in the $\alpha = 2$ chip with a frequency as close as possible, but higher, to the ideal frequency of panel (A). Here $f = 2.1844$ MHz and the wavelength in the water channel is 10.7% too short ($\delta = -0.107$).

As in 1D we also in 2D study the $\alpha = 1$ and $\alpha = 2$ chips. To enable direct comparison we reuse the 1D widths in 2D for the transverse y-direction. Some of the resulting pressure eigenmodes are shown in Fig. 5. We note how the modes (A), (B), (C$_+$), and (C$_-$) from the 1D case in Fig. 4 also can be identified in the 2D case of Fig. 5. However, due to the extra degree of freedom for oscillations in the axial x-direction, it is now possible even in the "bad" $\alpha = 2$ chip to find eigenmodes (D$_+$ and D$_-$), which are both close to the ideal frequency $f = 1.95$ MHz of the $\alpha = 1$ chip in panel (A) and at the same time possess the wanted odd (one-node) symmetry in the transverse y-direction. The only drawback is the appearance of several nodes in the axial direction. It is found experimentally that pressure modes with

a lower number of axial nodes lead to higher separation efficiencies [18].

As in the 1D case, we can study the quality of the 2D pressure eigenmodes by evaluating the ratio of the acoustic energy density in the water channel relative to that in the silicon chip. The results are listed in Table 2. Again, the perfectly matched A-mode has the best figure of merit, however it is seen that also the new D$_+$ and D$_-$ also perform well. These three modes have high energy density ratios of 39.2, 32.0 and 36.1, respectively, while the other three modes have ratios around 6 or lower.

A natural extension of the model is a many-channel chip, which supports higher flow rates. We reuse the former channel geometries to create a chip with eight parallel channels. Resulting modes for two chips of different values of α are shown in Fig. 6. We note the obvious different in homogeneity in pressure amplitudes from the perfectly matching mode in the $\alpha = 1$ chip to the badly matching mode in the arbitrarily chosen $\alpha = 0.47$ chip. Regarding the energy ratios, the perfectly matching chip mode has an homogeneous average energy density ratio of 39.4, whereas the mode in the non-matching chip has an inhomogeneous energy density with an average ratio of 16.4. The two examples

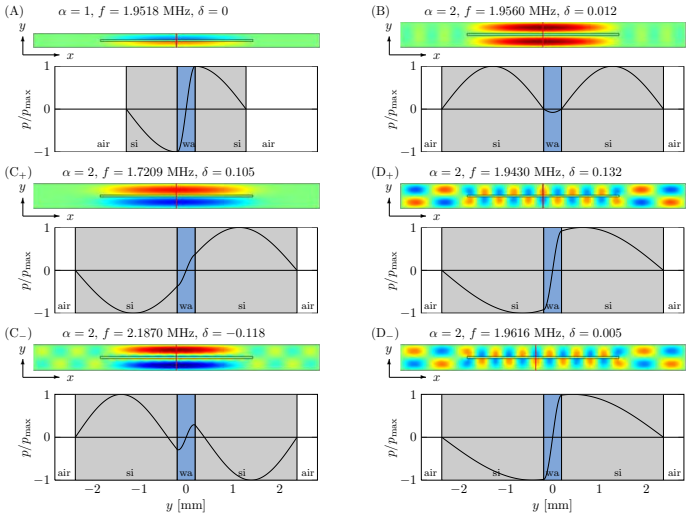

FIGURE 5. 2D COMSOL simulations of six pressure eigenmodes in a water-filled channel (wa/blue) of width $w = 0.38$ mm and length $l = 29.30$ mm. The channel is placed in a silicon chip (si/gray) of width $W = \alpha\,(c_{si}/c_{wa})w$ and length $L = 55.00$ mm. The widths here are as in the 1D system of Fig. 4. For each mode the pressure amplitude is plotted along the indicated red line in the corresponding 2D color plot of the pressure amplitude. (A) $\alpha = 1$, $W = 2.6$ mm: perfectly matching mode at the ideal frequency $f = 1.95$ MHz having odd (one-node) transverse symmetry and even (zero-node) axial symmetry. (B) $\alpha = 2$, $W = 4.7$ mm: matching mode at $f = 1.95$ MHz very near the ideal frequency, but having the un-wanted even (two-node) transverse symmetry and even (zero-node) axial symmetry. (C$_+$) and (C$_-$) $\alpha = 2$, $W = 4.7$ mm: as in Fig. 4 non-matching modes with frequencies far below/above the ideal frequency having the wanted odd (one-node) transverse symmetry and even (zero-node) axial symmetry. (D$_+$) and (D$_-$) $\alpha = 2$, $W = 4.7$ mm: almost matching modes with frequencies near the ideal frequency having the wanted odd (one-node) transverse symmetry, but with many nodes in the axial direction.

TABLE 2. Data for the six 2D pressure eigenmodes shown in Fig. 5. Listed are the value of the aspect parameter α and the symmetries, as well as the resulting frequency f, relative shift in wavelength δ, and energy density ratio obtained by COMSOL simulations.

Mode	α	x-symm.	y-symm.	f [MHz]	δ [%]	$\langle\mathscr{E}_{\mathrm{wa}}\rangle/\mathscr{E}_{\mathrm{si}}^{\max}$
A	1	even	odd	1.9518	0.0	39.2
B	2	even	even	1.9560	1.2	0.2
C_+	2	even	odd	1.7209	13.4	6.3
C_-	2	even	odd	2.1870	−11.7	5.1
D_+	2	even	odd	1.9430	1.4	32.0
D_-	2	odd	odd	1.9616	0.5	36.1

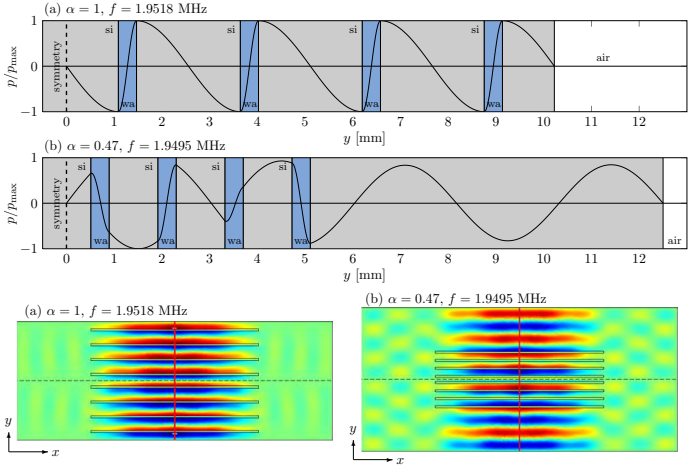

FIGURE 6. 2D COMSOL simulations of silicon chips (si/gray) length $L = 55.00$ mm containing eight parallel water-filled channels (wa/blue) each of width $w = 0.38$ mm and length $l = 29.30$ mm. Two chips are shown; (a) $\alpha = 1$ between channels and to the silicon edge, and (b) $\alpha = 0.47$ between channels and $\alpha = 6.80$ to the silicon edge. For each shown resonance the pressure amplitude is plotted as a surface plot showing the entire chip and as a symmetric cross-sectional plot along the transverse y-direction. For each plot the pressure is normalized to the maximum pressure for that given mode.

presented clearly demonstrate the importance of designing the chip surrounding the water-filled channel properly.

4. IN SITU CALIBRATION OF ACOUSTIC RADIATION FORCES ON PARTICLES

When applying standing ultrasound waves in microfludic systems, it is difficult to measure or calibrate the acoustic radiation force exerted on a particle in solution. Acoustic power sent from the actuator to the microfluidic system suffers losses due to heating in the system and acoustic radiation to the surroundings. These losses are hard to measure,

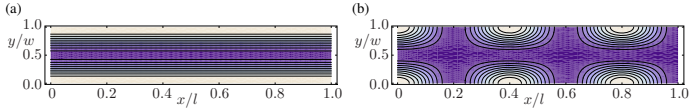

FIGURE 7. (a) Contour plot with 10% contour lines from low (dark) to high (light) of the normalized acoustic potential $U_{\mathrm{ac}}/U_{\mathrm{o}}$ from Eq. (15b) for a polystyrene sphere in water given the ideal 1D pressure field p_1 of Eq. (13a) with $(k_x, k_y) = (0, \pi y/w)$ so that $\theta = 90°$. (b) Similar plot for the 2D pressure field with $(k_x, k_y) = (\pi/(2w), \pi/w)$ so that $\theta \approx 63°$. Further parameter values used in the simulation are given in Table 1.

and at the same time it is difficult to mount pressure sensors inside the microfluidic system for direct determination of the acoustic power actually present. Based on the insight obtained above, regarding the global wave nature of the pressure eigenmodes, we present in the following a possible chip design for *in situ* calibration of the acoustic radiation force from a standing ultrasound wave on suspended spherical particles in a microfluidic channel. The method relies on determining the critical flow velocity above which the particles cease to be trapped by the ultrasound forces.

4.1. The acoustic potential experienced by a particle

According to Eq. (7), the acoustic force acting on a particle in solution can be calculated once the pressure eigenmode p is known. Our previous analysis for straight 2D channels of length l and width w have shown that to a good approximation these eigenmodes are given by simple cosine/sine standing waves in a water channel surrounded by infinitely hard walls. Such an idealized 2D pressure eigenmode is given by

$$p_1(x,y,z) = +p_{\mathrm{a}}\cos(k_x x)\cos(k_y y), \tag{13a}$$

$$\boldsymbol{\nabla} p_1(x,y,z) = -k_x p_{\mathrm{a}}\sin(k_x x)\cos(k_y y)\boldsymbol{e}_x - k_y p_{\mathrm{a}}\cos(k_x x)\sin(k_y y)\boldsymbol{e}_y, \tag{13b}$$

$$\boldsymbol{k} = k_x\boldsymbol{e}_x + k_y\boldsymbol{e}_y. \tag{13c}$$

This standing wave can be interpreted as the result of two counter-propagating waves along the direction $\boldsymbol{k}$, which forms the angle θ with the x-axis,

$$\cos\theta = \frac{k_x}{k}, \quad \sin\theta = \frac{k_y}{k}, \quad k = \sqrt{k_x^2 + k_y^2}. \tag{14}$$

Inserting this in Gorkov's expression Eq. (7), we find the acoustic force as minus the gradient of a potential U_{ac},

$$\boldsymbol{F}_{\mathrm{ac}} = -\boldsymbol{\nabla} U_{\mathrm{ac}}, \tag{15a}$$

where the acoustic potential U_{ac} and its amplitude U_{o} are given by

$$U_{\mathrm{ac}} = U_{\mathrm{o}}\Big[2f_1\cos^2(k_x x)\cos^2(k_y y) - 3f_2\sin^2(k_x x)\cos^2(k_y y)\cos^2\theta - 3f_2\cos^2(k_x x)\sin^2(k_y y)\sin^2\theta\Big], \tag{15b}$$

$$U_{\mathrm{o}} = \frac{p_{\mathrm{a}}^2 V}{8\rho_{\mathrm{wa}}c_{\mathrm{wa}}^2}. \tag{15c}$$

Two numerical examples of the acoustic potential U_{ac} for a polystyrene sphere are shown in Fig. 7.

4.2. Chip design for in situ calibration of the acoustic radiation force

The acoustic radiation force on a suspended particle can be calibrated *in situ* if it is anti-parallel to the Stokes drag force from the flow of the carrier liquid along the x-direction. By gradually increasing the flow velocity v from zero,

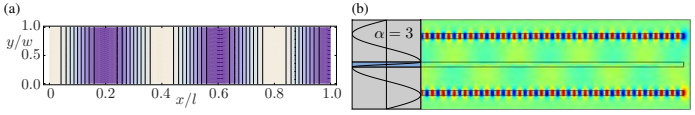

FIGURE 8. (a) Contour plot with 10% contour lines from low (dark) to high (light) of the normalized acoustic potential $U_{\rm ac}^{\rm calib}/U_{\rm o}$ from Eq. (16a) for a polystyrene sphere in water given the pressure field $p_1 = p_a\cos(\pi x/2w)$. The parameter values are given in Table 1, and moreover $k_x = \pi/(2w)$ while $k_y = 0$ so that $\theta = 0$. (b) Color plot of the pressure eigenmode in the triple-channel $\alpha = 3$ chip. A transverse potential, as in panel (a), suitable for *in situ* acoustic force calibration is set up in the two side channels, while the center channel supports a transverse mode of odd symmetry as in Fig. 5(D$_+$). The left insert shows the single-channel $\alpha = 3$ chip. Note the two anti-nodes in the silicon chip (gray) above and below the water-filled channel (blue).

a critical value v^* of v can be determined, above which the acoustic radiation force no longer can trap the particle. At this point $|\boldsymbol{F}_{\rm ac}| \approx 6\pi\eta a v^*$, and the unknown pre-factor $U_{\rm o}$ can be determined. The calibration setup requires that $\boldsymbol{k}$ and $\boldsymbol{e}_x$ are parallel, thus $k_x \neq 0$ while $k_y = 0$. By combining Eqs. (6) and (15) with this form of the wave vector, we obtain the acoustic potential and the associated radiation force for calibration purposes on the form

$$U_{\rm ac}^{\rm calib} = U_{\rm o}\left[2f_1\cos^2(k_x x) - 3f_2\sin^2(k_x x)\right], \tag{16a}$$

$$\boldsymbol{F}_{\rm ac}^{\rm calib} = 2k_x U_{\rm o}\left[\frac{5\gamma-2}{2\gamma+1} - \frac{1}{\gamma\beta^2}\right]\sin(2k_x x)\,\boldsymbol{e}_x. \tag{16b}$$

The potential $U_{\rm ac}^{\rm calib}$ is shown in Fig. 8(a).

If a particle is subject to a Stokes drag force $F_{\rm drag}$ from a flow in the x-direction, then the critical flow velocity v^*, where the acoustic radiation force no longer can trap the particle is given by the condition $F_{\rm drag} = \max\{|\boldsymbol{F}_{\rm ac}^{\rm calib}|\}$ or

$$6\pi\eta a v^* = 2k_x U_{\rm o}\left[\frac{5\gamma-2}{2\gamma+1} - \frac{1}{\gamma\beta^2}\right]. \tag{17}$$

If v^* is measured experimentally, we are therefore able to determine the acoustic energy scale $U_{\rm o}$ by

$$U_{\rm o} = 3\pi\frac{\eta a v^*}{k_x}\left[\frac{5\gamma-2}{2\gamma+1} - \frac{1}{\gamma\beta^2}\right]^{-1}. \tag{18}$$

We propose a specific chip design which supports a pressure eigenmode close to the one depicted in Fig. 8(a). The idea is to fabricate an $\alpha = 3$ chip. In such a chip a strong pressure eigenmode of odd symmetry exists in the channel as the $\alpha = 1$ chip in Fig. 5(a) but it will also have a strong anti-node in the silicon as the $\alpha = 2$ chip in Fig. 5(b). Now, if two auxiliary side channels parallel to the first channel is placed at these anti-nodes, the pressure mode inside these side channels is very close to the wanted mode of Fig. 8(a). The correctness of this line of reasoning is proved by numerical simulation of the eigenmodes in such a triple-channel $\alpha = 3$ chip as shown in Fig. 8(b).

5. CONCLUDING REMARKS

By theoretical and numerical analysis we have studied the applicability of the widely used transverse half-wavelength picture. We have shown that, although not entirely correct, this picture is accurate enough to be useful. Furthermore, we have shown that it is crucial to take the entire geometry of the chip into account and match the dimensions of the surrounding silicon to those of the water channel, i.e. a global wave picture must be employed. Finally, we have presented two examples of applying this global wave picture: (*i*) a many-channel chip, which by correct matching performs significantly better in terms of amplitude and homogeneity of the acoustic energy density, and (*ii*) a three-channel chip, which enables *in situ* calibration of the acoustic radiation force.

ACKNOWLEDGMENTS

We thank Thomas Laurell and Per Augustsson at Lund University for many illuminating discussions.

REFERENCES

1. L.V. King, *Proc. R. Soc. London, Ser. A* **147**, 212 (1934).
2. K. Yosioka and Y. Kawasima, *Acustica* **5**, 167 (1955).
3. L.P. Gorkov, *Sov. Phys. Doklady* **6**, 773 (1962).
4. K. Yasuda, S. Umemura, and K. Takeda, *Jpn. J. Appl. Phys.* **34**, 2715 (1995).
5. K. Yasuda, K. Takeda, and S. Umemura, *Jpn. J. Appl. Phys.* **35**, 3295 (1996).
6. J. Spengler and M. Jekel, *Ultrasonics* **38**, 624 (2000).
7. M. Saito, N. Kitamura and M. Terauchi, *J. Appl. Phys.* **92**, 7581 (2002).
8. M. Wiklund, P. Spégel, S. Nilsson and H. M. Hertz, Ultrasonics **41**, 329 (2003).
9. J.F. Spengler, W.T. Coakley, and K.T. Christensen, *AIChE J.* **49**, 2773 (2003).
10. L. A. Kuznetsova and W. T. Coakley, *J. Acoust. Soc. Am.* **116**, 1956 (2004).
11. H. Li and T. Kenny, *Conf. Proc. 26 Ann. Int. Conf. IEEE Engineering in Medicine and Biology*, **3**(4), 2631 (2004).
12. M. Bengtsson and T. Laurell, *Anal. Chem.* **378**, 1716 (2004).
13. J. J. Hawkes, R. W. Barber, D. R. Emerson and W. T. Coakley, *Lab Chip* **4**, 446 (2004).
14. A. Nilsson, F. Petersson, H. Jonsson, and T. Laurell, *Lab Chip* ***4***, 131 (2004).
15. H. Jonsson, C. Holm, A. Nilsson, F. Petersson, P. Johnsson, and T. Laurell, *Ann. Thoracic Surgery* **78**, 1572 (2004).
16. T. Lilliehorn, U. Simu, M. Nilsson, M. Almqvist, T. Stepinski, T. Laurell, J. Nilsson, S. Johansson, *Ultrasonics* **43**, 293 (2005).
17. S. M. Hagsäter, T. G. Jensen, H. Bruus, and J. P. Kutter, *Lab Chip* **7**, 1336 (2007).
18. S. M. Hagsäter, A. Lenshof, P. Skafte-Pedersen, J. P. Kutter, T. Laurell and H. Bruus, *Lab Chip* **8**, 1178 (2008).
19. O. Manneberg, S.M. Hagsäter, J. Svennebring, H.M. Hertz, J.P. Kutter, H. Bruus, M. Wiklund Ultrasonics **49**, 112-119 (2009).
20. J. Svennebring, O. Manneberg, P. Skafte-Pedersen, H. Bruus, and M. Wiklund Biotechnol. Bioeng. **103**, 323 (2009).
21. J. Lighthill, *Waves in fluid*, (Cambridge University Press, Cambridge, 2005).
22. H. Bruus, "Acoustofluidics" in *Theoretical Microfluidics*, (Oxford University Press, Oxford, 2008).

Appendix B

Impedance condition at cylindrical boundary

To model acoustic impedance conditions of curved boundaries, a cylindrically shaped boundary, between two domains, is investigated. We imagine the cylinder to be infinitely high, which thus leads to translational invariance in the z-direction. Inside the cylinder is one medium (1), while outside is another but infinitely extending medium (2). Leaving out the angular dependence θ due to angular invariance, the Helmholtz equation reads

$$\nabla^2\phi(r,t) = -k^2\phi(r,t), \tag{B.1}$$

where ϕ is the velocity potential and $k = \frac{\omega}{c}$ is the wave number of the medium. The Laplacian is

$$\nabla^2 = \partial^2 + \frac{1}{r}\partial_r. \tag{B.2}$$

As the solution can be expressed as a product between the solution to the spatial part and a solution to the time part, $\phi(r,t) = R(r)T(t)$, we now focus on the spatial part as time solution is already assumed to be hamonic in the above stated Helmholtz equation. The spatial solution to the polar wave equation in Eq. (B.2) is known to be a linear combination of Bessel functions in zeroth order (zeroth order because we have no angular dependence)

$$R(r) = AJ_0(kr) + BY_0(kr), \tag{B.3}$$

where A and B are constants. In order to describe cylindrical waves the linear combination of Bessel functions is given by the so-called Hankel functions. The zeroth order Hankel functions are

$$H_0^{(1)}(kr) = J_0(kr) + iY_0(kr), \tag{B.4}$$

$$H_0^{(2)}(kr) = J_0(kr) - iY_0(kr), \tag{B.5}$$

which obeys same algebraic rules as the ordinary Bessel functions and where $H_0^{(1)}$ is the outward going wave and $H_0^{(2)}$ is the inward going wave. In order to consider waves

propagating from the cylinder, we envisage a thin cylindrical piezo-actuator placed in the center of the boundary between the two media. We can therefore now write the velocity potential in each of the two media/domains

$$\phi_1(r,t) = \left[A_1 H_0^{(1)}(k_1 r) + B_1 H_0^{(2)}(k_1 r)\right] e^{-i\omega t}, \qquad a_0 < r < a, \tag{B.6}$$

$$\phi_2(r,t) = A_2 H_0^{(1)}(kr) e^{-i\omega t}, \qquad r > a, \tag{B.7}$$

where a_0 is the radius of the piezo-actuator inside domain 1 and a is the radius of the boundary between the two domains. Notice that we only consider outwards going waves in domain 2 as we consider it to extend infinitely. The boundary conditions at the interface of the domains are, by the demanding continuity in velocity and pressure, given as

$$\partial_r \phi_1(a,t) = \partial_r \phi_2(a,t), \quad \text{continuity in velocity,} \tag{B.8}$$

$$\rho_1 \phi_1(a,t) = \rho_2 \phi_2(a,t), \quad \text{continuity in pressure.} \tag{B.9}$$

With the objective of rewriting the interface conditions into one single requirement on the pressure p_1 in domain 1, the spatial derivative of ϕ_2 is found

$$\partial_r \phi_2(a,t) = -k_2 A_2 H_1^{(1)}(k_2 a) e^{-i\omega t}, \tag{B.10}$$

which is seen not to be a linear combination of $\phi_2(a,t)$. Asymptotic forms are therefore needed to continue.

Asymptotic expansion for large a The asymptotic form in the case of $|z| \to \infty$ for the $H_\nu^{(1)}(z)$ Hankel function of order ν is

$$H_\nu^{(1)}(z) \approx \sqrt{\frac{2}{\pi z}} e^{i(z - \frac{\nu\pi}{2} - \frac{\pi}{4})} \left[1 + \sum_{n=1}^{\infty} \frac{(\frac{1}{2}+\nu)_\nu (\frac{1}{2}-\nu)_n}{n!(2iz)^n}\right], \tag{B.11}$$

where the notation $(\alpha)_\beta = \frac{\Gamma(\alpha+\beta)}{\Gamma(\alpha)}$ is used [56]. Using this to expand $H_0^{(1)}(k_2 a)$ and $H_1^{(1)}(k_2 a)$ to $n = 1$ (or order $(k_2 a)^{-3/2}$) gives

$$H_0^{(1)}(k_2 a) \approx \sqrt{\frac{2}{\pi k_2 a}} e^{i(k_2 a - \pi/4)} \left[1 - \frac{i}{4}\frac{1}{k_2 a}\right], \tag{B.12}$$

$$H_0^{(1)}(k_2 a) \approx i\sqrt{\frac{2}{\pi k_2 a}} e^{i(k_2 a - \pi/4)} \left[1 + 3i\frac{1}{k_2 a}\right]. \tag{B.13}$$

Keeping the order of $(k_2 a)^{-3/2}$, the spatial derivative of $\phi_2(a,t)$ in Eq.(B.10) is rewritten to

$$\partial_r \phi_2(a,t) \approx -ik_2 \phi_2(a,t) \left[1 - i\frac{11}{4}\frac{1}{k_2 a}\right], \tag{B.14}$$

which rewritten into a condition on $p_1(a,t)$ gives

$$\frac{1}{\rho_1}\partial_r p_1(a,t) = -\frac{i\omega}{Z_2} p_1(a,t) \left[1 - i\frac{11}{4}\frac{1}{k_2 a}\right] + O\left[(k_2 a)^{-5/2}\right], \tag{B.15}$$

where $Z_2 = \rho_2 c_2$ is the impedance of medium 2. As the curvature of the cylinder $\kappa = \frac{1}{a} \to 0$ the condition on $p_1(a,t)$ is seen to equal the condition when considering a plane wall interface. This makes qualitatively good sense as the cylindrical waves reduces to plane waves as the distance from the origin of the wave is large.

Appendix C

Comsol/Matlab script for pressure eigenmodes in 2D chip model

Below we show the script for solving the pressure eigenmodes for a 2D chip geometry. The script uses x- and y-symmetry.

```
% 2D symmetric chip model, eigenvalue analysis
%
% Rune Barnkob, DTU Nanotech 2009

%% Initialization
clear all, flclear fem, close all
disp('Fem2D_SymmetricBox.m');

%% Constants
N = 2; % Number of resonance frequencies to investigate

cWa = 1483;      % Water: speed of sound
cSi = 8490;      % Silicon: speed of sound
rhoWa = 998;     % Water: density
rhoSi = 2331;    % Silicon: density

alpha = 2;
L = 55.00e-3;    % Length, silicon chip
l = 29.30e-3;    % Length, water channel
w = 380e-6;      % Width, water channel
W = w*(1+cSi/cWa*alpha); % Width, water chamber

f0 = cWa/2/w;
fs = f0;                          % Frequency to search for
points_mesh = 60;        % Number of mesh points per wavelength
points = 100;            % Additional number of points to evaluate
y0 = 0.0;                         % Crosssection-line to investigate

% Parity factors
```

```
paX = +1; % +1 even, -1 odd
paY = +1; % +1 even, -1 odd

if paX == -1
    BCX = 1;
else
    BCX = 0;
end

if paY == -1
    BCY = 1;
else
    BCY = 0;
end

const = struct('cWa',cWa,'cSi',cSi,'rhoWa',rhoWa,'rhoSi',rhoSi,...
    'w',w,'l',l,'W',W,'L',L,'y0',y0,'BCX',BCX,'BCY',BCY);

%% EVP - determining resonance frequencies near lambda/2
fem.const = const;

% Geometry %%
g1 = rect2(w/2,l/2,'base','corner','pos',[0 0]);
g2 = rect2(W/2,L/2,'base','corner','pos',[0 0]);
s.objs={g1,g2};
fem.draw=struct('s',s);
fem.geom=geomcsg(fem);
% sfigure(1),geomplot(fem,'sublabels','on','edgelabels','off')
% axis equal
% return

% Equations %%
% Subdomain Groups:
% [1] Water subdomain
% [2] Silicon subdomain
% Boundary Groups:
% [1] Si-water interface, continuity
% [2] Si-air interface, soft
% [3] Symmetry-X
% [4] Symmetry-Y
fem.equ.ind = {1 2};
fem.bnd.ind = {[4 6] [5 8] [1 3] [2 7]};

% Variables
fem.sdim = {'x','y'};
fem.dim = {'p'};
fem.shape = 2;

% Governing equations
```

```
79  fem.form = 'general';
80  fem.equ.expr = {...
81      'c',{'cWa','cSi'},...
82      'rho',{'rhoWa','rhoSi'},...
83      'Eaco',{'((abs(px)^2+abs(py)^2)/omega^2 + abs(p)^2/c^2)/(4*rho)
            '}};
84  fem.equ.shape = {1 1};  % define p in both domain groups
85  fem.equ.ga = {{'px/rho';'py/rho'}};
86  fem.equ.f = {{'-omega^2*p/(rho*c^2)'}};
87  fem.equ.init = {{'0'}}; % p is initially set to 0 everywhere
88
89  % Boundary conditions
90  fem.bnd.shape = {1,1,1,1};  % define p on all boundaries
91  fem.bnd.r = {... % only looking for uneven modes!
92      {'0'}, ...          % BC group [1]
93      {'0-p'}, ...        % BC group [2]
94      {'0-BCX*p'}, ...    % BC group [3]
95      {'0-BCY*p'}};       % BC group [4]
96
97  fem.bnd.g = { ...
98      {'0'}, ...      % BC group [1]
99      {'0'}, ...      % BC group [2]
100     {'0'}, ...      % BC group [3]
101     {'0'}};         % BC group [4]
102
103 % Meshing
104 mSi = cSi/f0/points_mesh;
105 mWa = cWa/f0/points_mesh;
106 fem.mesh = meshinit(fem,'report','off','hmaxsub',[1 2; mWa mSi]);
107 fem.xmesh = meshextend(fem);
108 DOF = flngdof(fem);
109 % sfigure(2); meshplot(fem);
110 % axis equal
111 % return
112
113 % Solving EVP
114 fem.sol=femeig(fem, ...
115     'solcomp',{'p'}, ...
116     'outcomp',{'p'}, ...
117     'eigname','omega',...
118     'shift',2*pi*fs,...
119     'neigs',N, ...
120     'linsolver','spooles',... %'pardiso',... %
121     'etol',1e-10);
122
123 omega_vec = fem.sol.lambda;
124
125 %% Postprocessing for all resonance frequencies
126 Ewa = zeros(1,length(omega_vec));
```

```
Esi = Ewa;

xvwa = (0+mWa/points):mWa/points:(w/2-mWa/points); % points channel
xvsi = (w/2+mSi/points):mSi/points:(W/2-mSi/points); % points chip
Edens_wa = zeros(length(omega_vec),length(xvwa));
Edens_si = zeros(length(omega_vec),length(xvsi));

for j = 1:length(omega_vec)

    % Surface plots of pressure field in different p limits
    sfigure(3);
    postplot(fem,'tridata','p','solnum',j)
    xlabel('x'),ylabel('y')
    axis equal

    % Aquiring acoustic energies
    yv0wa = y0*ones(1,length(xvwa));
    yv0si = y0*ones(1,length(xvsi));
    Edens_wa(j,:) = postinterp(fem,'Eaco',[xvwa;yv0wa],...
        'solnum',j,'Dl',1,'edim',2);
    Edens_si(j,:) = postinterp(fem,'Eaco',[xvsi;yv0si],...
        'solnum',j,'Dl',2,'edim',2);
    EmaxWa = max(Edens_wa(j,:));
    EmaxSi = max(Edens_si(j,:));
    Awa = w*l; % total area of water channels
    Asi = W*L-w*l; % total area of silicon chip
    Ewa(j) = 1/(Awa/4)*postint(fem,'Eaco','Dl',1,'edim',2,'solnum',
       j);
    Esi(j) = 1/(Asi/4)*postint(fem,'Eaco','Dl',2,'edim',2,'solnum',
       j);

    % Plot pressure along y0
    p_wa = postinterp(fem,'p',[xvwa;yv0wa],'solnum',j);
    p_si = postinterp(fem,'p',[xvsi;yv0si],'solnum',j);
    sfigure(4);
    plot(xvwa/1e-3,p_wa/max(p_si),'-r',xvsi/1e-3,p_si/max(p_si),'-b
       ');
    xlabel('y [mm]'),ylabel('p/pmax [Pa]')
    delta = cWa/(omega_vec(j)/2/pi)/2/w-1;

    % Writing info to screen
    fprintf(1,'f0: %6.4f MHz, DOF: %i, alpha: %2.3f\n',f0/1e6,DOF,
       alpha);
    fprintf(1,['No.: %i/%i, f: %6.4f MHz, delta: %6.8f, ' ...
        'EmaxWa/EmaxSi: %2.3f, Ewa/EmaxSi: %2.3f\n'],...
        j,length(omega_vec),omega_vec(j)/2/pi/1e6,delta,...
        EmaxWa/EmaxSi,Ewa(j)/EmaxSi);
    pause
end
```

Appendix D

Comsol/Matlab script for eigenmodes in translational inv. 3D model

Below we show the script for solving the pressure eigenmodes for a chip geometry of a translational invariance along its axial direction. This script is described in detail in Chap. 3 on COMSOL MULTIPHYSICS.

```
%% Initialization
clear all, flclear fem, close all

% Material parameters
cWa = 1483;      % Water: speed of sound
cPy = 5603;      % Pyrex: speed of sound
cSi = 8490;      % Silicon: speed of sound
rhoWa = 998;     % Water: density
rhoSi = 2331;    % Silicon: density
rhoPy = 2230;    % Pyrex: density
% Geometric parameters
L = 40e-3;       % Length, silicon/pyrex chip
w = 0.375e-3;    % Width, water-filled channel
W = 4e-3;        % Width, silicon/pyrex chip
hSi = 0.350e-3; % Height, silicon chip
hPy = 1.13e-3;   % Height, pyrex lid
hWa = 0.157e-3; % Height, water-filled channel
% Wave number in x-direction
kx = pi/L;       % nx=1

% Constants into fem-struct
fem.const = struct('cWa',cWa,'cSi',cSi,'cPy',cPy,...
    'rhoWa',rhoWa,'rhoSi',rhoSi,'rhoPy',rhoPy,'kx',kx);

% Geometry
g1 = rect2(W/2,hPy,'base','corner','pos',[0 0]);
```

```
g2 = rect2(w/2,hWa,'base','corner','pos',[0 -hWa]);
g3 = rect2(W/2,hSi,'base','corner','pos',[0 -hSi]);
s.objs={g1,g2,g3};
fem.draw=struct('s',s);
fem.geom=geomcsg(fem);
% figure(1),geomplot(fem,'sublabels','off','edgelabels','on')
% axis equal % xlabel('y [m]'),ylabel('z [m]')
% return

% Equations %%
% Subdomain Groups:
% [1] Water subdomain
% [2] Silicon subdomain
% [3] Pyrex subdomain
% Boundary Groups:
% [1] Interface, continuity
% [2] Air-interface, soft
% [3] y-symmetry
% [4] Piezo, hard wall
fem.equ.ind = {2 1 3};
fem.bnd.ind = {[4 8 6 9] [7 10 11] [1 3 5] [2]};

% Variables
fem.sdim = {'y','z'};
fem.dim = {'p'};
fem.shape = 2;

% Governing equations on general form
fem.form = 'general';
fem.equ.expr = {'c',{'cWa','cSi','cPy'},'rho',{'rhoWa','rhoSi','
    rhoPy'}};
fem.equ.shape = {1 1 1};     % Defining p in all domain groups
fem.equ.ga = {{{'py/rho';'pz/rho'}}};
fem.equ.f = {{'-(omega^2/c^2-kx^2)*p/rho'}};
fem.equ.init = {{'0'}};      % p is initially set to 0 everywhere

% Boundary conditions on general form
fem.bnd.shape = {1,1,1,1};  % Defining p on all boundaries
fem.bnd.r = {...
    {'0'}, ...       % BC group [1] Interface, continuity
    {'0-p'}, ...     % BC group [2] Air-interface, soft
    {'0-1*p'}, ...   % BC group [3] y-symm.: -1*p (even), 0*p (odd)
    {'0'}};          % BC group [4] Piezo, hard wall
fem.bnd.g = { ...
    {'0'}, ...       % BC group [1] Interface, continuity
    {'0'}, ...       % BC group [2] Air-interface, soft
    {'0'}, ...       % BC group [3] y-symm.
    {'0'}};          % BC group [4] Piezo, hard wall

```

```
% Meshing
mSi = cSi/2e6/50; % 50 meshes per silicon wavelength at 2 MHz
mWa = cWa/2e6/50; % 50 meshes per water wavelength at 2 MHz
mPy = cPy/2e6/50; % 50 meshes per pyrex wavelength at 2 MHz
fem.mesh = meshinit(fem,'hmaxsub',[2 1 3; mWa mSi mPy]);
fem.xmesh = meshextend(fem);
% figure(2); meshplot(fem);% xlabel('y [m]'),ylabel('z [m]')
% axis equal
% return

% Solving EVP
fem.sol=femeig(fem, ...
    'solcomp',{'p'}, ...
    'outcomp',{'p'}, ...
    'eigname','omega',...
    'shift',2*pi*0,...
    'neigs',1, ...
    'linsolver','spooles',...
    'etol',1e-8);

omega_vec = fem.sol.lambda;
f_vec = omega_vec/2/pi

%% Postprocessing
figure(1);
postplot(fem,'tridata','p','tridlim',[-2.1 2.1],'solnum',1)
xlabel('y [m]'),ylabel('z [m]')
axis equal
axis([0 2e-3 -4e-4 12e-4])
```

Appendix E

Comsol/Matlab script for resonances in point-actuated 3D model

Below we show the script for the computation of the acoustic resonances for the point-actuated 3D model treated in Chap. 4.

```
%% COMSOL-MATLAB-script: CircAct_func_Zair.m
% Driven 3D acoustic resonance analysis
% MSc-student Rune Barnkob, TMF, DTU Nanotech, 2008/2009
% 22-10-2008
%
% Script for sweeping in frequencies and in Zair
%
% The system consists of a silicon chip containing a water cavity. Acoustic
% resonances in the chip is actuated by a circular actuator, which is
% applied to the top surface of the chip.
% Variation possibilities: position of actuator and BCs on the chip
% surface (last mentioned can create circular fixations by choosing proper
% impedance conditions).
%
%%
function CircAct_func_Zair

disp(' ')
disp('CircAct_func_Zair_Pins.m started');
flreport('off')

%% Initialization
clear all, close all, flclear fem

```

```
%% Variables to define
freq1 = 720e3;
freq2 = 800e3;
tol = 0.0001e3; % tolerance in Golden Section Search

ZZ = [0.5 1 2 3 4 5 6 7 8 9 10]; % Impedance factors

%% Geometry parameters
L0 = 10.5e-3; W0 = 3.2e-3; H0 = 1.0e-3;      % Silicon chip box
L1 = 4.7e-3; W1 = 1.4e-3; H1 = 0.3e-3;       % Water cavity box
x1 = 1.3e-3; y1 = 0.68e-3; z1 = 0.3e-3;      % Water box corner
    coordinate

Lmb = L0; Wmb = W0; Hmb = 0.15e-3;           % Interior "mesh"-box,
    top (b)
Lmt = L0; Wmt = W0; Hmt = 0.15e-3;           % Interior "mesh"-box,
    top (t)
xmt = 0; ymt = 0; zmt = 0.85e-3;             % Top-"mesh"-box
    coordinates

r_act = 0.3E-3;                              % Actuator radius

fem.const = struct('L0',L0,'W0',W0,'H0',H0, ...
    'L1',L1,'W1',W1,'H1',H1);

%% Physical parameters
fem.const.rho_water = 998;                % Density: water
fem.const.rho_air = 1.25;                 % Density: air
fem.const.rho_silicon = 2331;             % Density: silicon
fem.const.rho_iron = 7874;                % Density: iron
fem.const.ca_water = 1483;                % Sound velocity: water
fem.const.ca_air = 343;                   % Sound velocity: air
fem.const.ca_silicon = 8490;              % Sound velocity: silicon
fem.const.ca_iron = 5120;                 % Sound velocity: iron
fem.const.act_acc = 1;                    % Actuator acceleration
fem.const.ic = sqrt(-1);                  % Complex i
fem.const.gamma = 0;                      % Viscos damping factor
fem.const.omega = 0;                      % Initialize angular
    frequency
fem.const.Z_air = fem.const.rho_air*fem.const.ca_air;       % Air-
    impendance
fem.const.Z_silicon = fem.const.rho_silicon*fem.const.ca_silicon;
      % Silicon-impendance
fem.const.Z_iron = fem.const.rho_iron*fem.const.ca_iron;    % Iron-
    impendance

%% Geometry creation
% Silicon chip rectangle (subdivided in three parts)
g1 = block3(L0,W0,H0-2*Hmt,'base','corner','pos',[0,0,Hmt]);
```

```
66 g3 = block3(Lmb,Wmb,Hmb,'base','corner','pos',[0,0,0]);
67 g4 = block3(Lmt,Wmt,Hmt,'base','corner','pos',[xmt,ymt,zmt]);
68 % Water cavity rectangle
69 g2 = block3(L1,W1,H1,'base','corner','pos',[x1,y1,z1]);
70
71 % Embedding array of cirles on chip surface
72 ChessGeometry_input % loading array of circles
73 g5 = embed(c1+c2+c3+c4+c5+c6+c7+c11+c21+c12+c22+c13+c23+c14+c24+
       ...
74     c15+c25+c16+c26+c17+c27+c18+c28,'Wrkpln',[0 1 0;0 0 1;0 0 0]);
         % embed bottom
75 g6 = embed(c1+c2+c3+c4+c5+c6+c7+c11+c21+c12+c22+c13+c23+c14+c24+
       ...
76     c15+c25+c16+c26+c17+c27+c18+c28,'Wrkpln',[0 1 0;0 0 1;H0 H0 H0
         ]); % embed top
77
78 % Analyzed geometry
79 s.objs={g1-g2,g2,g3,g4};
80 f.objs={g5,g6};
81
82 fem.draw=struct('s',s,'f',f);
83 fem.geom=geomcsg(fem);
84
85 %% Equations
86 % Subdomain Groups:
87 % [1] Silicon subdomain
88 % [2] Water subdomain
89 % Boundary Groups:
90 % [1] Si-air interface, impedance
91 % [2] Si-water interface, continuity
92 % [3] Actuator, normal acceleration
93 % [4] Si-fixations interface, impedance
94
95 fem.equ.ind = {1:3 4};
96 fem.bnd.ind = {[66:68 1:5 7:8 10:13 23:34 36:46 48:61] [18:22 47]
       35 [14:17 62:65]}; % (1) with interiors, 6 9 is excluded
97
98 % Variables
99 fem.sdim = {'x','y','z'};
100 fem.dim = {'p'};
101 fem.shape = 2;
102
103 % Governing equations
104 fem.form = 'general';
105 fem.equ.shape = {1 1};  % define p in both subdomains
106 fem.equ.ga = { ...
107     {{'px/rho_silicon';'py/rho_silicon';'pz/rho_silicon'}}, ...
108     {{'px/rho_water';'py/rho_water';'pz/rho_water'}}};
109 fem.equ.f = { ...
```

```
110     {'-omega^2*p/(rho_silicon*ca_silicon^2)'}, ... % no gamma for
            Si
111     {'-(omega*(1+ic*gamma))^2*p/(rho_water*ca_water^2)'}};
112 fem.equ.init = {{'0'},{'0'}}; % p is initially set to 0 everywhere
113
114 % Boundary conditions
115 fem.bnd.shape = {1,1,1,1};  % define p on all boundaries
116 fem.bnd.r = {{0}, {0}, {0}, {0}};   % no Dirichlet conditions
117 fem.bnd.g = { ...
118     {'-ic*omega*p/(Z_fact*Z_air)'}, ...        % BC group [1]
119     {'0'}, ...                                   % BC group [2]
120     {'act_acc'}, ...                             % BC group [3]
121     {'-ic*omega*p/(Z_fact*Z_iron)'}};           % BC group [4]
122
123 %% Meshing
124 % load('../../Mesh_CircGrid_hauto=3_DOF=56811.mat')
125 file = load('../../Mesh_CircGrid_hauto=4_DOF=33605.mat');
126 fem.mesh = file.mesh;
127 fem.xmesh = meshextend(fem);
128
129 %% Sweeping in Z_fact
130
131 for i = 1:length(ZZ)
132
133     fem.const.Z_fact = ZZ(i); % Impedance factor
134     fem.xmesh = meshextend(fem);
135
136     %% Golden section search
137     a = freq1; b = freq2;
138
139     x = a + (b-a)/2;
140     [Ewa_x,Esi_x,Etot_x] = func(x,fem);
141     [Ewa_a,Esi_a,Etot_a] = func(a,fem);
142     [Ewa_b,Esi_b,Etot_b] = func(b,fem);
143
144     ff = [a;b;x];
145     Ewa = [Ewa_a;Ewa_b;Ewa_x];
146     Esi = [Esi_a;Esi_b;Esi_x];
147     Etot = [Etot_a;Etot_b;Etot_x];
148
149     j = 0;
150     while b-a > tol
151         j = j + 1;
152         if Etot_a > Etot_x
153             b = x;
154             x = a + (b-a)/2;
155             [Ewa0,Esi0,Etot0,time] = func(x,fem);
156             Etot_x = Etot0;
157             f0 = x;
```

```
158         elseif Etot_b > Etot_x
159             a = x;
160             x = a + (b-a)/2;
161             [Ewa0,Esi0,Etot0,time] = func(x,fem);
162             Etot_x = Etot0;
163             f0 = x;
164         else
165             if Etot_a > Etot_b
166                 b = b - (b-x)/2;
167                 [Ewa0,Esi0,Etot0,time] = func(b,fem);
168                 Etot_b = Etot0;
169                 f0 = b;
170             else
171                 a = a + (x-a)/2;
172                 [Ewa0,Esi0,Etot0,time] = func(a,fem);
173                 Etot_a = Etot0;
174                 f0 = a;
175             end
176         end
177         ff = [ff;f0];
178         Ewa = [Ewa;Ewa0];
179         Esi = [Esi;Esi0];
180         Etot = [Etot;Etot0];
181         fprintf(1,'Z no. %i/%i, Z: %i, f no. %i, f: %6.4f kHz, Etot
               : %6.6f aJ, (b-a)/tol: %6.6f, time: %6.0f\n',...
182             i,length(ZZ),ZZ(i),j,f0/1e3,Etot0/1e-18,(b-a)/tol,time)
                   ;
183
184         % Implement stop criteria: old(b-a) less than (b-a)
185
186         plot(ff,Etot,'ro'),shg
187
188         name = ['SweepGold_' num2str(freq1/1e3) 'kHz_' num2str(
               freq2/1e3) 'kHz'];
189         save([name 'Z' num2str(ZZ(i)) '_energy.mat'],'ff','Ewa','
               Esi','Etot')
190         save([name 'Z' num2str(ZZ(i)) '_fem.mat'],'fem')
191     end
192     fprintf(1,'\n');
193 end
194
195 disp('CircAct_func_Zair_pins.m ended');
196 disp(' ');
197
198
199 %% Function to solve system by "femstatic"
200 function [Ewa,Esi,Etot,time] = func(f,fem)
201 tic
202 fem.const.omega = 2*pi*f;
```

```
fem.sol=femstatic(fem, ...
    'solcomp',{'p'}, ...
    'outcomp',{'p'}, ...
    'ntol',1e-006);
Ewa = postint(fem, ...
    '((abs(px)^2+abs(py)^2+abs(pz)^2)/omega^2 + (abs(p)/ca_water)
       ^2)/(4*rho_water)', ...
    'Dl',4,'edim',3); % Water cavity energy
Esi = postint(fem, ...
    '((abs(px)^2+abs(py)^2+abs(pz)^2)/omega^2 + (abs(p)/ca_silicon)
       ^2)/(4*rho_silicon)', ...
    'Dl',1:3,'edim',3); % Silicon chip energy
Etot = Ewa + Esi;
time = toc;
```

Appendix F

Comsol/Matlab script for investigating 2D waveguide modes

```
% 2D eigenvalue simulation of 2D waveguide modes
%
% y-direction: parallel to channel
% x-direction: perpendicular to channel
%
% Rune Barnkob, DTU Nanotech 2009

%% Initialization
clear all, flclear fem, close all
disp('waveguide2D_transinv.m');

%% Constants
N = 1; % Number of resonance frequencies to investigate

cWa = 1483;      % Water: speed of sound
cSi = 8490;      % Silicon: speed of sound
rhoWa = 998;     % Water: density
rhoSi = 2331;    % Silicon: density

w = 375e-6;              % Width, water-filled channel
alpha = 1;
W = w*(1+cSi/cWa*alpha); % Width, silicon chip

f0 = 2e6;
fs = 0*2.000e6;      % Frequency to search for
points_mesh = 100;   % Number of mesh points per wavelength
points = 1000;        % Additional number of points to "postinterp"
mSi = cSi/f0/points_mesh;
mWa = cWa/f0/points_mesh;

% Postprocessing for all resonance frequencies
yvwa = (0+mWa/points):mWa/points:(w/2-mWa/points); % points channel
```

```
33 yvsi = (w/2+mSi/points):mSi/points:(W/2-mSi/points); % points chip
34
35 % y-parity factors
36 paY = -1; % +1 even, -1 odd
37
38 if paY == -1
39     BCY = 1;
40 else
41     BCY = 0;
42 end
43
44 % L_On = 0;
45 % L = 40e-3;                                % Length, silicon chip
46 % nx = [0.1,1,10]*L/(cSi/cWa)/w;
47 % for j = 1:length(nx)
48 %     n = nx(j);
49
50 L_On = 1;
51 n = 1;
52 Lx = [0.1,1,10]*(cSi/cWa)*w;
53 p_wa = zeros(length(Lx),length(yvwa));
54 p_si = zeros(length(Lx),length(yvsi));
55 for j = 1:length(Lx)
56     L = Lx(j);
57
58     % Wave number in x-direction
59     kx = n*pi/L;  % kx = n*pi/L, n odd - sym. paX=+1, n even -
       antisym. paX=-1
60
61     const = struct('cWa',cWa,'cSi',cSi,'rhoWa',rhoWa,'rhoSi',rhoSi
       ,...
62         'w',w,'W',W,'BCY',BCY,'kx',kx);
63
64     %% EVP - determining resonance frequencies near lambda/2
65     fem.const = const;
66
67     % Geometry %%
68     g1 = solid1([0,w/2]);
69     g2 = solid1([w/2,W/2]);
70     s.objs={g1,g2};
71     fem.draw=struct('s',s);
72     fem.geom=geomcsg(fem);
73     % figure(1),geomplot(fem,'sublabels','off','pointlabels','on')
74     % axis equal
75     % return
76
77     % Equations %%
78     % Subdomain Groups:
79     % [1] Water subdomain
```

```
80      % [2] Silicon subdomain
81      % Boundary Groups:
82      % [1] Si-water interface, continuity
83      % [2] Si-air interface, soft
84      % [3] Symmetry-Y
85      fem.equ.ind = {1 2};
86      fem.bnd.ind = {2 3 1};
87
88      % Variables
89      fem.sdim = {'y'};
90      fem.dim = {'p'};
91      fem.shape = 2;
92
93      % Governing equations (can be reduced to only one type of
            equations)
94      fem.form = 'general';
95      fem.equ.expr = {...
96          'c',{'cWa','cSi'},...
97          'rho',{'rhoWa','rhoSi'},...
98          'Eaco',{'(abs(py)^2/omega^2 + abs(p)^2/c^2)/(4*rho)'}};
99      fem.equ.shape = {1 1};  % define p in both domain groups
100     fem.equ.ga = {{{'py/rho'}}};
101     fem.equ.f = {{'-(omega^2/c^2-kx^2)*p/rho'}};
102     fem.equ.init = {{'0'}}; % p is initially set to 0 everywhere
103
104     % Boundary conditions
105     fem.bnd.shape = {1,1,1};  % define p on all boundaries
106     fem.bnd.r = {... % only looking for uneven modes!
107         {'0'}, ...          % BC group [1]
108         {'0-p'}, ...        % BC group [2]
109         {'0-BCY*p'}};       % BC group [3]
110
111     fem.bnd.g = { ...
112         {'0'}, ...      % BC group [1]
113         {'0'}, ...      % BC group [2]
114         {'0'}};         % BC group [3]
115
116     % Meshing
117     fem.mesh = meshinit(fem,'report','off','hmaxsub',[1 2; mWa mSi
            ]);
118     fem.xmesh = meshextend(fem);
119     DOF = flngdof(fem);
120     % figure(2); meshplot(fem);
121     % axis equal
122     % return
123
124     % Solving EVP
125     fem.sol=femeig(fem, ...
126         'solcomp',{'p'}, ...
```

```
127         'outcomp',{'p'}, ...
128         'eigname','omega',...
129         'shift',2*pi*fs,...
130         'neigs',N, ...
131         'linsolver','spooles',... %'pardiso',... %
132         'etol',1e-10);
133 
134     omega = fem.sol.lambda;
135     f = omega/2/pi;
136 
137     %% Get pressures
138     p_wa(j,:) = postinterp(fem,'p',yvwa,'solnum',1);
139     p_si(j,:) = postinterp(fem,'p',yvsi,'solnum',1);
140     %% Get energy densities
141     Ewa(j) = 1/(w/2)*postint(fem,'Eaco','Dl',1,'edim',1,'solnum',1)
            ;
142     Esi(j) = 1/(W/2-w/2)*postint(fem,'Eaco','Dl',2,'edim',1,'solnum
            ',1);
143     delta = cWa/(omega/2/pi)/2/w-1;
144 
145     fprintf(1,'L: %3.2f mm, nx: %1.0f, f: %2.5f MHz, alpha: %i, Ewa
            /Esi: %2.3f, delta: %1.2f\n',...
146         L/1e-3,n,f/1e6,alpha,Ewa(j)/Esi(j)/2,delta*100);
147 
148 end
149 
150 pmaxsi = max(max(p_si));
151 pmaxwa = max(max(p_wa));
152 pmax = max([pmaxwa pmaxsi]);
153 
154 if L_On == 1
155     % Plot pressure
156     plot(...
157         [yvwa yvsi]/(W/2),[p_wa(1,:) p_si(1,:)]/pmax,'-b',...
158         [yvwa yvsi]/(W/2),[p_wa(2,:) p_si(2,:)]/pmax,'-r',...
159         [yvwa yvsi]/(W/2),[p_wa(3,:) p_si(3,:)]/pmax,'-k',...
160         [w/2/(W/2) w/2/(W/2)],[0 1],'--k')
161     axis([0 1 0 1])
162     xlabel('y/(W/2)'),ylabel('p/pmax')
163     % L legend
164     legend( ['L=0.1*(cSi/cWa)*w=' num2str(Lx(1)/1e-3) 'mm'],...
165         ['L=1*(cSi/cWa)*w=' num2str(Lx(2)/1e-3) 'mm'],...
166         ['L=10*(cSi/cWa)*w=' num2str(Lx(3)/1e-3) 'mm'])
167 else
168     % Plot pressure
169     plot(...
170         [yvwa yvsi]/(W/2),[p_wa(1,:) p_si(1,:)]/pmax,'-b',...
171         [yvwa yvsi]/(W/2),[p_wa(2,:) p_si(2,:)]/pmax,'-r',...
172         [yvwa yvsi]/(W/2),[p_wa(3,:) p_si(3,:)]/pmax,'-k',...
```

```
173         [w/2/(W/2) w/2/(W/2)],[0 1],'--k')
174     axis([0 1 0 1])
175     xlabel('y/(W/2)'),ylabel('p/pmax')
176     % n legend
177     legend( ['nx=0.1*L/(cSi/cWa)/w=' num2str(nx(1))],...
178         ['nx=1*L/(cSi/cWa)/w=' num2str(nx(2))],...
179         ['nx=10*L/(cSi/cWa)/w=' num2str(nx(3))])
180 end
181 disp(' ')
182 return
```

Bibliography

[1] G. Karniadakis and A. Beskok, *Micro flows: fundamentals and simulation*. Springer-Verlag, New York, 2002.

[2] O. Geschke, H. Klank, and P. Telleman, *Microsystem engineering of lab-on-a-chip devices*. Wiley-VCH Verlag, Weinheim, 2004.

[3] P. Tabeling, *Introduction to microfluidics*. Oxford University Press, Oxford, 2005.

[4] J. Berthier and P. Silberzan, *Microfluidics for biotechnology*. Artech House, Boston, 2006.

[5] H. Bruus, *Theoretical microfluidics*. Oxford University Press, 2008.

[6] H. Stone, A. Stroock, and A. Ajdari, "Engineering flows in small devices: Microfluidics toward a lab-on-a-chip," *Annu. Rev. Fluid Mech.*, vol. 36, pp. 381–411, 2004.

[7] T. M. Squires and S. R. Quake, "Microfluidics: Fluid physics at the nanoliter scale," *Review of modern physics*, vol. 77, pp. 977–1026, 2005.

[8] G. M. Whitesides, "The origins and the future of microfluidics," *Nature*, vol. 442, pp. 368–373, 2006.

[9] M. Faraday, "On a Peculiar Class of Acoustical Figures; and on Certain Forms Assumed by Groups of Particles upon Vibrating Elastic Surfaces," *Philosophical Transactions of the Royal Society of London*, vol. 121, pp. 299–340, 1831.

[10] A. Kundt and O. Lehmann, "Longitudinal vibrations and acoustic figures in cylindrical columns of liquids," *Ann. Phys. Chem.*, vol. 153, p. 1, 1874.

[11] L. Rayleigh, "On the Circulation of Air Observed in Kundt's Tubes, and on Some Allied Acoustical Problems," *Philosophical Transactions Series I*, vol. 175, pp. 1–21, 1884.

[12] L. V. King, "On the Acoustic Radiation Pressure on Spheres," *Proceedings of the Royal Society of London. Series A, Mathematical and Physical Sciences*, vol. 147 (861), pp. 212–240, 1934.

[13] C. Eckart, "Vortices and Streams Caused by Sound Waves," *Phys. Rev.*, vol. 73, pp. 68–76, Jan 1948.

[14] J. Markham, "Second-Order Acoustic Fields: Relations between Energy and Intensity," *Physical Review*, vol. 89, no. 5, pp. 972–977, 1953.

[15] J. Markham, "Second-Order Acoustic Fields: Relations Between Density and Pressure," *Physical Review*, vol. 86, no. 5, pp. 710–711, 1952.

[16] J. Markham, "Second-Order Acoustic Fields: Energy Relations," *Physical Review*, vol. 86, no. 5, pp. 712–714, 1952.

[17] J. Markham, "Second-Order Acoustic Fields: Streaming with Viscosity and Relaxation," *Physical Review*, vol. 86, no. 4, pp. 497–502, 1952.

[18] J. Markham, R. T. Beyer, and R. B. Lindsay, "Absorption of Sound in Fluids," *Reviews of Modern Physics*, vol. 23, no. 4, pp. 353–411, 1951.

[19] W. L. Nyborg, "Acoustic streaming due to attenuated plane waves," *Journal of the Acoustical Society of America*, vol. 25, pp. 68–75, 1953.

[20] W. L. Nyborg, "Acoustic streaming near a boundary," *Journal of the Acoustical Society of America*, vol. 30, no. 4, pp. 329–339, 1958.

[21] W. L. Nyborg, "Radiation pressure on a small rigid sphere," *Journal of the Acoustical Society of America*, vol. 42, no. 5, pp. 947–952, 1967.

[22] L. P. Gor'kov, "On the Forces Acting on a Small Particle in an Acoustical Field in an Ideal Fluid," *Soviet Physics Doklady*, vol. 6, pp. 773–775, 1962.

[23] K. Yosioka and Y. Kawasima, "Acoustic radiation pressure on a compressible sphere," *Acustica*, vol. 5, no. 3, pp. 167–173, 1955.

[24] F. Petersson, A. Nilsson, C. Holm, H. Jönsson, and T. Laurell, "Separation of lipids from blood utilizing ultrasonic standing waves in microfluidic channels," *The Analyst*, vol. 129, no. 10, pp. 938–943, 2004.

[25] F. Petersson, A. Nilsson, C. Holm, H. Jonsson, and T. Laurell, "Continuous separation of lipid particles from erythrocytes by means of laminar flow and acoustic standing wave forces," *Lab on a Chip*, vol. 5, no. 1, pp. 20–22, 2005.

[26] K. Yasuda, S.-i. Umemura, and K. Takeda, "Concentration and fractionation of small particles in liquid by ultrasound," *Japanese Journal of Applied Physics, Part 1: Regular Papers & Short Notes & Review Papers*, vol. 34, no. 5B, pp. 2715–2720, 1995.

[27] K. Yasuda, K. Takeda, and S.-i. Umemura, "Studies on particle separation by acoustic radiation force and electrostatic force," *Japanese Journal of Applied Physics, Part 1: Regular Papers & Short Notes & Review Papers*, vol. 35, no. 5B, pp. 3295–3299, 1996.

[28] J. Spengler and M. Jekel, "Ultrasound conditionering of suspensions - studies of streaming influence on particle aggregation on a lab- and pilot-plant scale," *Ultrasonics*, vol. 38, p. 624, 2000.

[29] M. Wiklund, P. Spégel, S. Nilsson, and H. Hertz, "Ultrasonic-trap-enhanced selectivity in capillary electrophoresis," *Ultrasonics*, vol. 41, no. 4, pp. 329–333, 2003.

[30] J. Spengler, W. Coakley, and K. Christensen, "Microstreaming effects on particle concentration in an ultrasonic standing wave," *AIChE Journal*, vol. 49, no. 11, pp. 2773–2782, 2003.

[31] L. A. Kuznetsova and W. T. Coakley, "Microparticle concentration in short path length ultrasonic resonators: Roles of radiation pressure and acoustic streaming," *Journal of the Acoustical Society of America*, vol. 116, no. 4, pp. 1956–1966, 2004.

[32] A. Nilsson, F. Petersson, H. Jönsson, and T. Laurell, "Acoustic control of suspended particles in micro fluidic chips," *Lab on a Chip*, vol. 4, no. 2, pp. 131–135, 2004.

[33] H. Li and T. Kenny, "High speed particles separation using ultrasound for microtas and lab-on-a-chip application," in *Proc. 26th Annual International Conference of the Engineering in Medicine and Biology Society EMBC 2004*, vol. 1, pp. 2631–2634, 2004.

[34] M. Bengtsson and T. Laurell, "Ultrasonic agitation in microchannels," *Analytical and Bioanalytical Chemistry*, vol. 378, no. 7, pp. 1716–1721, 2004.

[35] H. Jonsson, C. Holm, A. Nilsson, F. Petersson, P. Johnsson, and T. Laurell, "Particle separation using ultrasound can radically reduce embolic load to brain after cardiac surgery," *Ann. Thoracic Surgery*, vol. 78, p. 1572, 2004.

[36] T. Lilliehorn, U. Simu, M. Nilsson, M. Almqvist, T. Stepinski, T. Laurell, J. Nilsson, and S. Johansson, "Trapping of microparticles in the near field of an ultrasonic transducer," *Ultrasonics*, vol. 43, no. 5, pp. 293–303, 2005.

[37] S. M. Hagsäter, T. G. Jensen, H. Bruus, and J. P. Kutter, "Acoustic resonances in microfluidic chips: full-image micro-PIV experiments and numerical simulations," *Lab on a Chip*, vol. 7, no. 10, pp. 1336–1344, 2007.

[38] S. M. Hagsäter, A. Lenshof, P. Skafte-Pedersen, J. Kutter, T. Laurell, and H. Bruus, "Acoustic resonances in straight microchannels: Beyond the 1D-approximation," *Lab on a Chip*, vol. 8, pp. 1178–1184, 2008.

[39] O. Manneberg, S. M. Hagsäter, J. Svennebring, H. M. Hertz, J. P. Kutter, H. Bruus, and M. Wiklund, "Spatial confinement of ultrasonic force fields in microfluidic channels," *Ultrasonics*, vol. 49, pp. 112–119, 2009.

[40] J. Svennebring, O. Manneberg, P. Skafte-Pedersen, H. Bruus, and M. Wiklund, "Selective bioparticle retention and characterization in a chip-integrated confocal ultrasonic cavity," *Biotechnology and Bioengineering*, vol. 103, pp. 323–328, 2009.

[41] T. G. Jensen, "Acoustic radiation in microfluidic systems," Master's thesis, MIC — Department of Micro and Nanotechnology, DTU — Technical University of Denmark, April 2007. http://www.nanotech.dtu.dk/microfluidics.

[42] P. Skafte-Pedersen, "Acoustic forces on particles and liquids in microfluidic systems," Master's thesis, DTU Nanotech, January 2008. http://www.nanotech.dtu.dk/microfluidics.

[43] L. M. Andersen, A. Nysteen, and M. Settnes, "Forces acting on microparticles in acoustofluidic systems," bachelor thesis, DTU Nanotech, June 2009. http://www.nanotech.dtu.dk/microfluidics.

[44] J. Lighthill, *Waves in fluid*. Cambridge University Press, 2005.

[45] CRCnetBASE Product, Copyrigth© 2009 Taylor and Francis Group, LLC, "CRC Handbook of Chemistry and Physics, 89^{th} edition." Online version, accessed through DTV: Technical Knowledge Center of Denmark, http://www.hbcponline.com.globalproxy.cvt.dk/, 2009.

[46] L. E. Kinsler, A. R. Frey, A. B. Coppens, and J. V. Sanders, *Fundamentals of Acoustics*. John Wiley & Sons, Inc., fourth ed., 2000. ISBN 978-0471-84789-2.

[47] F. Jacobsen, T. Poulsen, J. H. Rindel, A. C. Gade, and M. Ohlrich, "Fundamentals of acoustics and noise control." Department of Electrical Engineering, Technical University of Denmark, December 2008. Note no 31200.

[48] L. D. Landau and E. M. Lifshitz, *Theory of Elasticity, 3rd Edition. Course of Theoretical Physics*, vol. 7. Oxford: Pergamon Press, 1986.

[49] O. Nielsen, *Properties of silicon - 1.5 Stiffness of Si.* 4, London and New York: INSPEC, The Institution of Electrical Engineers, 1980.

[50] Schott, "Borosilicat-flachglas." http://www.naugatuckglass.com/downloads/borofloat.pdf.

[51] Ioffe Physical Technical Institute, Silicon — Mechanical properties, elastic constants, lattice vibrations. http://www.ioffe.rssi.ru/SVA/NSM/Semicond/Si/mechanic.html.

[52] COMSOL AB, *COMSOL Multiphysics User's Guide*, September 2008. Version 3.5.

[53] FERROPERM PIEZOCERAMICS A/S, "Ferroperm piezo-electric calculator." www.ferroperm-piezo.com, Jan 2003. Ver. 1.2.

[54] FERROPERM PIEZOCERAMICS A/S, "High quality components and materials for the electronic industry." www.ferroperm-piezo.com, May 2003. Full Catalogue, pdf.

[55] D. Brown, "Tracker 2.60 — free video analysis and modeling tool for physics education." Online open source: http://www.cabrillo.edu/ dbrown/tracker/, April 2009.

[56] Z. Wang and D. Guo, *Special Functions*. World Scientific, 1988.